nature aging

Article

https://doi.org/10.1038/s43587-025-00918-x

Extracellular vesicles from antler blastema progenitor cells reverse bone loss and mitigate aging-related phenotypes in mice and macaques

Received: 20 August 2024

Accepted: 6 June 2025

A list of authors and their affiliations appears at the end of the paper

Antler blastema progenitor cells (ABPCs) are a distinct population of skeletal mesenchymal stem cells found in regenerating deer antlers, with strong stemness and renewal capacity in vitro. Stem cell-derived extracellular vesicles (EVs) are emerging as potential therapeutic candidates that can mediate donor cells' beneficial effects. Here, we tested the effects of ABPC-derived EVs (EVs^{ABPC}) on aging in mice and rhesus macaques (*Macaca mulatta*). We identified a variety of unique factors in EVs^{ABPC} and showed that in vitro, EVs^{ABPC} attenuated phenotypes of senescence in bone marrow stem cells. In aged mice and macaques, EVs^{ABPC} substantially increased femoral bone mineral density. Further, intravenous EVs^{ABPC} improved physical performance, enhanced cognitive function and reduced systemic inflammation in aged mice, while reversing epigenetic age by over 3 months. In macaques, EV^{ABPC} treatment was also neuroprotective, reduced inflammation, improved locomotor function and reduced epigenetic age by over 2 years. Our findings position ABPCs as an emerging and practical source of EVs with translational value for healthy aging interventions.

Age-related disorders represent approximately 23% of the global diseases burden[1]. Aging is usually viewed as an inevitable time-dependent process that impaired cellular homeostasis and repair mechanisms[2,3]. Aging relies on a myriad of distinct responses and several hallmarks have been established, among which, progressive alterations in intercellular communication and inter-tissue crosstalk have garnered increasing attention[4,5]. Recent studies on systemic factors that promote healthy aging have identified several geroprotective factors from young individuals, tissues and cells to mitigate systemic aging[6,7]. Notably, the restoration of aged tissues or organisms has been achieved through transfusing factors like albumin[6] and tissue inhibitors of metalloproteinase 2 (ref. 7). These discoveries are driving therapeutic innovation in healthy aging, with ongoing efforts to identify emerging geroprotective factors.

Stem cells are a valuable source of geroprotective factors owing to their self-renewal and multiple differentiation nature[3,8]. EVs are nanosized membranous vesicles that are crucial mediators for intercellular communication by delivering components between cells[9–11]. Stem cell-derived EVs harbor geroprotective factors that can remediate aging through noncell-autonomous mechanisms[12] and mirror donor cells' therapeutic effects in preclinical/clinical studies, while avoiding the biosafety concerns of stem cells therapy[9,13]. Mesenchymal stem cells (MSCs) have attracted the most interest as they typically derived from postnatal tissues and have fewer safety and ethical concerns[8]. Yet in vitro expansion induces senescence in MSCs, compromising their geroprotective effect[14]. Additionally, MSCs from mammalian postnatal tissues have limited regenerative ability, restricting the efficacy of MSC-derived EVs in promoting healthy aging[15]. Therefore, identifying innovative MSCs with robust pro-regenerative potential might refine the role of MSC-derived EVs for geroprotective interventions.

In a recent study, we discovered an innovative MSC type in regenerating deer antlers, termed ABPCs, which reside at the local

e-mail: yaoyg@mail.kiz.ac.cn; wenwang@nwpu.edu.cn; zjluo@fmmu.edu.cn; qiuqiang@nwpu.edu.cn; huangjh@fmmu.edu.cn

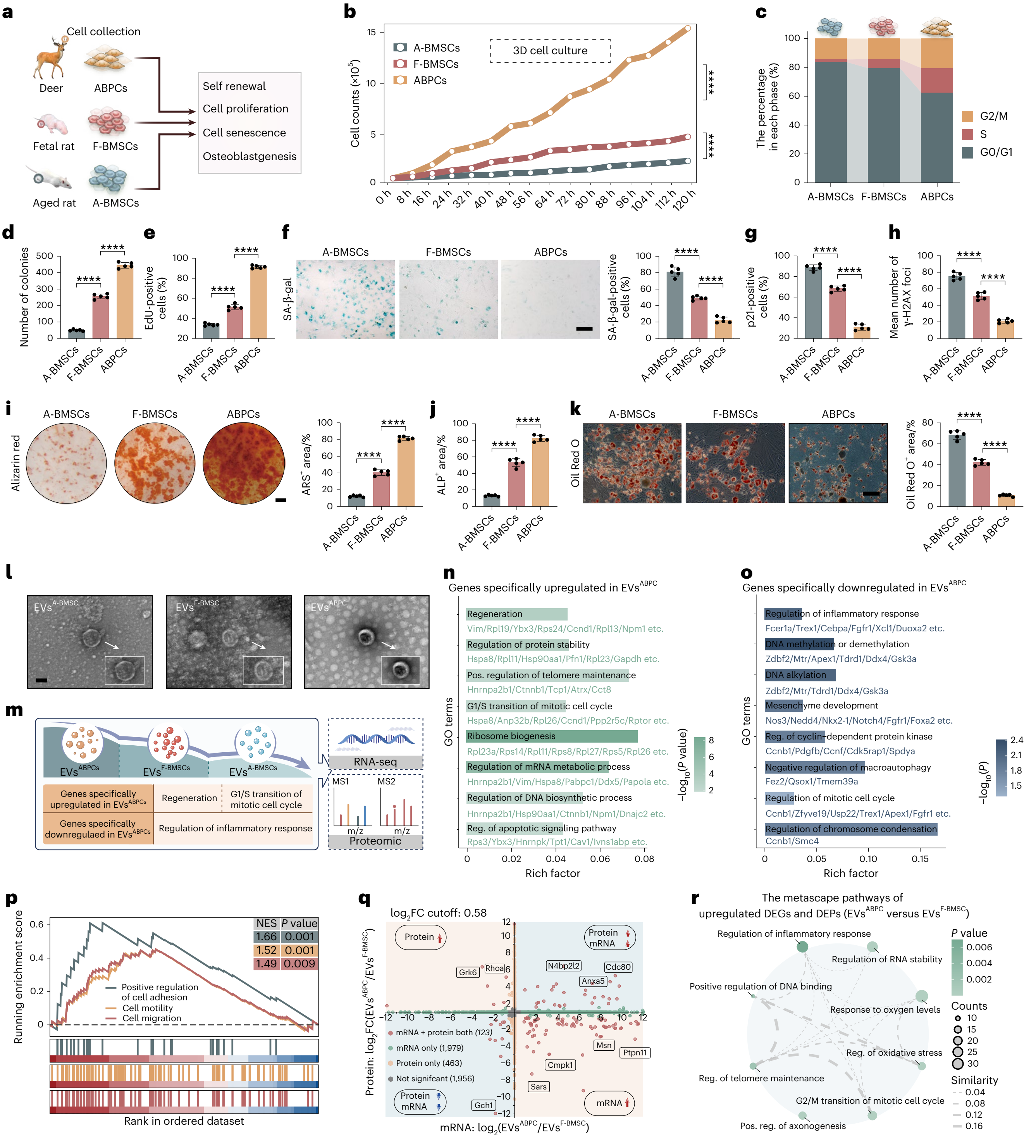

Fig. 1 | Biological properties of ABPCs and EVs^{ABPC}. **a**, The schematic diagram for the procedures of cell collection and functional characterization of ABPCs, F-BMSCs and A-BMSCs. **b**, Growth curves for cells over a 120-h period of culture. Cell counts were measured every 8 h. **c**, The proportion of cells in different cell-cycle phase at 72 h after culture using flow cytometry. **d**,**e**, CFU-F ability (**d**) and the ratios of EdU-positive cells (**e**) after culture of different cells ($n = 5$). **f**, Representative images of SA-β-gal staining in the three groups (left) and quantitative analysis (right) ($n = 5$). Scale bar, 200 µm. **g**, Quantification of p21 positive cells in the three groups ($n = 5$). **h**, Number of γ-H2AX foci in 4,6-diamidino-2-phenylindole (DAPI)-stained nuclei of cells ($n = 5$). **i**, Representative images of Alizarin Red staining (ARS) (left) and its quantitative analysis (right) ($n = 5$). Scale bar, 3 mm. **j**, Quantitative analysis of ALP-positive staining area ($n = 5$). **k**, Representative images of Oil Red O staining (left) and its quantitative analysis (right) ($n = 5$). Scale bar, 100 µm. **l**, Morphology of EVs detected by transmission electron microscopy. Scale bar, 100 nm. **m**, Schematic diagram shows the transcriptomic and proteomic analysis of EVs$^{A\text{-}BMSC}$, EVs$^{F\text{-}BMSC}$, and EVs^{ABPC}. **n**,**o**, GO term enrichment analysis of specifically upregulated (**n**) and downregulated (**o**) DEGs in EVs^{ABPC} compared to both EV$^{A\text{-}BMSC}$ and EV$^{F\text{-}BMSC}$ groups. **p**, GSEA for the enrichment of gene sets in EVs^{ABPC} compared to EVs$^{F\text{-}BMSC}$. **q**, Scatter-plot for multi-omics analysis (transcriptome and proteome) between EVs^{ABPC} and EVs$^{F\text{-}BMSC}$. The x axis represents the $\log_2$(FC) at mRNA level and the y axis represents the $\log_2$(FC) at protein level. FC, fold change. **r**, Network diagram represented the Metascape pathways of upregulated DEGs and DEPs in EVs^{ABPC} compared to EVs$^{F\text{-}BMSC}$. Each node corresponds to a specific biological process (BP) and the size of the node is proportional to the enrichment score. Statistical significance was calculated by two-way ANOVA-Bonferroni (**b**) or one-way ANOVA with Bonferroni's multiple comparisons test (**c**–**k**). Data are presented as mean ± s.d. ****$P < 0.0001$.

antler periosteum[16]. Notably, ABPCs can initiate de novo antler generation, which is the only mammalian organ to fully regenerate annually in adulthood. ABPCs and their progeny can drive the growth of bony antlers at 2.75 cm per day, producing a mass of up to 15 kg and length of 120 cm within 3 months, which is the fastest organ regeneration rate observed in mammals[17]. Unlike conventional MSCs (bone marrow, adipose or umbilical cord origins) showing senescence after 10–15 culture cycles[3,8,13,18], ABPCs maintain robust proliferative and regenerative capacities even after 50 cycles[13]. To our knowledge, ABPCs are the only postnatal mammalian MSCs enabling complete organ regeneration, highlighting their potential as a unique source of EVs for geroprotective therapies.

Results

EVs$^{\mathrm{ABPC}}$ attenuate cellular senescence in vitro

ABPCs were purified and compared to bone marrow stem cells (BMSCs) from aged (A-BMSCs) and fetal (F-BMSCs) rats (Fig. 1a). ABPCs exhibited a higher proliferation rate, a greater proportion in the S phase and enhanced colony formation compared to BMSCs (Fig. 1b–e and Extended Data Fig. 1a–c). At 120 h, the cell count of ABPCs was 5.71-fold and 3.07-fold higher than A-BMSCs and F-BMSCs, respectively (Fig. 1b). Given that stem cells of mesenchymal origin typically undergo senescence during prolonged culture in vitro, we next evaluated senescence markers after ten consecutive passages of culture (P10). A-BMSCs displayed increased aging-related markers, including senescence-associated β-galactosidase (SA-β-gal), p21 and γ-H2AX and adipocyte differentiation tendency. In contrast, ABPCs showed the lowest senescence markers and strongest osteogenic differentiation ability (Fig. 1f–k, Extended Data Fig. 1d–f and Supplementary Fig. 1a–d). Notably, the SA-β-gal activity in ABPCs was 72.4% and 54.5% lower than that in A-BMSCs and F-BMSCs, respectively (Fig. 1f). To address potential interspecies differences in BMSCs between deer and rodent, we isolated BMSCs from young male deer (D-BMSCs) and compared them to F-BMSCs from rats. D-BMSCs and F-BMSCs exhibited similar proliferation rate, differentiation capacities and aging markers (SA-β-gal and γ-H2AX) at P10, but they differed from ABPCs (Extended Data Fig. 2a–f). Overall, ABPCs possess a superior proliferative capacity and are less prone to senescence compared to BMSCs.

A greater abundance of vesicle-like structures was observed in ABPCs than in BMSCs, likely linked to increased EV production (Extended Data Fig. 1g). EVs$^{\mathrm{ABPC}}$ displayed similar morphology, surface charge and size with those of EVs derived from BMSCs (EVs$^{\mathrm{BMSC}}$) (Fig. 1l and Extended Data Figs. 1h–j and 2g–i). Additionally, EVs$^{\mathrm{ABPC}}$ were positive for typical EV markers, including CD9, CD81 and TSG101 (Extended Data Figs. 1k and 2j). Moreover, the concentration of EVs$^{\mathrm{ABPC}}$ was 2.13-, 2.20- and 9.39-fold higher than those of EVs derived from F-BMSCs (EVs$^{\mathrm{F\text{-}BMSC}}$), D-BMSCs (EVs$^{\mathrm{D\text{-}BMSC}}$) and A-BMSCs (EVs$^{\mathrm{A\text{-}BMSC}}$), respectively (Extended Data Figs. 1l and 2k), highlighting ABPCs as an attractive source for EV-based therapeutics. Next, we performed bulk RNA transcriptomic and proteomic analysis to characterize the compositions of EVs (Fig. 1m–r and Extended Data Fig. 1m–p). Compared to EVs$^{\mathrm{BMSC}}$, EVs$^{\mathrm{ABPC}}$ had a unique transcript profile, with upregulated differentially expressed genes (DEGs) engaged in regeneration (*Vim*, *Rpl19* and *Ybx3*), proteostasis (*Hspa8*, *Rpl11* and *Hsp90aa1*), telomere maintenance (*Hnmpa2b1*, *Ctnnb1* and *Tcp1*) and cell-cycle regulation (*Hspa8*, *Anp32b* and *Rpl26*) (Fig. 1n and Extended Data Fig. 1n). In contrast, pathways associated with aging hallmarks, such as inflammation (*Fcer1a*, *Trex1* and *Cebpa*) and epigenetic alterations (*Zdbf2*, *Mtr*, *Apex1* and *Tdrd1*)[19,20], were downregulated in EVs$^{\mathrm{ABPC}}$ (Fig. 1o). Additionally, EVs$^{\mathrm{ABPC}}$ outperformed EVs$^{\mathrm{F\text{-}BMSC}}$ in promoting cell adhesion, motility and migration (Fig. 1p). Among the upregulated differentially expressed proteins (DEPs) in EVs$^{\mathrm{ABPC}}$, key molecules such as DONSON, NDUFS2 and PARK7, are involved in the cell-cycle, oxidative stress response and inflammatory response (Extended Data Fig. 1o). Furthermore, a comprehensive multi-omics analysis, integrating both transcriptomic and proteomic data, revealed 1,979 specific DEGs (*Prkar2a*, *Anp32b* and *Ftl1*) and 463 specific DEPs (ADCY3, EXT1 and SPAG4) in EVs$^{\mathrm{ABPC}}$ compared to EVs$^{\mathrm{F\text{-}BMSC}}$ (Fig. 1q). Additionally, we identified 123 shared DEGs and DEPs associated with regulation of inflammatory response (*Cyld*, *Hspd1* and *Ldlr*), RNA stability (*Angel2*, *Celf1* and *Cnot1*) and cell cycle (*Arpp19*, *Cdk14* and *Fbxl17*)[21], all of which could influence the aging process (Fig. 1q,r). Meanwhile, the downregulated DEGs or DEPs were primarily involved in the negative regulation of cell migration (*Gstp1*, *Lrp1* and *Pdgfb*), neuron death (*Agt*, *Gata3* and *Ncstn*) and acute inflammatory response (*Fcer1a*, *Ptger3* and *Vnn1*) (Extended Data Fig. 1p). Collectively, these findings highlight the therapeutic potential of EVs$^{\mathrm{ABPC}}$ in mitigating age-related disorders.

To compare the geroprotective effects of the EVs, A-BMSCs were treated daily with different EVs for three consecutive days (Fig. 2a). Notably, PKH26-labeled EVs were detected within the A-BMSCs, indicating internalization by the A-BMSCs (Fig. 2b and Extended Data Fig. 3a). Dosage-effect tests identified 8×10^8 particles per ml of EVs$^{\mathrm{ABPC}}$ as optimal for mitigating aging-related phenotypes and facilitating osteogenic differentiation in A-BMSCs (Extended Data Fig. 3b–d). EVs$^{\mathrm{ABPC}}$ were more effective in promoting cell proliferation than EVs$^{\mathrm{F\text{-}BMSC}}$ and EVs$^{\mathrm{A\text{-}BMSC}}$, increasing the number of 5-ethynyl-2′-deoxyuridine (EdU)-positive cells, the proportion of S phase cells, and colony formation (Fig. 2c–f and Extended Data Fig. 3e–g). Furthermore, EVs$^{\mathrm{ABPC}}$ significantly lengthened telomeres (Fig. 2g) and reduced senescent markers in A-BMSCs (Fig. 2h–k, Extended Data Fig. 3h, i and Supplementary Fig. 2a,b). Notably, treatment with EVs$^{\mathrm{ABPC}}$, EVs$^{\mathrm{F\text{-}BMSC}}$ and EVs$^{\mathrm{A\text{-}BMSC}}$ decreased the SA-β-gal activity in A-BMSCs by 57.9%, 23.6% and 10.0%, compared to the vehicle group (Fig. 2h,i). Similar effects on proliferation and aging markers were observed with EVs$^{\mathrm{BMSC}}$ from both rat and deer origins (Extended Data Fig. 2l–n). Overall, these results suggest that the phenotypes of senescent BMSCs can be attenuated to varying degrees using different EVs, with EVs$^{\mathrm{ABPC}}$ exhibiting the strongest effect.

Aging induces a shift in BMSCs from osteogenic to adipogenic differentiation, resulting in age-related bone loss[22]. EVs from both

Fig. 2 | EVs$^{\mathrm{ABPC}}$ attenuate phenotypes of senescence in BMSCs. **a**, The schematic diagram for the procedure of cell culture, EVs isolation, treatment and related experiments. **b**, Internalization of PBS (top) and PKH26-labeled EVs$^{\mathrm{ABPC}}$ (bottom, yellow) in A-BMSCs stained with DAPI (blue) and phalloidin (white). Scale bar, 10 μm. **c**, Growth curves of A-BMSCs with different treatments for 120 h. **d**, Proportion of A-BMSCs in different cell-cycle phase detected after treatment with EVs for 72 h by flow cytometry. **e**–**g**, EdU-positive ratios (**e**), CFU-F capacity (**f**) and telomere lengths (**g**) of A-BMSCs with different treatments for 72 h ($n = 5$). **h**, Representative SA-β-gal staining of A-BMSCs treated with different EVs. Scale bar, 200 μm. **i**–**k**, The SA-β-gal-positive cell ratios (**i**), γ-H2AX foci cell number (**j**) and p21-positive cell ratios (**k**) of A-BMSCs. ($n = 5$). **l**–**n**, The proportion of positive area for ARS (**l**), ALP (**m**) and Oil Red O (**n**) staining in A-BMSCs ($n = 5$). **o**, PCA of the transcriptomic characteristics in A-BMSCs treated with PBS, EVs$^{\mathrm{A\text{-}BMSC}}$, EVs$^{\mathrm{F\text{-}BMSC}}$ and EVs$^{\mathrm{ABPC}}$, as well as PBS-treated F-BMSCs. The EV$^{\mathrm{ABPC}}$-treated A-BMSCs exhibited a similar transcript profile to PBS-treated F-BMSCs, as indicated by the dashed circle. **p**,**q**, Mufzz-based clustering of DEGs in A-BMSCs treated with different EVs. Clustering trend plots showing the expression of genes across different modules (**p**). Heatmap of clustered genes (modules) with associated BP (**q**). **r**, GSEA of SenMayo in A-BMSCs treated with different EVs. **s**, Transcriptomic analysis showed that *Prkar2a* is the top cargo specifically in EVs$^{\mathrm{ABPC}}$ and abundant in EV$^{\mathrm{ABPC}}$-treated cells (top). The relative expression levels of *Prkar2a* in EVs$^{\mathrm{ABPC}}$ and EV$^{\mathrm{ABPC}}$-treated cells by real-time PCR (bottom). **t**,**u**, SA-β-gal staining in A-BMSCs with EVs$^{\mathrm{ABPC}}$, EVs from *Prkar2a*-knockdown ABPCs (EVs$^{\mathrm{ABPC/sh}\mathit{Prkar2a}}$) (**t**), with EVs$^{\mathrm{A\text{-}BMSC}}$, EVs from *Prkar2a*-overexpressing A-BMSCs (EVs$^{\mathrm{A\text{-}BMSC/}\mathit{Prkar2a}}$) (**u**) ($n = 5$). Scale bar, 200 μm. Statistical significance was calculated by two-way ANOVA-Bonferroni (**c**), one-way ANOVA with Bonferroni's multiple comparisons test (**d**–**g** and **i**–**n**) or two-tailed Student's *t*-test (**t**,**u**). Data are presented as mean ± s.d. $^{*}P < 0.05$, $^{**}P < 0.01$, $^{***}P < 0.001$ and $^{****}P < 0.0001$.

https://doi.org/10.1038/s43587-025-00918-x

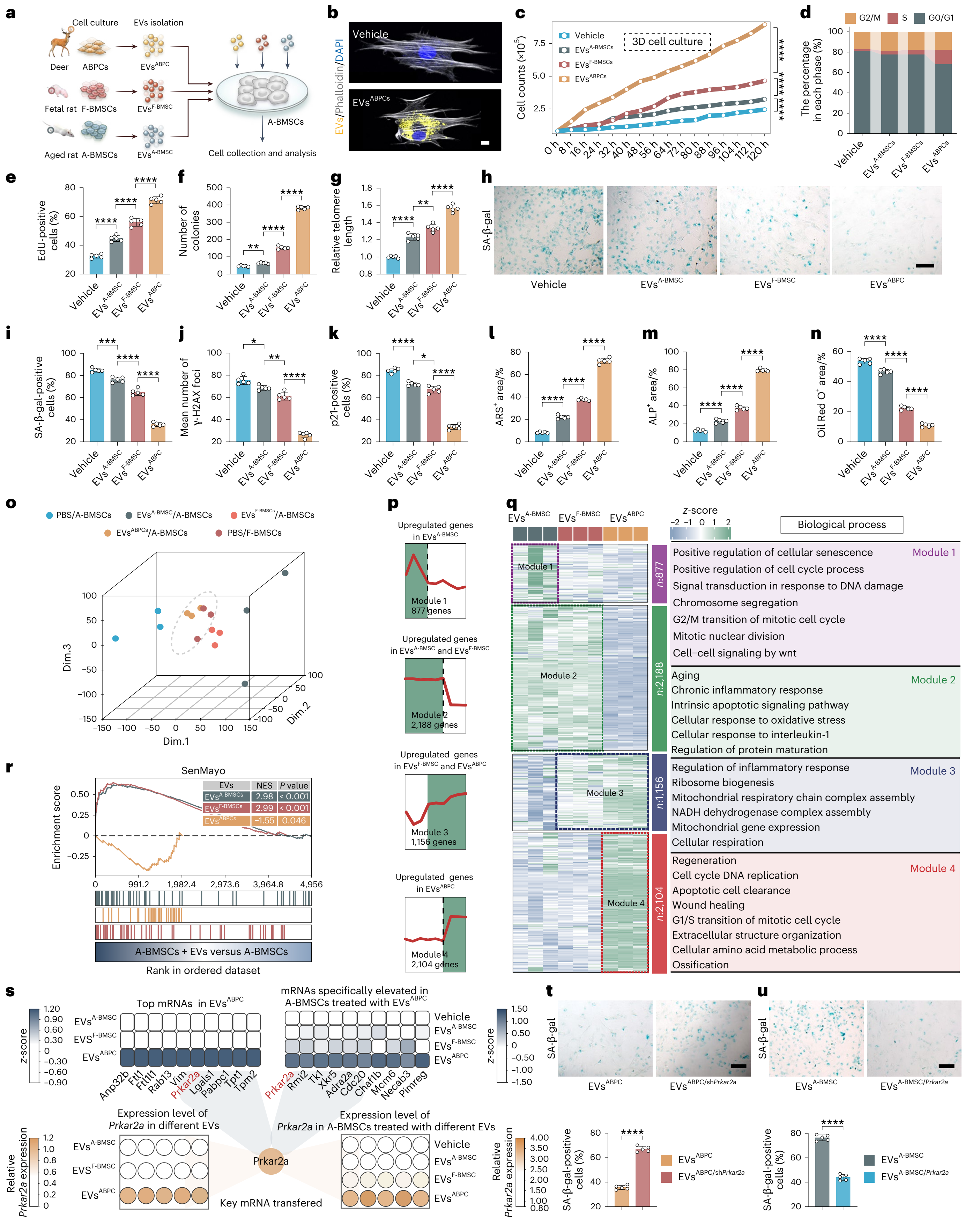

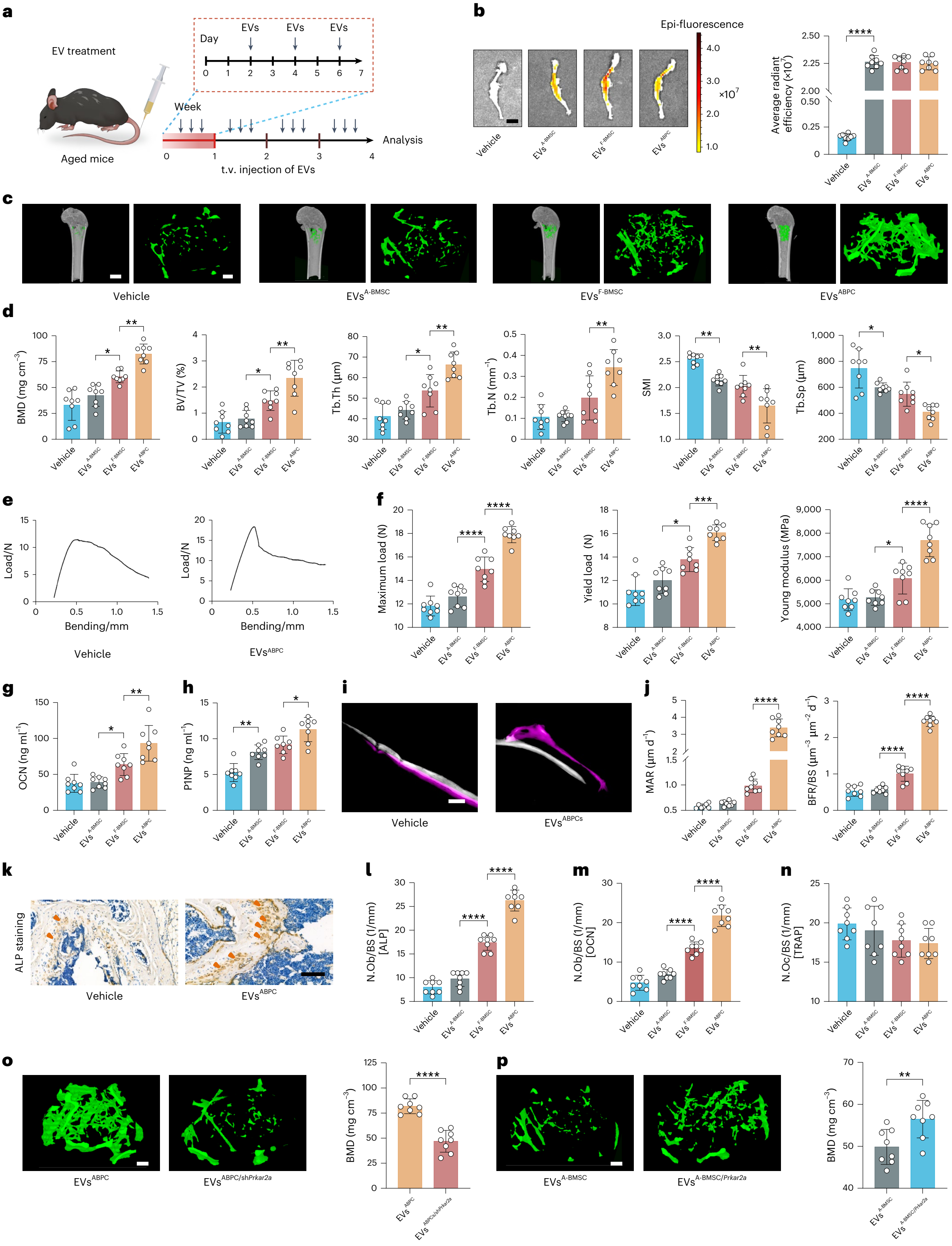
a
EV treatment
Aged mice
Day
EVs
EVs
EVs
0 1 2 3 4 5 6 7
Week
0 1 2 3 4
Analysis
t.v. injection of EVs
b
Epi-fluorescence
4.0
3.0
2.0
1.0
×10^7
Vehicle
EVs^A-BMSC
EVs^F-BMSC
EVs^ABPC
Average radiant efficiency (×10^7)
****
c
Vehicle
EVs^A-BMSC
EVs^F-BMSC
EVs^ABPC
d
BMD (mg cm^-3)
BV/TV (%)
Tb.Th (μm)
Tb.N (mm^-1)
SMI
Tb.Sp (μm)
e
Load/N
Bending/mm
Vehicle
EVs^ABPC
f
Maximum load (N)
Yield load (N)
Young modulus (MPa)
g
OCN (ng ml^-1)
h
PINP (ng ml^-1)
i
Vehicle
EVs^ABPCs
j
MAR (μm d^-1)
BFR/BS (μm^-3 μm^-2 d^-1)
k
ALP staining
Vehicle
EVs^ABPC
l
N.Ob/BS (1/mm) [ALP]
m
N.Ob/BS (1/mm) [OCN]
n
N.Oc/BS (1/mm) [TRAP]
o
EVs^ABPC
EVs^ABPC/shPrkar2a
BMD (mg cm^-3)
p
EVs^A-BMSC
EVs^A-BMSC/Prkar2a
BMD (mg cm^-3)

Fig. 3 | EVs$^{\text{ABPC}}$ promote osteoblastic bone formation in aged mice. a, The schematic for EV treatment in aged mice. Aged mice were treated with PBS (vehicle) or different EVs (40 μg per time), three times weekly for a duration of 4 weeks. **b**, Ex vivo fluorescence images (left) and average radiant efficiency (right) of femurs at 48 h after injection of DiR-labeled EVs ($n = 8$). Scale bar, 750 μm. **c**, Representative micro-CT reconstruction images of femurs from mice in different groups. Scale bar, 1,500 μm (left) or 300 μm (right) **d**, Quantitative analysis of BMD, BV/TV, Tb.Th, Tb.N, SMI and Tb.Sp in femurs after EV treatment ($n = 8$). **e**, Representative images of the mechanical strength of femurs in mice treated with PBS or EVs$^{\text{ABPC}}$. **f**, Quantification of the maximum load, yield load and Young's modulus in the femurs after EVs treatment ($n = 8$). **g**,**h**, The serum concentration of OCN (**g**) and P1NP (**h**) post-EVs treatment ($n = 8$). **i**, Representative images of the newly formed trabecular bone in the femurs of mice using calcein AM (magenta) and Alizarin Red (white) staining. Scale bar, 50 μm. **j**, Quantitative analysis of MAR and BFR/BS in mice after EV treatment ($n = 8$). **k**, Representative images of ALP staining in the femurs of mice treated with PBS or EVs$^{\text{ABPC}}$, showing the increased number of ALP-positive cells in EVs$^{\text{ABPC}}$ group (red arrows). Scale bar, 100 μm. **l**–**n**, Quantification of ALP (**l**), OCN (**m**) for osteoblast surfaces and TRAP (**n**) for osteoclast surfaces in femurs from mice with EVs treatment ($n = 8$). N.Ob/BS, number of osteoblasts per bone surface; N.Oc/BS, number of osteoclasts per bone surface. **o**,**p**, Representative micro-CT analysis of femurs from aged mice treated with EVs$^{\text{ABPC}}$, EVs$^{\text{ABPC/sh}\textit{Prkar2a}}$ (**o**) or EVs$^{\text{A-BMSC}}$, EVs$^{\text{A-BMSC/}\textit{Prkar2a}}$ (**p**) ($n = 8$). Scale bar, 300 μm. Statistical significance was calculated by one-way ANOVA with Bonferroni's multiple comparisons test (**b**,**d**,**f**–**h**,**j**,**l**–**n**) or two-tailed Student's t-test (**o**,**p**). Data are presented as mean ± s.d. $^*P < 0.05$, $^{**}P < 0.01$, $^{***}P < 0.001$ and $^{****}P < 0.0001$.

BMSCs and ABPCs reversed this process in A-BMSCs, as evidenced by increased mineralization nodule formation, alkaline phosphatase (ALP) activity, and decreased Oil Red O area (Fig. 2l–n and Extended Data Fig. 3j–l). Additionally, EVs$^{\text{ABPC}}$ enhanced osteogenic genes expression (*Alp*, *Runx2* and *Bmp2*) and suppressed adipogenic genes (*Fab-4*, *Ppar-γ* and *Lpl*) in A-BMSCs (Supplementary Fig. 2c,d). Among the three EVs, EVs$^{\text{ABPC}}$ exhibited strongest effect in facilitating osteogenic differentiation, followed by EVs$^{\text{F-BMSC}}$ and EVs$^{\text{A-BMSC}}$ (Fig. 2l,m and Extended Data Fig. 3j,k). Additionally, EVs$^{\text{BMSC}}$ from both rat and deer origins showed minimal differences in osteogenic induction of A-BMSCs (Extended Data Fig. 2o–q). RNA-seq analysis revealed that EVs$^{\text{ABPC}}$ altered A-BMSCs to a younger transcriptomic state, similar to F-BMSCs (Fig. 2o). Notably, the DEGs in EV$^{\text{ABPC}}$-treated cells possessed a unique cluster of geroprotective gene sets (Module 4), which is associated with tissue regeneration, DNA sustainment and repair, and apoptotic cells elimination (Fig. 2p,q). Subsequently, we employed a specialized gene set (SenMayo) to evaluate the senescence-associated secretory phenotype (SASP) in EV-treated cells (Supplementary Table 6)[23]. EVs$^{\text{ABPC}}$ resulted in downregulation of SenMayo set in senescent BMSCs, further confirming the potential of EVs$^{\text{ABPC}}$ in mitigating SASP in A-BMSCs ($P < 0.05$; Fig. 2r). Additional gene set enrichment analysis (GSEA) revealed that EVs$^{\text{ABPC}}$ had positive effects on certain aging hallmarks, such as DNA repair and maintenance, epigenetic alterations and telomere attrition (Extended Data Fig. 4a,b), while inhibiting SASP, chronic inflammation and cell exhaustion in A-BMSCs (Extended Data Fig. 4c,d). Overall, EVs$^{\text{ABPC}}$ demonstrated a strong geroprotective effect and restored A-BMSCs' molecular signature to a youthful state.

To identify the key cargo within EVs$^{\text{ABPC}}$, we focused on messenger RNAs unique to EVs$^{\text{ABPC}}$ but absent in EVs$^{\text{BMSC}}$. A total of 2,736 mRNAs were exclusively expressed in EVs$^{\text{ABPC}}$, with the most abundant cargos highlighted (Fig. 2s). Given that the main function of EVs is to transfer cargos to recipient cells, we then examined the top mRNAs that were specifically upregulated in A-BMSCs treated with EVs$^{\text{ABPC}}$ (Fig. 2s). Notably, *Prkar2a*, involved in the cell-cycle regulation and developmental maturation, was the only mRNA found both uniquely in EVs$^{\text{ABPC}}$ and abundant in A-BMSCs treated with EVs$^{\text{ABPC}}$ (Fig. 2s). This observation was further corroborated by real–time PCR (Fig. 2s). To confirm whether the high level of *Prkar2a* in A-BMSCs was delivered by the EVs$^{\text{ABPC}}$, we knocked down *Prkar2a* in ABPCs using *Prkar2a*-targeted shRNA (Extended Data Fig. 4e). Notably, EVs$^{\text{ABPC/sh}\textit{Prkar2a}}$ induced compromised geroprotective effect on A-BMSCs (Fig. 2t and Extended Data Fig. 4g,h), confirming *Prkar2a* as a critical cargo responsible for the geroprotective effect of EVs$^{\text{ABPC}}$. Furthermore, elevating *Prkar2a* level in EVs$^{\text{A-BMSC}}$ enhanced their ability to attenuate phenotypes of senescence in BMSCs (Fig. 2u and Extended Data Fig. 4f,i,j), suggesting that the information gleaned from EVs$^{\text{ABPC}}$ might enable the engineering of EVs from common sources to optimize their efficacy.

EVs$^{\text{ABPC}}$ alleviate bone loss in aged mice

Given that ABPCs and BMSCs are skeletal-derived stem cells[16], we investigated the effect of different EVs on age-related bone loss in aging mice. EVs were administered to mice every other day for 4 weeks via tail vein injection (Fig. 3a). Notably, the fluorescent dye (DiR)-labeled EVs were successfully detected in bones (Fig. 3b and Extended Data Fig. 5a). At 4 weeks, all EVs increased bone mineral density (BMD), with EVs$^{\text{ABPC}}$ showing the greatest increase (2.5-fold of vehicle) (Fig. 3c,d). Meanwhile, EVs$^{\text{ABPC}}$ outperformed EVs$^{\text{F-BMSC}}$ and EVs$^{\text{A-BMSC}}$ in improving trabecular bone microstructure, as evidenced by increased bone volume/total volume (BV/TV), trabecular thickness (Tb.Th) and trabecular number (Tb.N), along with decreased structure model index (SMI) and trabecular separation (Tb.Sp) (Fig. 3d); however, no significant differences were observed in cortical bones among all groups (Extended Data Fig. 5b,c). This is in line with the notion that bone loss in aged mammals predominantly occurs in trabecular bones rather than in cortical bones[24]. As fracture is the most common complication of bone loss[24], we assessed the mechanical strength of mouse femurs using a three-point bending test. Femurs from EV$^{\text{ABPC}}$-treated mice exhibited the highest maximum load, yield load and Young's modulus (Fig. 3e,f and Extended Data Fig. 5d).

Fig. 4 | EVs$^{\text{ABPC}}$ mitigate multiple age-associated phenotypes and transcriptomic signature in aged mice. a,**b**, Quantification of motor performance assessment by rotarod tests (**a**) and treadmill tests (**b**) ($n = 8$). **c**, SASP expression level of related inflammatory factors (IL-8, IL-6, IL-1β and TNF) in serum post-EV treatment ($n = 8$). **d**, Spearman correlation analysis was conducted to compare gene profiles in different EV-treated aged mice with 'Young' and 'Old' gene sets derived from young mice (8 weeks) and aged mice (18 months) ($n = 3$). Spearman's correlation coefficient (Corr) is displayed. The fit spline (green or blue lines) and 95% confidence intervals (green or blue areas) are shown. **e**, Aging-related biological pathways were significantly downregulated in the EV$^{\text{ABPC}}$ group. **f**, Correlation analysis of chronological age and DNAmAge for mouse blood. The Pearson's correlation coefficient (R) is displayed ($P < 0.0001$). The fit spline (black line) is shown. **g**, The rescue of DNAmAge in aged mice after EV treatment ($n = 3$). Box plots display median (center line), 25th and 75th percentiles (box limits) and 1.5× interquartile range (IQR) (whiskers). **h**,**i**, Representative images of SA-β-gal staining in organs of aged mice after EVs treatment (**h**) and their quantitative analysis (**i**) ($n = 8$). Scale bars, 50 μm (liver, skin and brain) and 200 μm (kidney and intestine). **j**, Cluster analysis of upregulated DEGs specifically enriched in multi-organs with EV$^{\text{ABPC}}$ treatment ($n = 3$). **k**,**l**, Spatial working memory was assessed using the Y maze as the discrimination index for the novel arm (**k**) and their quantitative analysis (**l**) ($n = 8$). **m**,**n**, Object recognition memory was assessed by NOR as the percentage of time exploring the novel object (**m**) and their quantitative analysis (**n**) ($n = 8$). **o**,**p**, Anxiety-like behavior was assessed by EPM as the percentage of open arm (**o**) and their quantitative analysis (**p**) ($n = 8$). Statistical significance was calculated by one-way ANOVA with Bonferroni's multiple comparisons test (**a**–**c**,**g**,**i**,**l**,**n**,**p**). Data are presented as mean ± s.d. $^*P < 0.05$, $^{**}P < 0.01$, $^{***}P < 0.001$ and $^{****}P < 0.0001$.

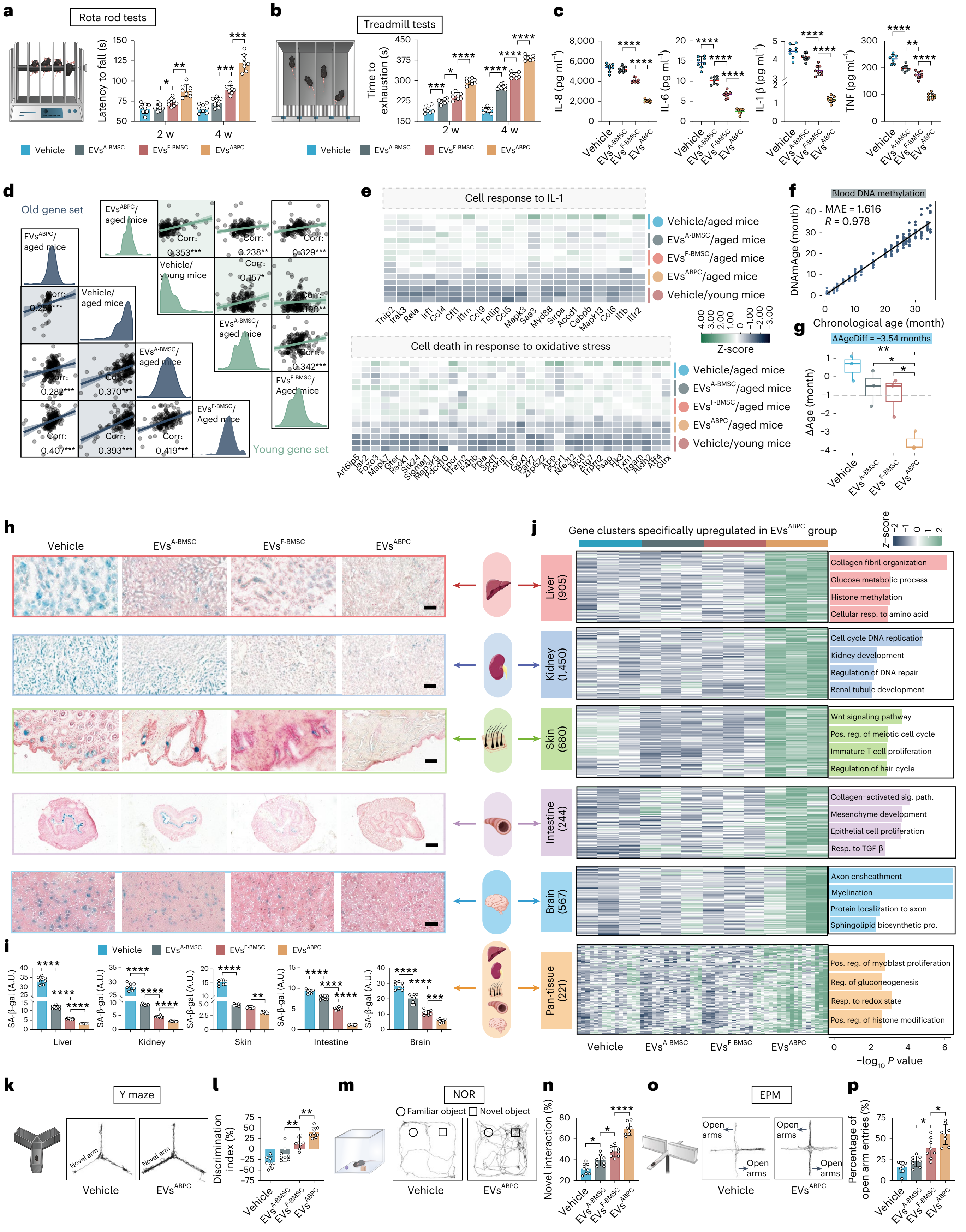
a
Rota rod tests
Latency to fall (s)
2 w
4 w
b
Treadmill tests
Time to exhaustion (s)
Vehicle
EVs^A-BMSC
EVs^F-BMSC
EVs^ABPC
c
IL-8 (pg ml⁻¹)
IL-6 (pg ml⁻¹)
IL-1 β (pg ml⁻¹)
TNF (pg ml⁻¹)
d
Old gene set
Young gene set
EVs^ABPC/ aged mice
Vehicle/ aged mice
Vehicle/ young mice
EVs^A-BMSC/ aged mice
EVs^F-BMSC/ Aged mice
Corr: 0.353***
Corr: 0.238**
Corr: 0.329***
Corr: 0.157*
Corr: 0.190**
Corr: 0.342***
Corr: 0.253***
Corr: 0.282***
Corr: 0.370***
Corr: 0.407***
Corr: 0.393***
Corr: 0.419***
e
Cell response to IL-1
Cell death in response to oxidative stress
Vehicle/aged mice
EVs^A-BMSC/aged mice
EVs^F-BMSC/aged mice
EVs^ABPC/aged mice
Vehicle/young mice
Z-score
f
Blood DNA methylation
MAE = 1.616
R = 0.978
DNAmAge (month)
Chronological age (month)
g
ΔAgeDiff = −3.54 months
ΔAge (month)
h
Vehicle
EVs^A-BMSC
EVs^F-BMSC
EVs^ABPC
i
SA-β-gal (A.U.)
Liver
Kidney
Skin
Intestine
Brain
j
Gene clusters specifically upregulated in EVs^ABPC group
Z-score
Liver (905)
Kidney (1,450)
Skin (680)
Intestine (244)
Brain (567)
Pan-tissue (221)
Collagen fibril organization
Glucose metabolic process
Histone methylation
Cellular resp. to amino acid
Cell cycle DNA replication
Kidney development
Regulation of DNA repair
Renal tubule development
Wnt signaling pathway
Pos. reg. of meiotic cell cycle
Immature T cell proliferation
Regulation of hair cycle
Collagen-activated sig. path.
Mesenchyme development
Epithelial cell proliferation
Resp. to TGF-β
Axon ensheathment
Myelination
Protein localization to axon
Sphingolipid biosynthetic pro.
Pos. reg. of myoblast proliferation
Reg. of gluconeogenesis
Resp. to redox state
Pos. reg. of histone modification
−log10 P value
k
Y maze
Novel arm
l
Discrimination index (%)
m
NOR
○ Familiar object
☐ Novel object
n
Novel interaction (%)
o
EPM
Open arms
p
Percentage of open arm entries (%)

Bone mass maintenance involves a balance between osteoblast-mediated bone formation and osteoclast-mediated resorption[25]. In our study, EVs^{ABPC} significantly increased serum levels of biomarkers of bone formation, osteocalcin (OCN) and procollagen type I N-terminal propeptide (P1NP), than mice in other groups ($P < 0.05$; Fig. 3g,h); however, the serum levels of C-telopeptide of crosslinked collagen type I (CTX-1), an indicator of bone resorption, were similar across all groups (Extended Data Fig. 5e). Additionally, EVs^{ABPC} promoted bone formation and mineralization in aged mice, with increased mineral apposition rate (MAR) and bone formation rate per bone surface area (BFR/BS) (Fig. 3i,j and Extended Data Fig. 5f). Concomitantly, EVs^{ABPC} generated a significantly more osteoblasts (ALP- or OCN-positive cells; $P < 0.0001$) than $EVs^{F\text{-}BMSC}$ and $EVs^{A\text{-}BMSC}$ (Fig. 3k–m and Extended Data Fig. 5g–i), whereas osteoclasts numbers, determined by tartrate resistant acid phosphatase (TRAP)-positive cells, were similar across all groups (Fig. 3n and Extended Data Fig. 5j). Collectively, these findings suggest that the beneficial effects of EVs^{ABPC} on bone loss are mainly due to enhanced osteogenesis rather than osteoclastogenesis. Considering that *Prkar2a* was identified as a key cargo within EVs^{ABPC} responsible for its geroprotective effect in vitro, we further investigated the effect of $EVs^{ABPC/sh\mathit{Prkar2a}}$ on bone loss in vivo. Knocking down *Prkar2a* expression in $EVs^{ABPC/sh\mathit{Prkar2a}}$ compromised the age-related bone loss alleviation, with a 42.7% drop in BMD compared to EVs^{ABPC} (Fig. 3o and Extended Data Fig. 5k,l), confirming the vital role of *Prkar2a*. Conversely, *Prkar2a* overexpression in $EVs^{A\text{-}BMSC}$ reversed bone loss in aged mice (Fig. 3p and Extended Data Fig. 5n,o). Similarly, no significance was observed in cortical bones quality among the groups (Extended Data Fig. 5m,p). These results highlight *Prkar2a* as a potential geroprotective factor for age-related skeletal diseases.

EVs^{ABPC} mitigate multiple aging-associated phenotypes in aged mice

Systemic administration of EVs^{ABPC} exerts broad effects, ameliorating multiple aging-associated phenotypes in aged mice. To assess EVs^{ABPC} on overall physical performance, we evaluated motor coordination and fatigue resistance using the graded-intensity rotarod tests and treadmill tests, respectively[5]. EV treatment improved the motor coordination (Fig. 4a) and the fatigue resistance (Fig. 4b) of mice at 14 days post-treatment, with the most notable improvements observed in the EV^{ABPC} group. These enhancements persisted for 4 weeks, peaking at day 28, when EV^{ABPC}-treated mice exhibited the most pronounced improvements in both tests (Fig. 4a,b).

Then, we assessed the effects of the EVs on serum inflammatory markers associated with SASP, vital indicators of aging status[4]. All three EV types reduced the serum levels of interleukin (IL)-8, IL-6, IL-1β and tumor necrosis factor (TNF) in aged mice ($P < 0.0001$; Fig. 4c), with EVs^{ABPC} demonstrated the most prominent anti-inflammatory effect, followed by $EVs^{F\text{-}BMSC}$ and then $EVs^{A\text{-}BMSC}$ (Fig. 4c). This reduction suggests that EVs^{ABPC} may contribute to systemic aging amelioration. Next, we performed transcriptomic analysis of blood samples (Fig. 4d,e). Two distinct gene expression profiles were identified, termed 'Young' and 'Old', based on the top 200 DEGs between young (8-week-old) and aged (18-month-old) mice. The gene expression profile of the EV^{ABPC}-treated group correlated most strongly with the 'Young' set and least with the 'Old' set (Fig. 4d). EVs^{ABPC} also reduced gene expression associated with SASP-specific pathways (cell response to IL-1) and oxidative stress (Fig. 4e). Furthermore, we quantified the biological age through establishing a methylation clock based on blood DNA methylation profiles[26]. In aged mice, EVs^{ABPC} reset DNA methylation age (DNAmAge) by an average of 3.54 months, surpassing the improvements by $EVs^{F\text{-}BMSC}$ (0.96 months) and $EVs^{A\text{-}BMSC}$ (0.59 months) (Fig. 4f,g). These findings emphasize the potential of EVs^{ABPC} in reversing age-associated molecular signatures and slowing down epigenetic aging.

To systematically evaluate the geroprotective effect of EVs^{ABPC} across different tissues in aged mice, we focused on major organs, including liver, kidneys, skin, intestines and brain (Fig. 4h–j and Extended Data Fig. 6a–r). Different EVs led to a significant reduction in SA-β-gal levels in all organs, with EVs^{ABPC} exhibiting the most pronounced effect (Fig. 4h,i). In addition, EVs^{ABPC} partially reversed histological fibrosis in liver and kidneys (Extended Data Fig. 6a,b,h,i) and mitigated cell apoptosis in kidneys (Extended Data Fig. 6c,j). In the skin, EVs^{ABPC} decreased epidermal and dermal thickness, collagen content and cellular senescence (γ-H2AX) (Extended Data Fig. 6d–f, k–o). In the brain (cerebral cortex), EVs^{ABPC} provided neuroprotection, evidenced by reduced γ-H2AX foci (Extended Data Fig. 6g,p). RNA-seq revealed that EVs^{ABPC} induced distinct gene expression signatures in each organ, including collagen fibril organization in liver, DNA replication and cell-cycle regulation in kidneys, Wnt signaling in skin, collagen-activated signaling and epithelial cell proliferation in intestines, and axon ensheathment and myelination in brain (Fig. 4j and Extended Data Fig. 6q,r). Overall, EVs^{ABPC} elicit notable geroprotective effects on major organs at both the histological and molecular levels in aged mice.

The geroprotective effect of EVs^{ABPC} on brain prompted further investigation into evaluating cognitive and anxiety-like behaviors, as improvements at cellular and molecular levels in brain may not always translate to functional or behavioral improvements. Cognitive performance was assessed using two-trial Y maze and novel object recognition (NOR) task (Fig. 4k–n and Extended Data Fig. 6s,t). EV^{ABPC}-treated aged mice exhibited a stronger preference for the novel arm in the Y maze (Fig. 4k,l and Extended Data Fig. 6s) and spent 69.4% of the time exploring the novel object in the NOR task, indicating enhanced memory and object recognition (Fig. 4m,n and Extended Data Fig. 6t). Moreover, anxiety-like behaviors were evaluated using elevated plus maze (EPM). EV^{ABPC}-treated mice spent 55.2% of the time in the open arms, significantly higher than that in the other groups (Fig. 4o,p and Extended Data Fig. 6u). Additionally, EVs^{ABPC} accumulated in the brain within 48 h following tail vein injection (Extended Data Fig. 6v). These findings, combined with histological data, suggest that EVs^{ABPC} can mitigate aging-related impairments in brain function, offering potential therapeutic applications for age-related neurodegenerative diseases.

Building on our findings in male mice, we next evaluated the effects of systemic administration of EVs^{ABPC} in aged female mice. Imaging, histological and behavioral analyses demonstrated that EV^{ABPC} treatment effectively alleviated age-related bone loss and senescence phenotypes across multiple organs in female mice (Extended Data Fig. 7), aligning with the male data. These results suggest that EVs^{ABPC} exert robust geroprotective effects in both male and female mice.

EVs^{ABPC} enhance bone mass in aged rhesus macaques

To assess the translatability of the functional effects observed in mice to humans, we investigated the effect of EVs^{ABPC} on aging phenotypes in rhesus macaques[27]. To minimize the number of rhesus macaques in this study, only $EVs^{F\text{-}BMSC}$ were utilized as controls for EVs^{ABPC}, based on their superior performance over $EVs^{A\text{-}BMSC}$ in our previous mouse study. Nine aged female rhesus macaques (aged 16–18 years, equivalent to 56–63 years in humans) were intravenously injected with saline ($n = 3$), $EVs^{F\text{-}MBSC}$ ($n = 3$) and EVs^{ABPC} ($n = 3$) for 20 weeks (15 mg, biweekly administration for a total of ten injections), respectively. To minimize animal welfare concerns, only examinations without the need for killing animals were conducted throughout this study.

Our primary focus was the therapeutic efficacy of EVs^{ABPC} in addressing age-related bone loss (Fig. 5a). Before EV therapy, no significant differences were observed in trabecular and cortical microstructures among the groups, as examined by computed tomography (CT) (Supplementary Fig. 3a–c). After 20 weeks, both EVs^{ABPC} and $EVs^{F\text{-}BMSC}$ improved BMD and trabecular bone quality (Tb.Th, Tb.N and BV/TV), with EVs^{ABPC} providing superior results (Fig. 5b–d). Particularly, EVs^{ABPC} outperformed $EVs^{F\text{-}BMSC}$ in restoring BMD, showing a 1.53- and 1.63-fold increase in the femur and lumbar vertebrae (L5) compared to

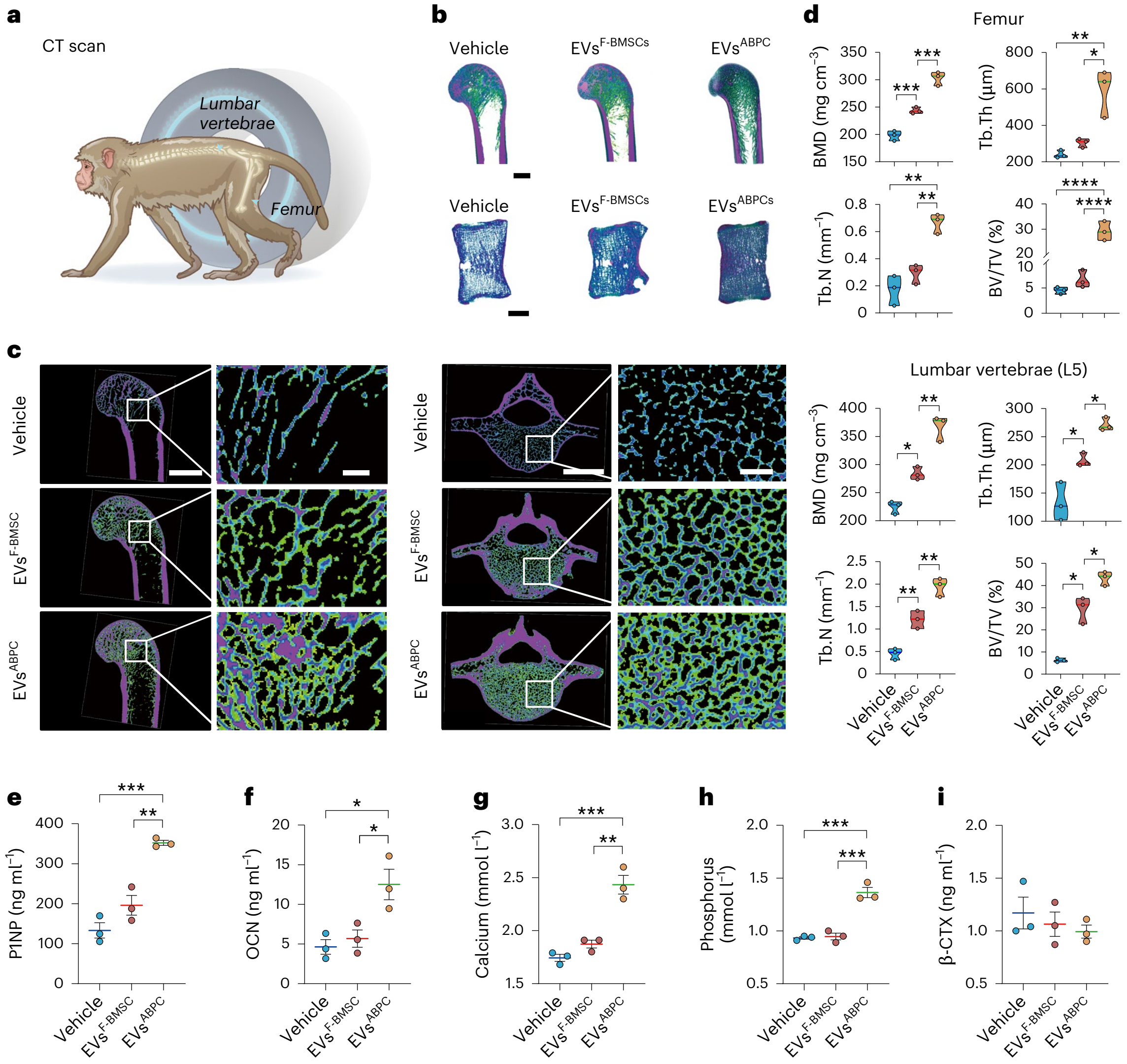

Fig. 5 | EVs$^{\text{ABPC}}$ enhance bone mass in aged rhesus macaques. **a**, The schematic diagram of CT scans for the femur and lumbar vertebrae (L5) of aged rhesus macaques across groups. Aged rhesus macaques were treated with PBS (vehicle) or different EVs (15 mg per time) every two weeks for ten administrations. **b**, Representative 3D CT reconstruction images of the femur (top) and lumbar vertebrae (L5) (bottom). Scale bar, 5,000 μm. **c**, Representative 2D CT reconstruction images of the femur (left) and lumbar vertebrae (L5) (right). Scale bar, 5,000 μm (first and third columns of c), 500 μm (second and fourth columns of c). **d**, Quantitative analysis of the trabecular bone in femur and lumbar vertebrae (L5) from aged rhesus macaques in the three groups ($n = 3$). **e**–**i**, Quantitative concentration analysis of serum biomarkers, including P1NP (**e**), OCN (**f**), calcium (**g**), phosphorus (**h**) and β-CTX (**i**) in aged rhesus macaques post-EV treatments ($n = 3$). Statistical significance was calculated by one-way ANOVA with Bonferroni's multiple comparisons test (**d**–**i**). Data are presented as mean ± s.d. $^{*}P < 0.05$, $^{**}P < 0.01$, $^{***}P < 0.001$ and $^{****}P < 0.0001$.

the vehicle group, respectively (Fig. 5d). Consistent with our observations in aged mice, cortical bone in aged rhesus macaques showed no significant changes following different EV treatment (Extended Data Fig. 8a,b). Furthermore, we examined the serum levels of bone metabolism markers[28]. Notably, bone formation indicators, such as P1NP, OCN, calcium and phosphorus levels were significantly elevated in serum by EVs$^{\text{ABPC}}$, but not in the EV$^{\text{F-BMSC}}$ group, compared to the saline group (Fig. 5e–h); however, the bone resorption indicator β-isomerized C-terminal telopeptides (β-CTX) was in the similar range across the three groups (Fig. 5i). These findings align with data in aged mice and indicate that EVs$^{\text{ABPC}}$ can effectively ameliorate age-related bone loss in aged rhesus macaques, mainly through enhancing bone formation.

EVs$^{\text{ABPC}}$ improve locomotor functions in aged rhesus macaques

We next examined the impact of EVs$^{\text{ABPC}}$ on locomotor functions, which are intimately connected to musculoskeletal functions[29], as observed in our mouse study. Using a three-dimensional (3D) fine-scale primate behavior analysis system[30], we evaluate the movement trajectories, overall activity level per unit time and postural kinematics of rhesus macaques (Fig. 6a–e). High-speed cameras recorded 35 min of free movement and resting, tracking 14 movements and 21 sets of representative body position (Fig. 6a). No baseline differences were detected among groups (Supplementary Fig. 4a,b). After treatment, EV$^{\text{ABPC}}$-treated rhesus macaques spent a longer period on movements with apparent displacement (AD) (walking, turning right, turning left, looking left and head raising) than the EV$^{\text{F-BMSC}}$- and saline-treated groups (Fig. 6b). No significances were observed between EV$^{\text{F-BMSC}}$- and saline-treated rhesus macaques (Fig. 6b). The EV$^{\text{ABPC}}$ group also exhibited greater activity positions diversity and faster movement speed (Fig. 6c,d), particularly in the head, back and root tail (Fig. 6e). Collectively, EVs$^{\text{ABPC}}$ remarkably enhanced the overall locomotor activity in aged rhesus macaques in an unfamiliar environment.

We next utilized a rotating Brinkman board task to evaluate monkey's manual dexterity that indicated upper limb motor abilities[31]

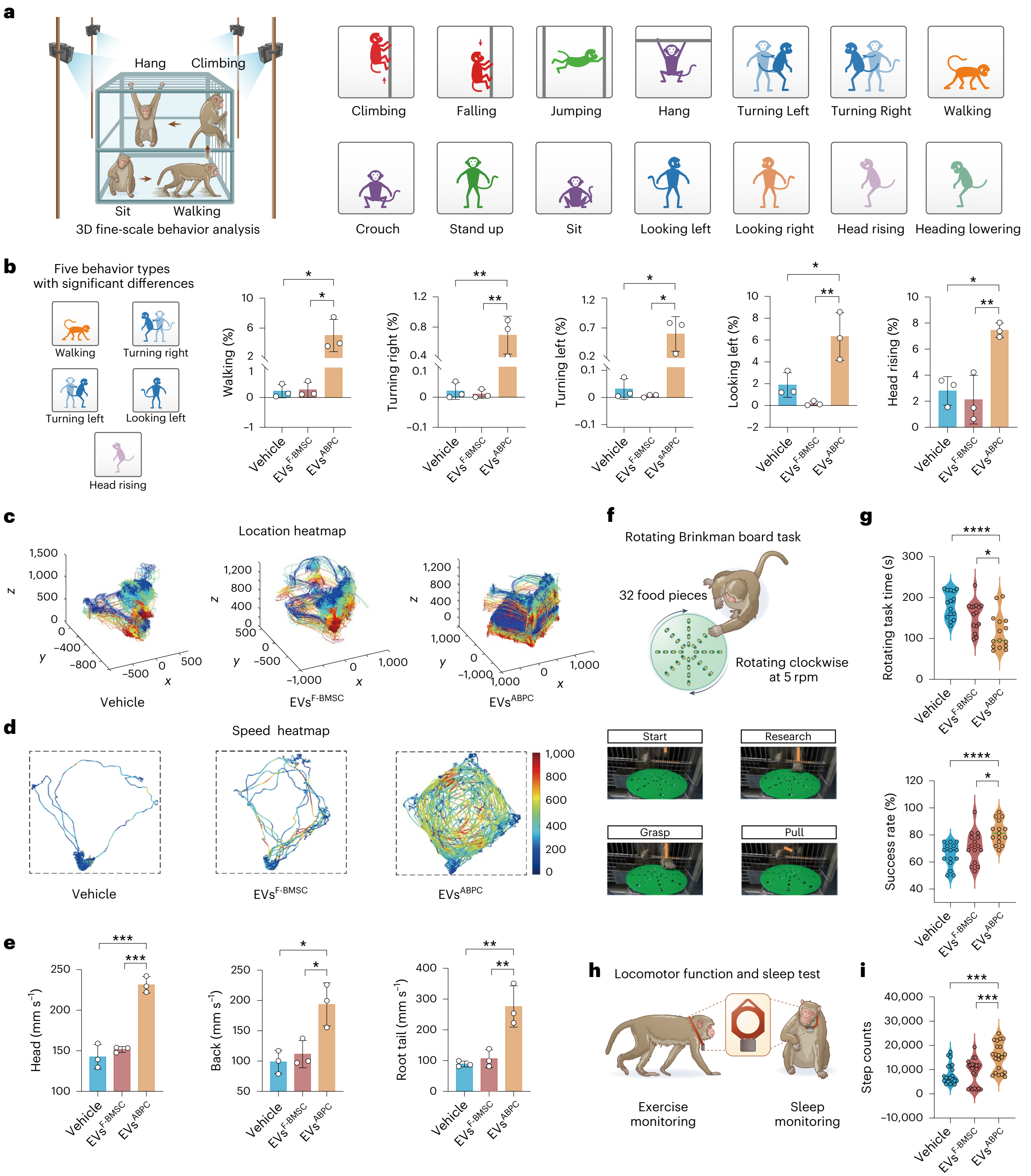

Fig. 6 | EVs$^{\mathrm{ABPC}}$ improve motor decline in aged rhesus macaques. a, Recording of rhesus macaques' movements, captured by four synchronized high-speed cameras during 35 min of free movement and resting, including a total of 14 movements. **b**, Five movement types (walking, turning right, turning left, looking left and head raising) exhibited significant differences in the EV$^{\mathrm{ABPC}}$ group compared to the other groups ($n = 3$). **c**, Location heatmaps visualize the motion trajectory of 21 body parts, with different colors distinguishing various body parts. **d**, Speed heatmap shows the velocity of the motion trajectory projected onto a two-dimensional plane parallel to the cage bottom. **e**, Motion speed for three body parts (head, back and tail root) reveals significant differences among different groups ($n = 3$). **f**, The schematic diagram shows the principle of rotating Brinkman board task (top). The task involves macaques retrieving 32 food pieces from a rotating board. The board rotates clockwise at a speed of 5 rpm. The task has four stages (1) start, begins the task; (2) research, searches for food pieces; (3) grasp, grasps a food piece; and (4) pull, pulls the food piece toward itself. **g**, Quantification of rotating task time (top) and success rate (bottom) among different macaque groups ($n = 3$). **h**, The schematic diagram shows two states (exercise and sleep) monitored by a noninvasive monitor neck collar for 7 consecutive days. **i**, Quantification of total step counts in aged rhesus macaques treated with EVs during a 7-day consecutive recording period ($n = 3$). Statistical significance was calculated by one-way ANOVA with Bonferroni's multiple comparisons test (**b**,**e**,**g**,**i**). Data are presented as mean ± s.d. $^{*}P < 0.05$, $^{**}P < 0.01$, $^{***}P < 0.001$ and $^{****}P < 0.0001$.

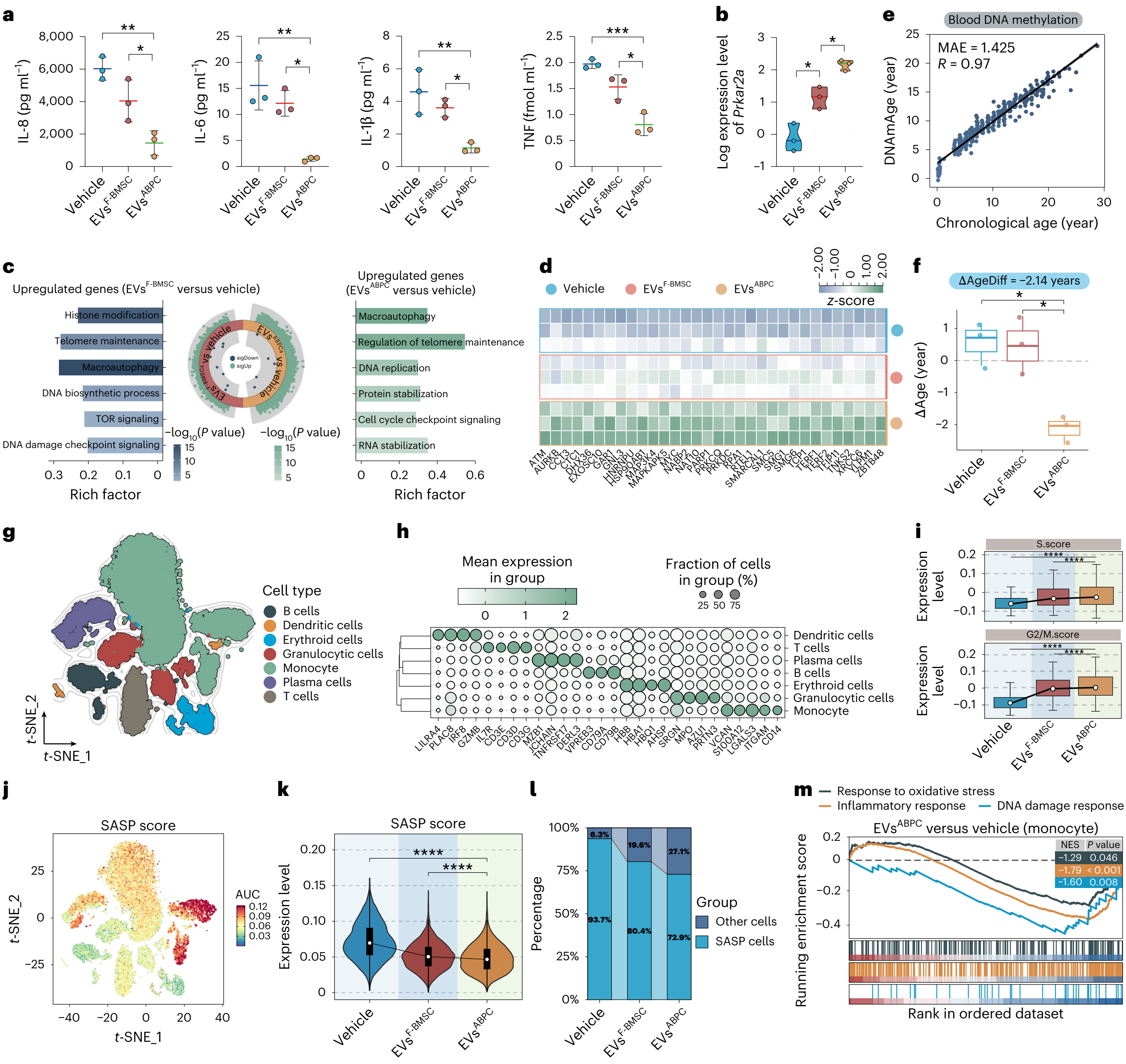

Fig. 7 | EVs^{ABPC} alleviate senescence in blood and bone marrow niche of aged rhesus macaques. a, Serum level of inflammatory factors of aged rhesus macaques treated with EVs ($n = 3$). **b**, Relative expression level of *Prkar2a* in blood samples from aged rhesus macaques by RNA-seq ($n = 3$). **c**, The biological pathways of upregulated genes in EVs$^{F\text{-}BMSC}$ (left) and EVs^{ABPC} (right), as compared to vehicle. **d**, Genes related to telomere maintenance pathway in blood samples. **e**, Correlation analysis of chronological age and DNAmAge for rhesus macaques' blood. The Pearson's correlation coefficient (R) is displayed ($P < 0.0001$). The fit spline (black line) is shown. **f**, The rescue of DNAmAge in aged rhesus macaques by EVs^{ABPC} ($n = 3$). Boxplots display median (center line), IQR (box limits) and 1.5 × IQR (whiskers). **g**–**m**, scRNA-seq analyzes the immune-lineage cells in bone marrow. A *t*-SNE plot shows the different cell types in bone marrow ($n = 23,511$ cells) (**g**). The expression levels of marker genes in seven immune-lineage cells (**h**). The S and G2/M phases scores across seven immune-lineage cells with different treatments. Boxplots display mean (white dot), IQR (box limits) and 1.5 × IQR (whiskers, from minimum to maximum). Lines connecting the medians across groups illustrate the overall trend of the data distribution (**i**). SASP gene expression strength across different cell types (**j**). The SASP gene expression scores across the whole immune-lineage cells. Violin plots depict the data distribution (kernel density), density (violin width), IQR (embedded box), mean (white dot) and mean ± s.d. (whiskers). Lines connecting the medians across groups illustrate the overall trend of the data distribution (**k**). The ratios of SASP-expressing cells across the whole immune-lineage cells (**l**). GSEA of three regulated pathways (**m**). Statistical significance was calculated by one-way ANOVA with Bonferroni's multiple comparisons test (**a**,**b**,**f**,**i**,**k**). Data are presented as mean ± s.d. $^{*}P < 0.05$, $^{**}P < 0.01$, $^{***}P < 0.001$ and $^{****}P < 0.0001$.

(Fig. 6f). At baseline, the rhesus macaques exhibited the similar rotating task time and success rates (Supplementary Fig. 4c). After treatment, both EVs^{ABPC} and EVs$^{F\text{-}BMSC}$ improved success rates of retrievals in clockwise tasks and decreased food exploration time (Fig. 6g), with EVs^{ABPC} achieving quicker responses and higher success rates (Fig. 6g), indicating better precision grip and postural adaptation of hand in aged rhesus macaques after EVs^{ABPC} treatment. Furthermore, ActiGraph noninvasive monitor neck collar was employed to monitor the monkeys' long-term locomotor activity within their familiar environment and living conditions, aiming to minimize potential bias associated with short-term recording (Fig. 6h). We performed consecutive monitoring of locomotor activity and sleep for 7 days in the monkey's home cage, with no significant differences observed at baseline (Supplementary Fig. 4d,e). In the EV^{ABPC} group, aged rhesus macaques exhibited a significant increase in total steps and average steps per minute compared to other groups, consistent with the results of the 3D fine-scale primate behavioral analysis ($P < 0.05$; Fig. 6i and Extended Data Fig. 8c). Nevertheless, no significance was found between the groups in sleep-related indices, including daily sleep duration, time from sleep onset to awakening and the number of awakenings (Extended Data Fig. 8d–f). Our data suggest that EV^{ABPC} treatment rescue aging-induced impairments in locomotor performance, with no adverse effects on sleep in aged rhesus macaques.

EVs^{ABPC} rescue blood and bone marrow in aged rhesus macaques

We next investigated the impact of EVs^{ABPC} on serum inflammatory markers associated with SASP in aged rhesus macaques. Blood samples were collected at 20 weeks post-treatment for analysis. Both EVs^{ABPC} and $EVs^{F\text{-}BMSC}$ significantly decreased serum pro-inflammatory cytokines (IL-8, IL-6, IL-1β and TNF) levels ($P < 0.05$; Fig. 7a), with EVs^{ABPC} exhibiting a more pronounced effect (Fig. 7a), indicating their superior anti-inflammatory capacity. No significant differences in complete blood counts and serum biochemistry (liver and kidney functions) across groups were observed, confirming the safety of EV treatment (Extended Data Fig. 9a). Consistent with the mouse experiment, RNA sequencing analysis showed an increase in *Prkar2a* level in blood post-EV^{ABPC} treatment (Fig. 7b). Gene Ontology (GO) analysis of DEGs identified several regeneration pathways enhanced by EVs^{ABPC}, including macroautophagy, regulation of telomere maintenance, DNA replication, protein stabilization, cell-cycle checkpoint signaling and RNA stabilization (Fig. 7c). Notably, EVs^{ABPC} were more effective than $EVs^{F\text{-}BMSC}$ in upregulating genes in blood involved with telomere maintenance in rhesus macaques (Fig. 7d). Consistent with the findings in mice, the signs of aging delay were further supported by methylation clock analyses of blood sample[32]. EVs^{ABPC} reset the global epigenetic age of aged rhesus macaques by an average of 2.14 years, representing a notable improvement compared to $EVs^{F\text{-}BMSC}$ (Fig. 7e,f). Collectively, these results suggest that EVs^{ABPC} have a stronger capability than $EVs^{F\text{-}BMSC}$ to reduce serum senescence-related molecular signatures and slow the biological age rate in aged rhesus macaques.

Aging rewires the bone marrow niche toward heightened inflammatory states with compromised osteogenesis of MSCs[33]. Therefore, we next proceeded to profile the responses of bone marrow cells to different EVs in aged rhesus macaques using single-cell RNA sequencing (scRNA-seq). Seven major cell subsets were identified within bone marrow immune-lineage cells (Fig. 7g,h and Extended Data Fig. 9b,c). Both EV types increased the proportion of cells in the S and G2/M phases, with EVs^{ABPC} exhibiting a more pronounced effect ($P < 0.0001$; Fig. 7i), suggesting the active revitalization of bone marrow cells in EV^{ABPC}-treated animals. Regarding cellular senescence, we found that EVs^{ABPC} significantly reduced the SASP level in senescent bone marrow immune cells ($P < 0.0001$; Fig. 7j–l), which is closely associated with aging-related bone metabolism[34]. Specifically, EVs^{ABPC} resulted in a greater reduction in senescent cells, in contrast to $EV^{F\text{-}BMSC}$ group (Fig. 7l). Additionally, strong SASP expression was enriched in the monocyte subpopulation (Extended Data Fig. 9d). Treatment with EVs^{ABPC} induced a shift in a transcriptional profile toward downregulated oxidative stress, chronic inflammation and DNA damage in the monocyte subpopulation (Fig. 7m). In contrast, $EV^{F\text{-}BMSC}$-treated animals exhibited fewer benefits (Extended Data Fig. 9e). Conclusively, EVs^{ABPC} ameliorate the senescence in bone marrow immune-lineage cells, providing a beneficial niche for bone formation to counteract age-related bone loss in rhesus macaques.

EVs^{ABPC} improve brain structure in aged rhesus macaques

Based on our previous findings regarding the geroprotective effects of EVs^{ABPC} on the brain and their ability to ameliorate the overall aging status in aged rhesus macaques, we speculate that potential of EVs^{ABPC} to partially mitigate brain aging in aged rhesus macaques. Using a SPECT/CT-based imaging strategy (Fig. 8a), we observed a significant accumulation of radioactivity in the brain from 1–8 h following systemic administration of ^{131}I-EVs^{ABPC} (Fig. 8b), which showed a high radiochemical purity of 98.3% and maintained in vitro stability of 92.0% in saline over 48 h. Notably, compared to ^{131}I[NaI] alone, ^{131}I-EVs^{ABPC} presented enhanced radioactive brain uptake, as evidenced by significantly higher standard uptake value (SUV) and target to background ratio (TBR) than those of adjacent background muscle (Fig. 8c,d). These findings suggest the possibility that EVs may effectively cross the blood–brain barrier, thereby highlighting their therapeutic potential in mitigating brain aging. Nevertheless, the detected cerebral radioactivity accumulation could not rule out the possibility of adherence of EVs^{ABPC} to cerebral vasculature, necessitating further investigations.

Next, we conducted a noninvasive magnetic resonance imaging (MRI) to investigate the impact of EVs on the brain structure of aged rhesus macaques (Fig. 8a). Given the limited sample size in the current study, our primary objective was to identify preliminary neuroimaging phenotypes at the whole-brain level following EV^{ABPC} treatment, rather than delving into specific region-wise changes or functional exploration. After a 20-week treatment period, EV^{ABPC} administration resulted in a significant increase in total intracranial volume (TIV) ($P_{FWE} = 0.022$; Fig. 8e). Specifically, this increase in TIV observed in EV^{ABPC}-treated rhesus macaques was predominantly attributed to alterations in gray matter volume (GMV), as evidenced by an elevated GMV (Fig. 8f,h), whereas white matter volume (WMV) showed no difference among the three groups (Fig. 8g,i). Furthermore, we analyzed additional morphometric properties related to gray matter to delineate the structural changes. The cortex of macaques treated with EVs^{ABPC} exhibited a tendency toward increase thickness and surface area, albeit these differences did not attain statistical significance (Extended Data Fig. 10a). This may be attributed to the small sample size or the possibility that the analysis method of voxel-based morphometry (VBM) is more sensitive in detecting structural changes while these detected brain alterations have less evident effects on surfaced-based metric such as cortical thickness and surface area[35–37]. Next, we conducted a preliminary analysis to identify potential region-specific GMV changes following EVs treatment. To balance detection sensitivity for neuroanatomical changes with the statistical limitations of our small sample size, voxel-wise comparisons were performed using a liberal statistical threshold (uncorrected $P < 0.05$). This analytical framework identified multiple clusters exhibiting an increased trend following EVs^{ABPC} (Extended Data Fig. 10b,c). Given our small sample size and the lack of multiple comparison correction at the voxel level, the interpretation of these findings necessitates caution and rigorous consideration; however, we posit that these data may hold promise for future studies aiming to quantitatively assess the degree of neuroprotection in brain regions most susceptible to aging or most responsive to treatment, through the enrollment of a larger cohort of animals. Additionally, no significant differences were observed in white matter metrics, including fractional anisotropy (FA) and radial diffusivity (RD), across the entire white matter region cross the three groups (Extended Data Fig. 10d). In summary, this brain imaging study provides preliminary evidence of the neuroprotective effects of EVs^{ABPC}, particularly within cerebral cortex of aged rhesus macaques.

Discussion

Our study identified ABPCs as a viable source of EVs enriched with geroprotective factors, with therapeutic benefits across multiple organs in aged mice and nonhuman primates (NHPs). EVs^{ABPC} attenuate

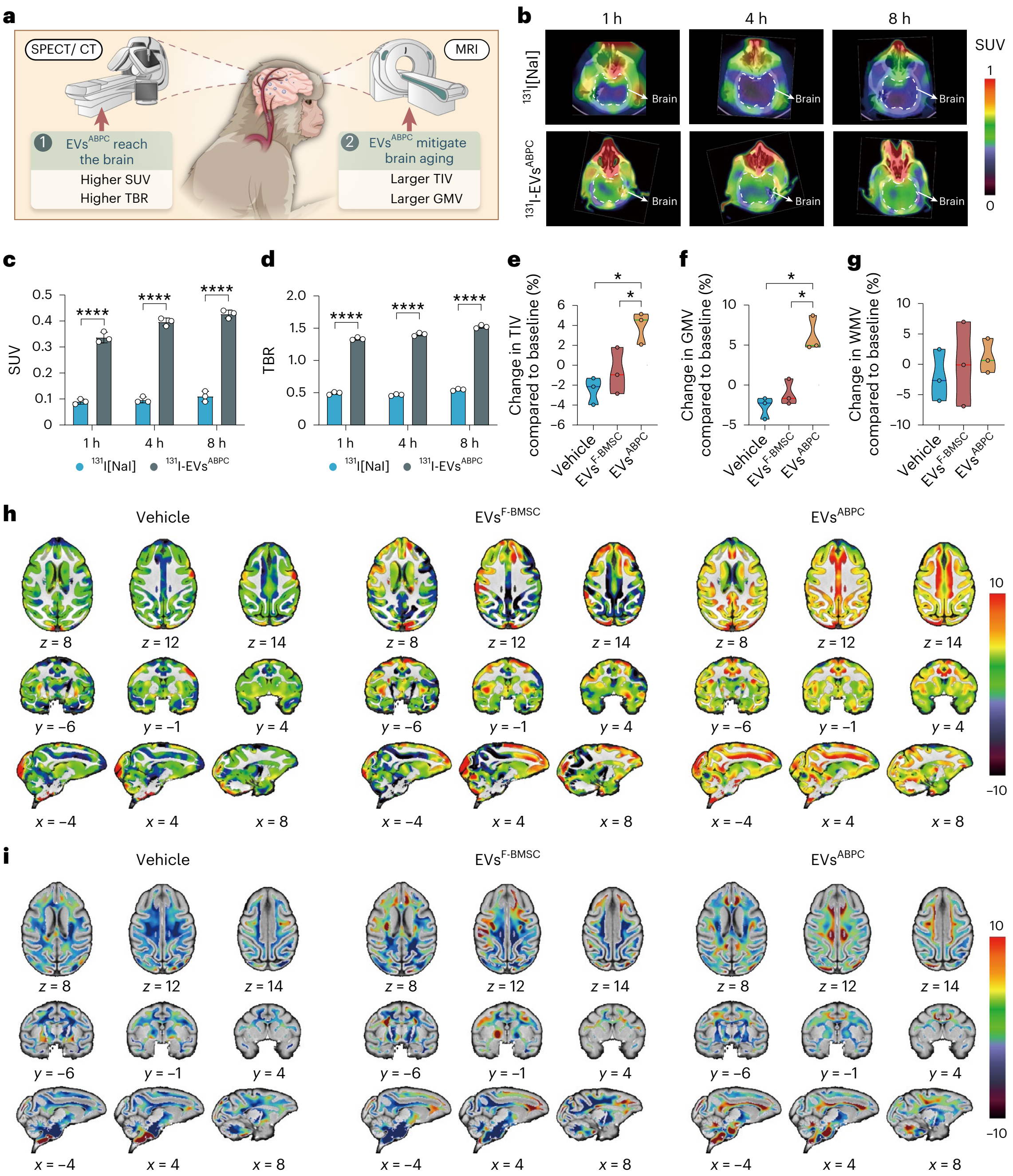

Fig. 8 | $\mathrm{EVs}^{\mathrm{ABPC}}$ alleviate brain aging in aged rhesus macaques. a, The schematic diagram shows using SPECT/CT to assess the situation of $\mathrm{EVs}^{\mathrm{ABPC}}$ reaching the brain of aged rhesus macaques and utilizing MRI to investigate the effect of EVs on the brain structure of aged rhesus macaques. **b**, Biodistribution and SPECT/CT imaging of aged rhesus macaques' brain, as indicated by dashed circles, at 1, 4 and 8 h after intravenous injection of [^{131}I]NaI and $^{131}\mathrm{I}\text{-}\mathrm{EVs}^{\mathrm{ABPC}}$. **c**,**d**, Quantitative analysis of radioactive brain uptake with SUV (**c**) and TBR with adjacent background muscle (**d**) following 1, 4 and 8 h after intravenous injection of purified [^{131}I]NaI and $^{131}\mathrm{I}\text{-}\mathrm{EVs}^{\mathrm{ABPC}}$ ($n = 3$). **e**–**g**, The percentage of changes in TIV (**e**), GMV (**f**) and WMV (**g**) compared to baseline over a 20-week treatment period among the groups ($n = 3$). **h**,**i**, The spatial brain maps for the percentage of changes in GMV (**h**) and WMV (**i**) compared to baseline, with the different colors indicating the extent of the changes in the average for each group, respectively. The *x*, *y* and *z* coordinates represent the 3D spatial positions within the brain, utilizing a Montreal Neurological Institute coordinate system. Statistical significance was calculated by two-way ANOVA with Bonferroni's multiple comparisons test (**c**,**d**), or nonparametric Kruskal–Wallis test with FWE correction for multiple comparison correction followed by post hoc pairwise between-group comparison conducted by one-tailed Mann–Whitney *U*-tests (**e**–**g**). Data are presented as mean ± s.d. $^{*}P_{\mathrm{FWE}} < 0.05$ and $^{****}P < 0.0001$.

phenotypes of senescence in stem cells, improve bone metabolism and reduce cellular senescence in bone marrow, resulting in an enhanced bone structure and strength in aged animals. Notably, $\mathrm{EVs}^{\mathrm{ABPC}}$ also induced a generalized rescue in the major organs of aged male mice, resetting their epigenetic age by an average of 3.54 months. Comparable benefits were observed in female mice. In rhesus macaques, $\mathrm{EVs}^{\mathrm{ABPC}}$ improve bone micro-architecture, ameliorate systemic inflammation, restore physical condition and enhance brain structure, highlighting their translational potential for clinical applications.

To date, the framework for assessing locomotor function in aging has been well established in mice, primarily employing graded-intensity treadmill and rotarod tests[5]; however, studies evaluating aging-related locomotor performance in aged primates remain scarce. Here, we employed a 3D fine-scale primate behavior test to assess spontaneous locomotor activity, utilizing a hierarchical 3D motion learning framework with multiple views[30]. This approach captures richer dynamic information compared to traditional approaches. Specifically, we placed rhesus macaques into testing cages slightly larger than their home cages within an empty room for a short-term (35 min) locomotor performance evaluation. Our analysis revealed that EVs^{ABPC} improved both movement speed and activity diversity in aged rhesus macaques. Although environmental alterations may introduce potential stress[38,39], the exploratory behavior induced by this slight stress could enhance locomotion, enabling us to effectively assess the monkeys' locomotor performance within a brief timeframe. To account for potential stress on experimental results, all testing environments and conditions were consistent, and a noninvasive neck collar monitor was used to track the long-term locomotor activity of the monkeys within their familiar environment and living conditions for 7 days. Our analysis reveals a similar locomotor improvement and good sleep quality by EVs^{ABPC}, indicating that the rescue aging-related impairments in locomotor performance were not attributes to stress. Collectively, our study provides a comprehensive understanding of locomotor changes in aged primates, and may offer valuable approaches for investigating aging-related declines in locomotor function in NHPs in future studies.

Direct delivery of geroprotective factors offers a promising strategy for delaying aging and alleviating age-related diseases. Consequently, it is crucial to identify the key cargo components within EVs^{ABPC} responsible for delaying aging and alleviating age-related diseases. Our study highlights *Prkar2a* as a pivotal geroprotective factor, largely recapitulates the revitalizing activity of EVs^{ABPC} in senescent cells and aging bones. Indeed, *Prkar2a* can translate into a component of the PKA holoenzyme, specifically the cyclic adenosine mono-phosphate (cAMP)-dependent protein kinase regulatory subunit IIα (RIIα), which decreases cell apoptosis and ameliorates inflammation[40,41]. Additionally, other factors within EVs^{ABPC} (*Cdc20*, *Adra2a*, *Pam* and *Timp1*) have been clarified to mitigating aging tissues and bone regeneration[42]. Although our focus was on mRNAs, EVs contain thousands of diverse cargos, including protein, DNAs, micro-RNAs and lipids[43]. Further studies should explore the relative contributions of these various components of EVs^{ABPC} to the aging process, and develop therapeutic strategies using EVs^{ABPC} and its related geroprotective factors for treating age-related diseases.

EVs^{ABPC} exhibited remarkable efficacy in ameliorating aging in multiple tissues, especially in the brain. Recent evidence has begun to shed preliminary insights into the role of EVs in brain aging. For instance, EVs isolated from the plasma of young mouse exhibit a clear cognitive-enhancing ability in aged mice by rescuing mitochondrial dysfunction[12]. In the current study, EVs^{ABPC} revitalized cognitive performance and reduced anxiety behaviors in aged mice. In aged rhesus macaques, long-term injection of EVs^{ABPC} exerted geroprotective effects on brain, notably increasing cerebral cortex volume. Indeed, previous studies have demonstrated that changes in mammalian brain volume and cortical-related metrics are closely associated with brain aging and function[44]. In a recent 40-month study, daily administration of metformin reversed brain aging by approximately 6 years in NHPs, with improvement primarily observed in cortical structure[45]. Considering that changes in brain structure are typically gradual, the increase in brain volume in the monkeys following 20-week treatment with EVs^{ABPC} is of translational importance. Generally, annual antler regeneration involves rapid nerve growth with a maximum rate of 2–3 cm per day, the fastest rate observed in mammals[25]. Additionally, EVs^{ABPC} contain various neuroprotective cargos (*Nrn1*, *Cobl* and *Fgfr2*), which may have contributed to the increase in brain volume. Nevertheless, future studies with a larger sample size of rhesus macaques and extended treatment duration will provide additional insights into the effect of EVs^{ABPC} on structural and functional changes in the brain, as well as identify the primary responsive brain regions.

EVs^{ABPC} offer several advantages for translational research, including a stable and abundant source of ABPCs from sika deer antlers. This makes ABPCs readily available using a standard culture and purification protocol. Additionally, ABPCs yield more EVs than MSCs at equivalent cell counts and passages. Furthermore, ABPCs can be expanded in vitro for at least 50 passages without exhibiting notable signs of senescence, whereas senescence in MSCs usually occurs after 10–15 passages. These characteristics make ABPCs a prominent source for EV-based geroprotective strategies. The utilization of EVs^{ABPC} presents a feasible strategy to overcome the limitations of stem cells, including the low retention and survival rate of stem cell delivery due to immune rejection. As EVs cannot self-replicate, concerns about tumor formation are minimized[46]. Additionally, EVs remain stable during long-term frozen storage or room temperature storage post-lyophilization, which is important for translational purposes[47].

Although EVs are safe for application in rodents and NHPs[5,27], long-term safety monitoring remains essential to exclude potential pro-tumorigenic effects. An additional safety concern regarding EVs from nonhuman species is possible adverse immunological reactions, although this was not observed in the present study. Moreover, although EVs^{ABPC} exerted geroprotective effects in female rhesus macaques, larger sample size encompassing both male and female individuals and extended longitudinal assessments are necessary for clinical translation. Furthermore, given the profound effect of EVs^{ABPC} on aging bones and organs, the use of engineering EVs^{ABPC} with tissue-specific binding peptides might allow geroprotective interventions in a specific tissue[48]. Finally, identifying emerging geroprotective factors that reside in EVs^{ABPC}, but not in other stem cells-derived EVs, may enable engineering of EVs from other common sources to optimize their efficacy.

Conclusively, EVs^{ABPC} provide a geroprotective strategy for attenuating phenotypes of senescence in cells and improving aging skeletons and organs in rodents and NHPs. Our study provides useful information for the development of promising treatments for age-related diseases.

Methods

Ethical approval

All animal procedures complied with Association for Assessment and Accreditation of Laboratory Animal Care International guidelines. Studies were approved by the Animal Ethics Committee of Fourth Military Medical University (IACUC-20230075), the Institutional Animal Care and Use Committee of Kunming Institute of Zoology (KIZ), Chinese Academy of Sciences (IACUC-PE-2023-05-002) and the Animal Ethics Committee of Changchun Sci-Tech University (CKARI202007).

Animals

Eighteen-month-old male and female healthy C57BL/6J mice were housed individually under a 12-h light–dark cycle with ad libitum access to chow and water. Animals were treated with different EVs or PBS (vehicle). The sample size ($n = 8$ mice per group) was determined using standard power analysis ($\alpha = 0.05$, power = 0.90) with the aid of PASS (v.23.0.2). EVs (40 µg, resuspended in 100 µl PBS) or 100 µl PBS were delivered via tail vein injection three times weekly for 28 days. After the final injection, mice were killed with ketamine (87.5 mg kg^{-1}) and xylazine (12.5 mg kg^{-1}), followed by transcardial perfusion with ice-cold PBS and major organs were collected.

All female rhesus macaques (*Macaca mulatta*) (16–18 years) were housed under identical 12-h light–dark conditions, with free access to standard chow, fruit and water. Nine female macaques were involved and randomly allocated 1:1:1 into three groups (EVs^{ABPC}, EVs$^{F\text{-}BMSC}$ and vehicle). Over 20 weeks, each macaque received ten intravenous administrations of 15 mg EVs in 5 ml saline or only 5 ml saline. Before imaging, examinations and blood collection, animals were pre-anesthetized with atropine (0.05 mg kg^{-1}, intramuscular injection) followed by ketamine (10 mg kg^{-1}, intramuscular injection). Anesthesia was maintained with continuous intravenous propofol at 15 mg kg^{-1} h^{-1}.

Cell isolation and culture

ABPCs were isolated as previously described using 2-year-old male sika deer[16]. On the fifth day post-antler shedding, animals were anesthetized, the pedicle region was sterilized, and an incision was made to expose the pedicle periosteum and regenerating antler tissue. The pedicle periosteum was collected in minimum essential medium (MEM) α for further processing. *Cx43*$^+$*Fgfr2*$^+$ cells were identified as ABPCs and sorted by flow cytometry. Single-cell suspensions in MEM α, 1% penicillin–streptomycin, 0.1% *Mycoplasma* removal agent and fetal bovine serum (FBS) were seeded in 10-cm dishes at 2×10^5 cells per cm^2 and cultured. When adherent cells reached 80–90% confluence, they were passaged at the same seeding density. ABPCs at P6–P10 were used for subsequent experiments.

BMSCs were isolated from 18-month-old (A-BMSCs) and fetal (F-BMSCs) male Sprague–Dawley rats, and 2-year-old male deer (D-BMSCs). For rats, bone marrow was flushed from diaphyses using MEM α. For deer, femoral bone marrow sample was aspirated aseptically using a trocar connected to a 10-ml syringe. All BMSCs were cultured in MEM α with 10% FBS Once cells reached 80–90% confluence, adherent cells were collected and seeded at a density of 2×10^5 cells per cm^2 for amplification. P6–P10 were used in all experiments.

3D cell culture

The 3D cultures were performed in 500-ml spinner flasks (CytoNiche) within a DASEA Regenbio mBioR-CC system housed in a cell culture incubator. DASEA Regencarrier Mimick microcarriers (2 g) were dispersed in 50 ml culture medium and 2.5×10^7 cells were introduced into the flask. Then final volume was adjusted to 500 ml.

Cultures underwent 48 inoculation cycles over 24 h, each comprising 5 min of stirring at 40 revolutions per minute (rpm) and 25 min resting. After 48 inoculation cycles, agitation was maintained at 40 rpm for 96 h. Culture supernatants were collected post-incubation for EV isolation.

Cell transfection

To modulate *Prkar2a* expression, ABPCs and A-BMSCs were transfected with lentiviruses (Genechem) encoding either *Prkar2a*-targeting shRNA (5′-GCATGTCTCTCCAACAATTA-3′) or *Prkar2a* cDNA (GenBank, NM_019264.2). Cells (1×10^5 to 1×10^6) were cultured in 12-well plates, and transfection was performed 24 h later. After 12 h, the medium was replaced with fresh complete medium. Subsequently, at 48 h post-transfection, transfection efficiency was confirmed *via* fluorescence microscopy and quantified by real–time PCR.

EdU assay

DNA synthesis was assessed using the Cell-Light EdU Apollo567 kit. Cells (5×10^3) were incubated with 50 μM EdU solution for 10 h. EdU-positive cells were quantified using ImageJ (v.2.14.0/1.54i).

Clonal-formation units

Cells (1×10^3) were stained with crystal violet. Colonies, identified as groups containing more than 50 cells, were counted under a light microscope.

Cell cycle analysis

Cells (1×10^6) were washed and centrifuged. Following this, the cell pellet was incubated darkly with 500 μl PI/RNase Staining Buffer for 30 min at 25 °C. Cell cycle analysis was performed by BD FACSCalibur (BD Biosciences) and ModFit LT (v.3.0).

Differentiation assays

Cells were induced in osteogenic or adipogenic medium with medium changes every 2 days for 14 and 21 days, respectively. Following differentiation, cells were stained with Alizarin Red S, ALP for osteogenic identification or Oil Red O for adipogenic differentiation. Images were photographed under a light microscope. The ratios of positive areas were determined using ImageJ.

Telomere lengths analysis

Total RNA was isolated using RIzol reagent according to the manufacturer's instructions. Then, RNA sample (1 μg) was reverse-transcribed into complementary DNA using the ReverTra Ace qPCR RT kit. Real–time PCR was conducted using SYBR Green PCR Master Mix on a StepOnePlus real-time PCR system. Primer details are provided in Supplementary Table 5. GAPDH and β-actin served as internal control genes. Telomere lengths were normalized to 36B4 (*RPLP0*) as the housekeeping gene.

Isolation and characterization of EVs

Cells (2.5×10^7) were seeded in 500-ml 3D spinner flasks and cultured in medium with EV-free FBS. The supernatants were sequentially centrifuged at 750*g* for 20 min followed by 2,000*g* for 30 min. The supernatant was then centrifuged at 16,000*g* for 70 min. Subsequently, the supernatant was centrifuged at 100,000*g* for 70 min. All centrifugation was conducted at 4 °C. The resulting EV pellet was resuspended in 1 ml PBS and stored at −80 °C. Protein concentration was measured using a BCA kit.

EV characterization was confirmed by EV protein markers (CD9, CD81 and TSG101) by western blot, morphology by transmission electron microscopy and particle size by nanoparticle tracking analysis (NTA).

In vitro tracking of EV uptake

EVs were labeled with PKH26 after diluting in Diluent C at 25 °C for 5 min. After incubating with PKH26-labeled EVs at 37 °C for 24 h, cells were stained with FITC-phalloidin for 30 min and then visualized with a confocal microscope. Fluorescence intensity was quantified using ImageJ.

Ex vivo tracking of EVs

EVs (4 μg μl^{-1}) were incubated with 15 μl DiR for 30 min at 37 °C, followed by centrifugation at 16,000*g* for 1 h at 4 °C. DiR-labeled EVs were injected via the tail vein in mice. At 48 h post-injection, mice were killed and organs were collected. Then fluorescence intensity was measured using the fluorescence imaging system.

Real–time PCR

Total RNA was extracted and purified from cells or EVs using the MiniBEST Universal RNA Extraction kit following the manufacturer's instructions. Then, 2 μg of RNA was utilized for cDNA preparation employing a Transgene reverse transcription kit. The reverse transcription reaction was conducted at 16 °C for 5 min, followed by 42 °C for 60 min and concluded with a final step of 85 °C for 5 min. Real–time PCR was performed using SYBR Green Master Mix and amplified on a 7500 real-time PCR system. The PCR reaction was performed during the initial denaturation at 95 °C for 10 min, amplification for 40 cycles, denaturation at 95 °C for 15 s, annealing at 60 °C for 30 s and extension at 72 °C for 30 s. Expression was normalized to *Gapdh* using the 2C−ΔΔt method. All reactions were executed in three technical replicates. Primers are listed in Supplementary Table 5.

Histological analysis

Organs were fixed in 4% PFA for 48 h. Femurs were then decalcified in 10% EDTA for 30 days. The remaining organs were directly embedded in paraffin. Sections (8 μm) were prepared for histological and immunofluorescence staining according to standard protocols. Images were captured with a microscope and analyzed with ImageJ.

SA-β-gal assay

The level of SA-β-gal was stained by a standard kit. Cells were incubated with SA-β-gal solution for 18 h. For tissue analysis, frozen sections were incubated with SA-β-gal solution for 18 h and counterstaining with nuclear fast red. Images were acquired by light microscope, SA-β-gal-positive cells were quantified using ImageJ from randomly selected fields.

Fluorochrome calcein mineral staining

Mice were intraperitoneally injected with calcein (10 mg kg^{-1}) and Alizarin Red (15 mg kg^{-1}) on days 3 and 17 before killing. Femurs were collected, fixed, dehydrated and embedded in methyl methacrylate. Sections were analyzed using fluorescence microscopy. BFR/BS and MAR were calculated by ImageJ.

Immunofluorescence assay

Cells or organs were permeabilized with 0.1% Triton X-100, blocked with 10% goat serum for 2 h and incubated with primary antibodies overnight at 4 °C, followed by secondary antibody for 1 h. Finally, nuclei were counterstained with 4,6-diamidino-2-phenylindole (DAPI). Images were captured using a fluorescence microscope and analyzed using ImageJ.

Mechanical properties

Femurs were horizontally positioned with a 9.9-mm span and tested using a Bose ELF3220 system at a displacement rate of 2 mm min^{-1} to generate load-displacement curves until failure. Maximum load (N), yield load (N) and Young's modulus (MPa) were calculated.

ELISA

Mouse serum levels of OCN, P1NP, CTX-I, IL-8, IL-6, IL-1β and TNF, were measured by standard ELISA kits according to protocols.

Blood routine examination in macaques

Whole blood (1 ml) from a macaque's femoral vein was analyzed using a XN series automated hematology analyzer.

Serum biochemical and inflammatory indicators in macaques

Blood was collected from a macaque's femoral vein. Liver and kidney function indicators were measured using an Indiko Plus clinical and specialty chemistry analyzer. Serum levels of P1NP, OCN and β-CTX were assessed via electrochemiluminescence immunoassay. IL-6, IL-8, IL-1β and TNF were determined by chemiluminescence immunoassay. Calcium and phosphorus content were analyzed according to instructions.

Behavioral tasks in mouse

Motor coordination was assessed using a rotarod, where mice underwent a 5-min training trial at 4 rpm followed by three accelerating trials (0 to 40 rpm in 300 s) with a 1-h rest between trials. Latency to fall was recorded, with a maximum time of 300 s. Graded-intensity treadmill test was performed, starting at 10 cm s^{-1} for 4 min, with a 4 cm s^{-1} increase every 2 min until exhaustion, defined as remaining on the shock grid for over 5 s.

The Y maze test was conducted with a 5-min training session where they explored the start and trained arms while the novel arm was blocked. After a 30-min rest, mice were allowed to explore all three arms for 5 min. The discrimination index was calculated as (novel arm − trained arm)/(novel arm + trained arm), the value representing the number of entries into each arm. The NOR test was performed over 3 days: habituation (10 min), training (5 min with two identical objects A and A) and testing (5 min, one of objects A was replaced with one novel object B). The recognition index was calculated as (time spent exploring object B)/(time spent on objects A and B). The EPM test was conducted on a cross-shaped platform with two open and two closed arms. Mice explored the maze for 5 min under red light (5 lux). Anxiety-like behavior was assessed by calculating open arm/(open arm + closed arm), the value representing the number of entries into each arm. The Y maze, NOR and EPM tests were conducted after EV treatment.

Locomotor activities in macaques

A multiview video system recorded macaque spontaneous behaviors in a transparent-walled cage (150 × 150 × 150 cm) positioned centrally in a quiet room. Four Intel RealSense D435 cameras, mounted 1.1 m from the cage on pillars, captured synchronized 30-Hz footage (848 × 480 resolution) at optimized angles for full arena coverage. Subjects were transferred using a transfer box. The tests were conducted at baseline and 20 weeks after EV treatment.

Data collection and analysis utilized BehaviorAtlas NHP Explorer/Analyzer software (Bayone BioTech, v.1.01)[7]. A model trained on 4,200 labeled frames (21 key body parts from eight macaques) extracted 46 kinematic parameters to construct 14 movement sequences. The 21 body parts included the nose, left eye, right eye, head, neck, left shoulder, right shoulder, left elbow, right elbow, left wrist, right wrist, left limb, right limb, left knee, right knee, left ankle, right ankle, back, root tail, mid tail and tip tail. The 14 movements are in Fig. 6a. Movements were categorized as AD or without AD (NAD) and analyzed separately. Movements with NAD included hanging, crouching, standing and sitting movements and those linked to AD comprised the remaining ten movement types. Results were standardized via z-scores. Each macaque underwent two 35-min recording sessions in the morning and afternoon, respectively.

Rotating Brinkman board task

Macaques' preferred-hand dexterity was tested over five daily sessions using a rotating Brinkman board (20-cm diameter, 5 rpm) at baseline and 20 weeks after EV treatment. Performance was scored by reward retrieval time (max 5 min) and success rate[27].

Home cage activity and sleep

The ActiGraph GT9X Link (3.5 × 3.5 × 1 cm, 14 g) was attached to macaques' collars to monitor diurnal activity (7:00–19:00) and nocturnal sleep (19:00–7:00) over 7 days. Using ActiLife 6 software (60-s epochs, v.6.13.4), locomotor activity (step counts and steps per min) and sleep parameters (total sleep time, wake after sleep onset and number of awakenings) were assessed at baseline and 20 weeks after treatment.

Micro-CT scanning

Following 4 weeks of treatment, femurs were collected, then subjected to micro-CT scanning using a Skyscan 1276 system (Bruker). The images were reconstructed by NRecon (v.1.7.3.1) and bone density data were analyzed by CRAn (v.1.18). The 3D and two-dimensional (2D) images were visualized, respectively using Dataviewer (v.0.4.8) and CTvox (v.3.3.0 r1401). The following parameters were measured: BMD, BV/TV, Tb.Th, SMI, Tb.N, Tb.Sp, cortical volume (Ct.V), cortical thickness (Ct.Th), cortical bone area (Ct.Ar) and total cortical bone area (Tt.Ar).

CT scans and analyses

High-resolution CT scans were acquired at baseline, 10 and 20 weeks after treatment by CT scanner (GE HealthCare, Lightspeed VCT). Axial imaging was performed with parameters 120 kV, 118 mA, a reconstruction diameter of 359 mm, a 512 × 512 matrix, 0.6-mm slice thickness, 0.77 × 0.77 × 0.6 mm voxel resolution and 570-mm source distance. Image reconstruction and 3D modeling were performed in 3DSlicer (v.5.6.2), with semiautomatic segmentation for regions of interest (ROIs). Femurs and lumbar vertebrae (L5) were analyzed for BMD, Tb.Th, Tb.N, BV/TV, Ct.V, Ct.Th, Cr.Ar and Tt.Ar.

SPECT/CT scans and analyses

EVs^{ABPC} were radiolabeled with ^{131}I. Specifically, EVs^{ABPC} (100 µg in 60 µl saline) and [^{131}I]NaI solution (2 ml, 10 mCi) were sequentially introduced into EP tubes preloaded with Iodogen (20 g), followed by purification using PD-10 columns and 0.22-µm filters. Radiolabeling efficiency was assessed from 3-µl aliquots and in vitro stability of ^{131}I-EVs^{ABPC} in saline at 37 °C was assessed over a 48-h incubation period using instant thin-layer chromatography.

Macaques received oral Lugol's solution (5% I_2, 0.5 ml per day) for 3 days before SPECT/CT imaging. Thereafter, animals were sedated with propofol and intravenously injected with purified ^{131}I-EVs$^{\text{ABPC}}$ or [^{131}I]NaI. Both the counts of empty and full needles, as well as injection times, were recorded pre- and post-injection. SPECT/CT images were performed at 1, 4 and 8 h post-injection using Symbia Inteva 6 (Siemens Healthineers). Images were acquired on a SPECT/CT dual-head gamma camera equipped with a high-energy general-purpose collimator. Whole-brain images were obtained by acquiring images for 20 s after each 3° rotation, spanning a total rotation of 180°, with a matrix size of 256 × 256 pixels. Subsequently, CT scans were conducted to generate fused SPECT/CT image. The ordered subset conjugate gradient-modified reconstruction algorithm (xSPECT Quant) was employed to determine averaged SUV and TBR, with the background SUV assessed in muscle tissue[49]. ROIs were delineated across the brain, and radioactive uptake activities in the brain were quantified at the various time points.

MRI data acquisition and processing

The macaques were scanned on a 3T imaging system (United Imaging Healthcare). T1-weighted anatomical images were acquired using a fast-spoiled gradient echo imaging sequence. Multi-shell diffusion-weighted images were obtained using a spin-echo planar imaging prototype sequence. Additionally, two *b*0 images with reversed phase-encoding were collected to correct for geometrical distortion.

The MRI structural image processing was characterized at two levels to identify morphological changes in macaques. At the volumetric level, we calculated the TIV, GMV and WMV using an SPM12 (v.r7771)-based VBM pipeline. Following DARTEL normalization (Inia19 template), tissue segmentation was performed to generate gray/white matter and cerebrospinal fluid probability maps. TIV was calculated as the sum of modulated GMV and WMV, with extracranial tissues removed through morphological mask processing. At the surface level, the brain surface was reconstructed using the HCP-NHP pipeline and cortical thickness and surface area were estimated.

The diffusion images were preprocessed using a common pipeline, which included distortion, motion and eddy current correction conducted by FMRIB Software Library (FSL, v.6.0.6.4). Preprocessed data were reconstructed by diffusion tensor imaging (DTI) models, then FA and RD were calculated (quantitative indicators widely concerned with brain aging)[50,51]. Whole-brain-wise FA/RD values were obtained by averaging across the FSL FAST-segmented white matter mask after affine alignment to the DTI space.

Detailed information for acquisition parameter and quality control can be found in the MRI section of the Reporting Summary.

MRI data analyses and metrics calculation

Change in each metric compared to the baseline was calculated at the whole-brain level and voxel level, respectively[52].

$$\text{value of metric} = \frac{(Post_{treatment} - \text{Pre}_{treatment})}{\text{Pre}_{treatment}} \times 100\%$$

Given the small sample size and deviation from a normal distribution, whole-brain level structural metrics were calculated. Kruskal–Wallis test for nonparametric comparisons were conducted, with Mann–Whitney *U*-tests (post hoc analysis) to reveal the pairwise between-group differences. Then permutation tests were performed for multiple comparisons to correct family-wise error (FWE)[53]: The permutation process was concurrently conducted for all pairwise comparisons among three groups. Permutation testing across three-group pairwise comparisons generated a null distribution (1,000 iterations) by retaining maximum *U*-values from relabeled data; true label-derived *U*-values determined FWE-corrected *P* values against this distribution.

In our voxel-wise comparison, we utilized a Kruskal–Wallis test for nonparametric comparisons to assess the voxel-wise metric across the three groups. Subsequently, Mann–Whitney *U*-tests were conducted as post hoc analyses to elucidate the pairwise differences between groups. Considering the relatively small sample size of our study, we did not apply multiple comparison corrections in voxel-wise level. Instead, we set a stringent significance level of $P < 0.05$ at the voxel level.

Bulk-seq quantification and quality control

Total RNA was extracted and sequenced using a NEBNext Ultra RNA library prep kit for Illumina with index codes for sample identification. Libraries were quantified and pooled according to effective concentrations for specific data output targets. Sequencing was performed on an Illumina platform. Raw data were processed into FASTQ format, filtered for low-quality reads with Fastp (v.0.23.1) and aligned to reference genomes (*Rattus norvegicus*, *Mus musculus*, *M. mulatta* and *Cervus nippon*). Transcript abundance was quantified using TPM via a custom script.

Proteomic analysis

Protein samples were lysed in SDT buffer (4% SDS and 10 mM Tris-HCl, pH 7.6) and protein concentrations were measured using a BCA assay kit. For each sample, 20 µg of protein was denatured and separated by SDS–PAGE (4–20% gel). Following Coomassie Blue staining, proteins were digested using filter-aided sample preparation with trypsin. Peptides were desalted and analyzed by LC–MS/MS with a TimsTOF Pro mass spectrometer coupled to a NanoElute system. Data were analyzed using MaxQuant (v.1.6.14), identifying 1,093 proteins annotated against the UniProt database.

Expression matrix analysis

Principal-component analysis (PCA) was prepared using the scatterplot3d package (v.0.3.42) in R (v.4.2.0) and DEGs/DEPs were identified using Limma (v.3.52.1) with a threshold of $P < 0.05$. For EVs, an absolute $\log_2$(fold change; FC) > 0.58 was used, while for peripheral blood and tissue samples, a stricter threshold ($\log_2$(FC) > 1.00) was applied. Heatmaps and clustering were visualized using TBtools-II (v.2.069) and ClusterGVis (v.0.0.9). The top 200 DEGs categorized as either upregulated or downregulated in young (8-week-old) and aged mice (18-month-old) were identified as 'young' and 'old' gene sets, respectively. Spearman's correlation analysis was conducted to evaluate correlations between these gene sets in the various groups compared to that in the vehicle group separately for both gene sets.

Multi-omics analysis

mRNA expression from RNA-seq and protein abundance from proteomics were normalized via $\log_2$ transformation. FCs were calculated as $\log_2$ ratios of experimental to control groups, with significant changes defined by $|\log_2(1.5)|$(~0.58). Genes and proteins were categorized into four groups: mRNA + protein both, mRNA only, protein only and no change. Moderated *t*-statistics were used to compute *P* values based on linear modeling with empirical Bayes moderation. All tests were two-sided and *P* values were adjusted for multiple comparisons using the Benjamini–Hochberg false discovery rate method. Data visualization was carried out with a scatter-plot in ggplot2 (v.3.4.2).

DNA methylation data generation and methylation age estimation

Whole-genome bisulfite sequencing data from mice and macaques were acquired on the Illumina NovaSeq 6000 platform with paired-end 150-bp reads. Quality control ensured >30× coverage and bisulfite conversion rate >99%. Methylation levels were processed through trimming, read alignment, and methylation extraction using metratio.py.

A mouse methylation age model was constructed using the GSE80672 dataset, achieving a 0.98 correlation and an average error of 1.616 months. The macaque methylation model, built from reduced representation bisulfite sequencing (NCBI SRA PRJNA610241), showed a 0.97 correlation and an average error of 1.425 years. These models were applied to predict methylation age in study samples.

ScRNA-seq and processing

Bone marrow samples from aged macaques were collected after 20 weeks of treatment (vehicle, EVs$^{\text{F-BMSC}}$, EVs$^{\text{ABPC}}$). A 10× Chromium Controller (10× Genomics) captured 10,000 cells per sample. Libraries were constructed using a Chromium single-cell 3′ gel bead and library V3 kit, and sequencing was performed on a NovaSeq 6000 platform (Illumina). Data were aligned with Cell Ranger (v.7.0.1) to the *M. mulatta* genome. To remove doublets from the scRNA-seq data, the scDblFinder package (v.1.17.1) was used to identify and eliminate doublets in each sample. After filtering cells based on gene expression and mitochondrial content, 28,558 high-quality cells were retained for analysis. The filtered gene expression matrix was analyzed using the Seurat package (v.4.3.0) in R software.

To correct for technical variability, data were normalized using the Harmony package (v.0.1.1). Cell-cycle effects were assessed, and clusters were identified at a resolution of 0.3. Clustering was visualized using *t*-distributed stochastic neighbor embedding (*t*-SNE). Marker genes for each cluster were identified with a Wilcoxon rank-sum test, and cell types were annotated using SingleR. A total of 23,511 cells from seven immune cell types were used to map the aging immune microenvironment in bone marrow. Differential expression was analyzed between the vehicle and EV-treated groups.

Gene set score analysis

Gene set score analysis for the SASP was performed using the AUCell package (v.1.18.1). The SenMayo gene set (Supplementary Table 6) was used as the input gene set, and area under the curve (AUC) values were calculated using the 'AUCell_calcAUC' function based on gene expression rankings. AUC scores were calculated for each cell to assess senescence, with cells exhibiting an AUC > 0.0345 classified as SASP positive.

GSEA

GSEA was conducted using the clusterProfiler package (v.4.9.3), with visualization facilitated by the GseaVis package (v.0.0.9). Genes were preranked based on their differential expression significance, employing the metric, $-\log_{10}(P) \times (\mathrm{FC})/\mathrm{abs}\,(\mathrm{FC})$. The Limma package was used to calculate P values and FC values. The normalized enrichment scores and P values for the pathways were computed via a one-sided permutation test (1,000 permutations) without multiple testing correction. The SenMayo gene set was specifically used to assess cellular senescence, whereas additional gene sets enriched in GO were acquired or compiled from the Molecular Signatures Database (MSigDB)[23]. Pathways with a minimum gene count of five and $P < 0.05$ were selected for subsequent analyses.

GO analysis

GO analysis of DEGs and DEPs was conducted using the Metascape (v.3.5)[54] and clusterProfiler packages. Results were visualized using the ggplot2 package and Cytoscape software (v.3.8.2). The rich factor for GO terms was calculated as the count of genes in a term divided by the total number of genes in the background.

Statistics and reproducibility

All experiments were conducted with simple randomization and blinding performed by an independent researcher before EV injection. During allocation, animals were randomly assigned to each group, with group allocation being concealed from the therapists, collectors and analysts. Throughout the experiment, the therapists remained blinded to the group allocations and handled all animals uniformly. They were also unaware of the specific treatments and provided consistent care across different groups. Following treatment, data were collected by individuals who were blinded to both the treatment and group allocation. Similarly, data were analyzed by analysts who remained blinded to treatment details. Groups were unblinded after the completion of the statistical analysis. No animals or data points were excluded and omitted from the analysis. All dots in graphs represent biological replicates. Before analysis, the data were tested for normality and homoscedasticity. For data passing the normality test, two-group comparisons were performed using a Student's *t*-test, whereas comparisons among more than two groups, we used one-way analysis of variance (ANOVA) for a single variable or two-way ANOVA for two variables, followed by the Bonferroni's post hoc test. For data without normal distribution, a Mann–Whitney *U*-test was used for comparisons among two groups and a Kruskal–Wallis test with Dunn's multiple comparisons was used for comparisons among more than two groups. Statistical significance was assessed using Prism (v.9.0), with significance defined as $P < 0.05$. Further statistical details can be found in the figure legends. Main experimental findings (such as micrographs, blots and hematology) were validated through three independently performed experiments. All replications presented similar results. All reagents or resources are listed in Supplementary Tables 1–8.

Reporting summary

Further information on research design is available in the Nature Portfolio Reporting Summary linked to this article.

Data availability

All omics data generated in this study have been deposited in the Gene Expression Omnibus database (transcriptome) and iProX database (proteome), which have been publicly released. The transcriptomic data of EVs, cells and mice (including serum and tissues) are accessible via GSE289038. The transcriptomic data of rhesus macaques are accessible via GSE273278. For scRNA-seq of rhesus macaques, the data are accessible via GSE288582. For proteomics of EVs, the data are accessible via PXD064039. Additionally, all data associated with this study are present in the paper or the Supplementary Information. Source data are provided with the paper.

Code availability

The code used in this study is available at GitHub (https://github.com/finalbeibeiyu/Nature_aging).

References

1. Prince, M. J. et al. The burden of disease in older people and implications for health policy and practice. *Lancet* **385**, 549–562 (2015).
2. Childs, B. G. et al. Senescent cells: an emerging target for diseases of ageing. *Nat. Rev. Drug Discov.* **16**, 718–735 (2017).
3. Brunet, A., Goodell, M. A. & Rando, T. A. Ageing and rejuvenation of tissue stem cells and their niches. *Nat. Rev. Mol. Cell Biol.* **24**, 45–62 (2023).
4. López-Otín, C., Blasco, M. A., Partridge, L., Serrano, M. & Kroemer, G. Hallmarks of aging: an expanding universe. *Cell* **186**, 243–278 (2023).
5. Sanz-Ros, J. et al. Small extracellular vesicles from young adipose-derived stem cells prevent frailty, improve health span, and decrease epigenetic age in old mice. *Sci. Adv.* **8**, eabq2226 (2022).
6. Mehdipour, M. et al. Rejuvenation of three germ layers tissues by exchanging old blood plasma with saline-albumin. *Aging* **12**, 8790–8819 (2020).
7. Castellano, J. M. et al. Human umbilical cord plasma proteins revitalize hippocampal function in aged mice. *Nature* **544**, 488–492 (2017).

8. Galipeau, J. & Sensébé, L. Mesenchymal stromal cells: clinical challenges and therapeutic opportunities. *Cell Stem Cell* **22**, 824–833 (2018).
9. Zhang, K. & Cheng, K. Stem cell-derived exosome versus stem cell therapy. *Nat. Rev. Bioeng.* **1**, 608–609 (2023).
10. Mathieu, M., Martin-Jaular, L., Lavieu, G. & Théry, C. Specificities of secretion and uptake of exosomes and other extracellular vesicles for cell-to-cell communication. *Nat. Cell Biol.* **21**, 9–17 (2019).
11. Li, X. H. et al. Physiological and pathological insights into exosomes in the brain. *Zool. Res.* **41**, 365–372 (2020).
12. Chen, X. et al. Small extracellular vesicles from young plasma reverse age-related functional declines by improving mitochondrial energy metabolism. *Nat. Aging* **4**, 814–838 (2024).
13. Lei, J. et al. Exosomes from antler stem cells alleviate mesenchymal stem cell senescence and osteoarthritis. *Protein Cell* **13**, 220–226 (2022).
14. Hoang, D. M. et al. Stem cell-based therapy for human diseases. *Signal Transduct. Target. Ther.* **7**, 272 (2022).
15. Han, Y. et al. The secretion profile of mesenchymal stem cells and potential applications in treating human diseases. *Signal Transduct. Target. Ther.* **7**, 92 (2022).
16. Qin, T. et al. A population of stem cells with strong regenerative potential discovered in deer antlers. *Science* **379**, 840–847 (2023).
17. Landete-Castillejos, T. et al. Antlers - evolution, development, structure, composition, and biomechanics of an outstanding type of bone. *Bone* **128**, 115046 (2019).
18. Sharpless, N. E. & DePinho, R. A. How stem cells age and why this makes us grow old. *Nat. Rev. Mol. Cell Biol.* **8**, 703–713 (2007).
19. Heezen, L. G. M. et al. Spatial transcriptomics reveal markers of histopathological changes in Duchenne muscular dystrophy mouse models. *Nat. Commun.* **14**, 4909 (2023).
20. Luo, W. D. et al. Age-related self-DNA accumulation may accelerate arthritis in rats and in human rheumatoid arthritis. *Nat. Commun.* **14**, 4394 (2023).
21. Yin, A. et al. Exercise-derived peptide protects against pathological cardiac remodeling. *eBioMedicine* **82**, 104164 (2022).
22. Zhou, Y. et al. Senolytics improve bone forming potential of bone marrow mesenchymal stem cells from aged mice. *NPJ Regen. Med.* **6**, 34 (2021).
23. Saul, D. et al. A new gene set identifies senescent cells and predicts senescence-associated pathways across tissues. *Nat. Commun.* **13**, 4827 (2022).
24. Khosla, S. Pathogenesis of age-related bone loss in humans. *J. Gerontol. A Biol. Sci. Med. Sci.* **68**, 1226–1235 (2013).
25. Wang, L., You, X., Zhang, L., Zhang, C. & Zou, W. Mechanical regulation of bone remodeling. *Bone Res.* **10**, 16 (2022).
26. Petkovich, D. A. et al. Using DNA methylation profiling to evaluate biological age and longevity interventions. *Cell Metab.* **25**, 954–960.e6 (2017).
27. Yang, L. et al. Extracellular vesicle-mediated delivery of circular RNA SCMH1 promotes functional recovery in rodent and nonhuman primate ischemic stroke models. *Circulation* **142**, 556–574 (2020).
28. Zhou, R. et al. Endocrine role of bone in the regulation of energy metabolism. *Bone Res.* **9**, 25 (2021).
29. Cassady, K., Ruitenberg, M. F. L., Reuter-Lorenz, P. A., Tommerdahl, M. & Seidler, R. D. Neural dedifferentiation across the lifespan in the motor and somatosensory systems. *Cereb. Cortex* **30**, 3704–3716 (2020).
30. Huang, K. et al. A hierarchical 3D-motion learning framework for animal spontaneous behavior mapping. *Nat. Commun.* **12**, 2784 (2021).
31. Brinkman, J. & Kuypers, H. G. Cerebral control of contralateral and ipsilateral arm, hand and finger movements in the split-brain rhesus monkey. *Brain* **96**, 653–674 (1973).
32. Chiou, K. et al. Rhesus macaques as a tractable physiological model of human ageing. *Phil. Trans. R. Soc. B* **375**, 20190612 (2020).
33. Tian, X. G. et al. Inflammation-mediated age-dependent effects of casein kinase 2-interacting protein-1 on osteogenesis in mesenchymal stem cells. *Chin. Med. J.* **133**, 1935–1942 (2020).
34. Li, C. J. et al. Senescent immune cells release grancalcin to promote skeletal aging. *Cell Metab.* **33**, 1957–1973.e6 (2021).
35. Zatorre, R. J., Fields, R. D. & Johansen-Berg, H. Plasticity in gray and white: neuroimaging changes in brain structure during learning. *Nat. Neurosci.* **15**, 528–536 (2012).
36. Wagstyl, K., Ronan, L., Goodyer, I. M. & Fletcher, P. C. Cortical thickness gradients in structural hierarchies. *Neuroimage* **111**, 241–250 (2015).
37. Goto, M. et al. Advantages of using both voxel- and surface-based morphometry in cortical morphology analysis: a review of various applications. *Magn. Reson. Med. Sci.* **21**, 41–57 (2022).
38. Koenig, S. et al. Age dependent hypothalamic and pituitary responses to novel environment stress or lipopolysaccharide in rats. *Front. Behav. Neurosci.* **12**, 55 (2018).
39. Bian, Z. et al. Effects of species-relevant auditory stimuli on stress in cats exposed to novel environment. *J. Appl. Anim. Welf. Sci.* **28**, 318–327 (2023).
40. Kong, D. et al. PKA regulatory IIα subunit is essential for PGD2-mediated resolution of inflammation. *J. Exp. Med.* **213**, 2209–2226 (2016).
41. Huang, R. et al. Circ_0000811 acts as a miR-15b sponge and inhibits Prkar2a-mediated JAK2/STAT1 pathway to attenuate cerebral ischemic vertigo. *Cell Death Discov.* **8**, 247 (2022).
42. Rao, S. et al. Extracellular vesicles from human urine-derived stem cells delay aging through the transfer of PLAU and TIMP1. *Acta Pharm. Sin. B* **14**, 1166–1186 (2024).
43. Robbins, P. D. Extracellular vesicles and aging. *Stem Cell Investig.* **4**, 98 (2017).
44. Bethlehem, R. A. I. et al. Brain charts for the human lifespan. *Nature* **604**, 525–533 (2022).
45. Yang, Y. et al. Metformin decelerates aging clock in male monkeys. *Cell* **187**, 6358–6378.e6329 (2024).
46. van Niel, G. et al. Challenges and directions in studying cell-cell communication by extracellular vesicles. *Nat. Rev. Mol. Cell Biol.* **23**, 369–382 (2022).
47. Kalluri, R. & LeBleu, V. S. The biology, function, and biomedical applications of exosomes. *Science* **367**, eaau6977 (2020).
48. Breda, L. et al. In vivo hematopoietic stem cell modification by mRNA delivery. *Science* **381**, 436–443 (2023).
49. Zhou, C. et al. Prospective study comparing [(99m)Tc] Tc-DP-FAPI quantitative SPECT/CT with [(68)Ga]Ga-FAPI-04 PET/CT in patients with gastrointestinal tumors. *Mol. Pharm.* **21**, 5297–5304 (2024).
50. Beck, D. et al. White matter microstructure across the adult lifespan: a mixed longitudinal and cross-sectional study using advanced diffusion models and brain-age prediction. *Neuroimage* **224**, 117441 (2021).
51. Shamir, I. & Assaf, Y. Tutorial: a guide to diffusion MRI and structural connectomics. *Nat. Protoc.* **20**, 317–335 (2025).
52. Cagol, A. et al. Association of brain atrophy with disease progression independent of relapse activity in patients with relapsing multiple sclerosis. *JAMA Neurol.* **79**, 682–692 (2022).
53. Wang, S., Su, Q., Qin, W., Yu, C. & Liang, M. Both fine-grained and coarse-grained spatial patterns of neural activity measured by functional MRI show preferential encoding of pain in the human brain. *Neuroimage* **272**, 120049 (2023).
54. Zhou, Y. et al. Metascape provides a biologist-oriented resource for the analysis of systems-level datasets. *Nat. Commun.* **10**, 1523 (2019).

Acknowledgements

We thank all members of the Huang, Qiu and Yao laboratories for discussions. We thank R. Zhao (Fourth Military Medical University, FMMU) for his assistance with MRI data processing and analysis. We thank C. Yu, D. Si and Z. Gong at the Analysis & Testing Laboratory for Life Sciences and Medicine of FMMU for their assistance with NTA analysis of EVs. We thank F. Kang and J. Ye (Department of Nuclear Medicine, Xijing Hospital) for their assistance of SPECT/CT. We thank S. Zhao and Y. Li (FMMU) for the scanning transmission and electron microscope technical assistance. We thank J. Hu (FMMU) for flow cytometry technical assistance. We thank Z. Hu (KIZ) for raising rhesus macaques and access to the monkey facility. We thank S. Dong, H. Zhu, Y. Zhang, Y. Li and M. Yuan (KIZ) for conducting a behavior assessment of rhesus macaques. We thank X. Zhu (KIZ) and N. Liu (State Key Laboratory of Brain and Cognitive Science, Institute of Biophysics, Chinese Academy of Sciences) for analyzing MRI data. We thank R. Heller (Section for Computational and RNA Biology, Department of Biology, University of Copenhagen) for reviewing the manuscript and offering valuable suggestions. We thank Shenzhen Acegen Technology Co. for guidance in data analysis and statistics for technical guidance in whole-genome bisulfite sequencing library preparation. We thank Novogene Co. for providing technical support with RNA-seq. We thank OE Biotech for providing technical support with scRNA-seq. The work was supported by the National Key Research and Development Program of China (2024YFA1802500 (J.H.) and 2023YFC2509905 (Z. Luo)); National Natural Science Foundation of China (82122043 (J.H.), 82372404 (J.H.) and 32225009 (Q.Q.)); the Ministry of Science and Technology of China (STI2030-Major Project grant 2021ZD0200900 (Y. Yao); STI2030-Major Projects grants 2022ZD0205100 (J.W.) and 2021ZD0203900 (J.W.)); the Yunnan Department of Science and Technology (202305AH340006 (Y. Yao)); and the New Cornerstone Investigator Program (W.W.).

Author contributions

J.H., Q.Q., Z. Luo, W.W., Y. Yao and D.W. conceptualized and designed the study. Y.H., B.Y., M. Qin, T.Q., Y.W., C.Z., T.X., B. Xue, Yali Zhang, H.H., X.Y., Y.J., M. Qiu, B. Xia, T.M., S.L., H.W., Xue Gao, Y. Yang, L.G., Yongfeng Zhang, Z.W., H.S., Xueli Gao, Z.H., L.L., D.W. and Z. Li provided technical, methodological, material support, and resources. Y.H., B.Y., M. Qin, T.Q., Y.W., C.Z. and T.X. contributed to the acquisition of data. Y.H., B.Y., M. Qin, T.Q., Y.W., C.Z., Y.X. and Y. Yuan analyzed and interpreted the results. Y.H., B.Y., M.Qin, T.Q., Y.W., C.Z., Y.X., Y. Yuan, T.X., B. Xue, Y.J., Yali Zhang, B. Xia, T.M., S.L., H.W., Xue Gao, Y. Yang, L.G., Yongfeng Zhang, Z.W., H.S. and Xueli Gao provided formal analysis of the data and data curation. Y.H., M. Qin, B.Y. and T.Q. prepared the first manuscript. D.W., Y. Yao, W.W., Z. Luo, Q.Q. and J.H. revised and edited the manuscript. All authors agreed to submit the manuscript, read and approve the final draft and take full responsibility for its content, including the accuracy of the data.

Competing interests

The authors declare no competing interests.

Additional information

Extended data are available for this paper at https://doi.org/10.1038/s43587-025-00918-x.

Supplementary information The online version contains supplementary material available at https://doi.org/10.1038/s43587-025-00918-x.

Correspondence and requests for materials should be addressed to Yonggang Yao, Wen Wang, Zhuojing Luo, Qiang Qiu or Jinghui Huang.

Peer review information *Nature Aging* thanks Hirotaka Iijima, Andrei Seluanov and the other, anonymous, reviewer(s) for their contribution to the peer review of this work.

Reprints and permissions information is available at www.nature.com/reprints.

Yiming Hao [1,11], **Beibei Yu** [1,2,11], **Mingze Qin** [1,11], **Tao Qin** [3,11], **Jianhong Wang** [4,5,11], **Yitao Wei**[1], **Chengxiang Zhao**[1], **Yaowen Xing**[6], **Yuan Yuan**[3], **Tingfeng Xue**[3], **Borui Xue**[1], **Yali Zhang**[4], **Hongdi Huang**[4], **Xiaomei Yu**[4], **Yunchao Ji**[4], **Minghao Qiu**[4], **Yufang Zhou**[4], **Bing Xia**[1], **Teng Ma**[1], **Shengyou Li**[1], **Haining Wu**[1], **Xue Gao**[1], **Yujie Yang**[1], **Lingli Guo**[1], **Yongfeng Zhang**[1,2], **Zhenguo Wang**[1], **Huiling Sun**[3], **Xueli Gao**[3], **Zujian Huang**[7], **Longbao Lv**[4], **Dongdong Wu** [4,5,8], **Zhipeng Li**[9,10], **Yonggang Yao** [4,5,8] ✉, **Wen Wang** [3] ✉, **Zhuojing Luo** [1] ✉, **Qiang Qiu** [3] ✉ **& Jinghui Huang** [1] ✉

[1]Department of Orthopaedics, Xijing Hospital, Fourth Military Medical University, Xi'an, China. [2]Department of Neurosurgery, The Second Affiliated Hospital, Xi'an Jiaotong University, Xi'an, China. [3]New Cornerstone Science Laboratory, Shaanxi Key Laboratory of Qinling Ecological Intelligent Monitoring and Protection, School of Ecology and Environment, Northwestern Polytechnical University, Xi'an, China. [4]National Research Facility for Phenotypic & Genetic Analysis of Model Animals (Primate Facility), and National Resource Center for Non-Human Primates, Kunming Institute of Zoology, the Chinese Academy of Sciences, Kunming, China. [5]Key Laboratory of Genetic Evolution and Animal Models, Yunnan Key Laboratory of Animal Models and Human Disease Mechanisms, KIZ-CUHK Joint Laboratory of Bioresources and Molecular Research in Common Diseases, Kunming Institute of Zoology, Chinese Academy of Sciences, Kunming, China. [6]United Imaging Healthcare, Shanghai, China. [7]School of Life Sciences, Xidian University, Xi'an, China. [8]Kunming College of Life Science, University of Chinese Academy of Sciences, Kunming, China. [9]Institute of Antler Science and Product Technology, Changchun Sci-Tech University, Changchun, China. [10]College of Traditional Chinese Medicine, Jilin Agricultural University, Changchun, China. [11]These authors contributed equally: Yiming Hao, Beibei Yu, Mingze Qin, Tao Qin, Jianhong Wang. ✉e-mail: yaoyg@mail.kiz.ac.cn; wenwang@nwpu.edu.cn; zjluo@fmmu.edu.cn; qiuqiang@nwpu.edu.cn; huangjh@fmmu.edu.cn

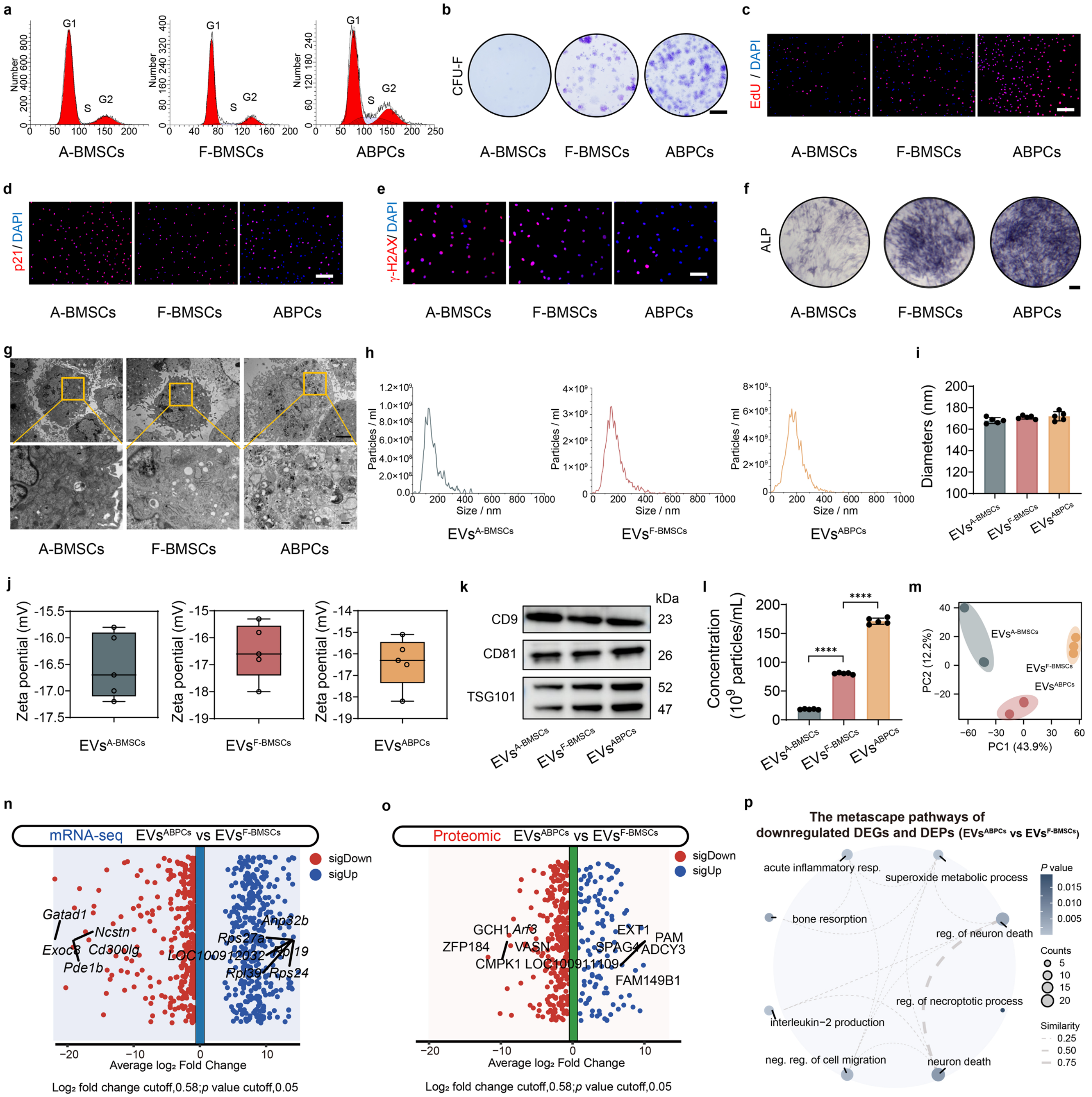

Extended Data Fig. 1 | Characterization of ABPCs and EVs$^{\mathrm{ABPCs}}$. **a**, Flow cytometry analysis of the cell-cycle phase distribution in A-BMSCs, F-BMSCs, and ABPCs. **b**–**f**, Representative images depicting staining for CFU-F (**b**), EdU (**c**), p21 (**d**), γ-H2AX (**e**) and ALP (**f**) staining of cells from the three cell types. Scale bar, 5 mm (**b**), 200 μm (**c** and **d**), 100 μm (**e**) or 3 mm (**f**). **g**, Representative morphological images of cells by transmission electron microscopy. Scale bar, 2 mm (top), 200 μm (bottom). **h**, Diameter distribution of EVs derived from different cell types by NTA. **i**, Mean diameters of EVs from three distinct cell sources ($n = 5$). **j**, Zeta potential of the EVs was determined by tunable resistance pulse sensing (TRPS) ($n = 5$). Data points are represented by circles. Boxplots display median (center line), IQR (box limits), and 1.5 × IQR (whiskers). **k**, CD9, CD81, and TSG101 protein levels in EVs from three distinct cell sources were determined by western blotting. **l**, Mean concentrations of EVs from three distinct cell sources ($n = 5$). **m**, PCA of the transcriptomic characteristics in EVs$^{\mathrm{A\text{-}BMSCs}}$, EVs$^{\mathrm{F\text{-}BMSCs}}$, and EVs$^{\mathrm{ABPCs}}$. **n**,**o**, Volcano plot illustrated DEGs (**n**) and DEPs (**o**) between EVs$^{\mathrm{ABPCs}}$ and EVs$^{\mathrm{F\text{-}BMSCs}}$. **p**, Network diagram represented the metascape pathways of downregulated DEGs and DEPs in EVs$^{\mathrm{ABPCs}}$ compared to EVs$^{\mathrm{F\text{-}BMSCs}}$. Each node corresponds to a specific biological process, and the size of the node is proportional to the enrichment score. The similarity between pathways is indicated by the thickness of the connecting lines. Statistical significance was calculated by one-way ANOVA with Bonferroni's multiple comparisons test (**i** and **l**). Data are presented as mean ± s.d. ****$P < 0.0001$.

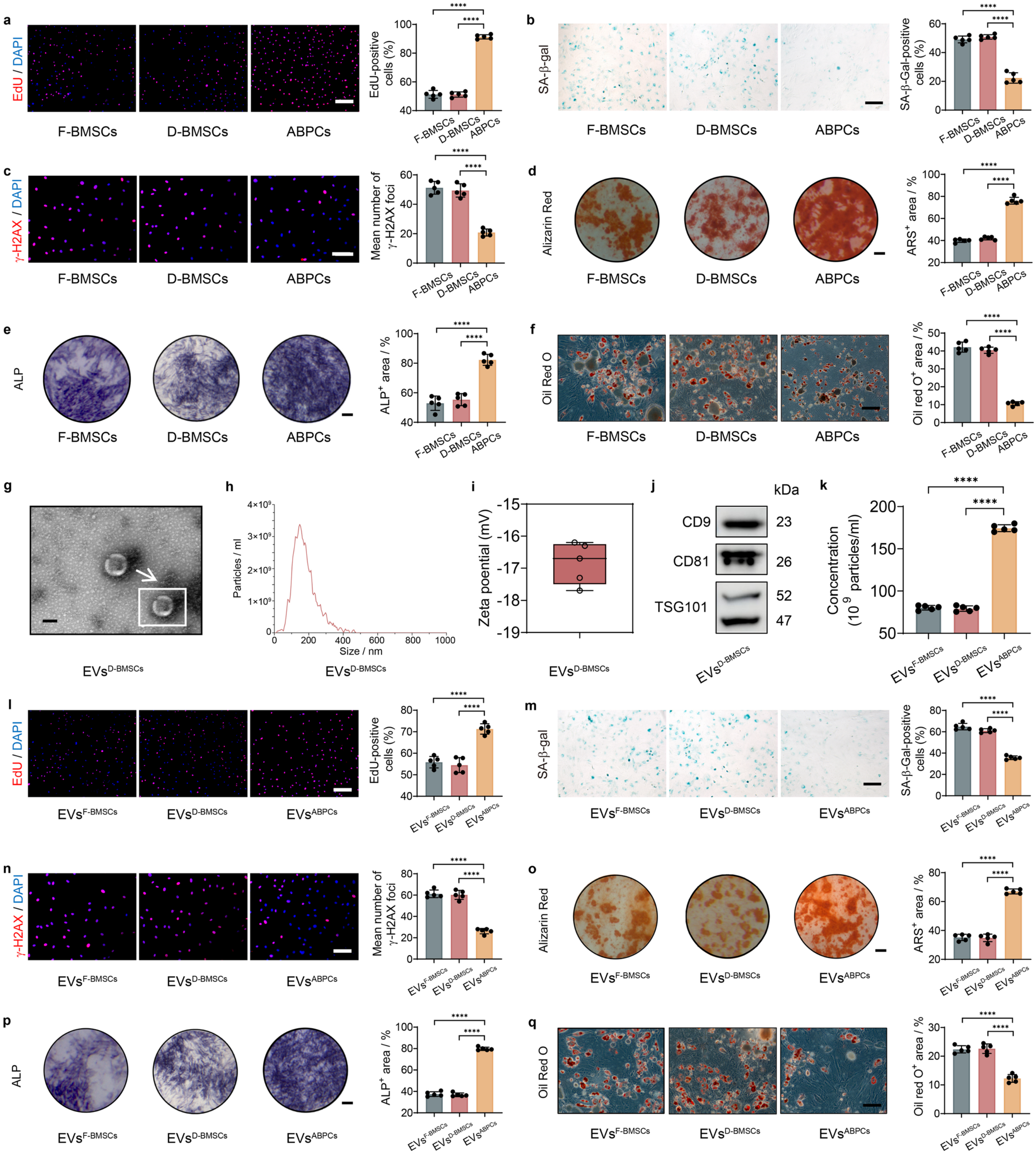

Extended Data Fig. 2 | See next page for caption.

Extended Data Fig. 2 | D-BMSCs and EVs$^{\text{D-BMSCs}}$ demonstrate similar rejuvenating capabilities compared to F-BMSCs and EVs$^{\text{F-BMSCs}}$. **a**, Representative images of EdU staining and the quantitative analysis of EdU-positive cells (*n* = 5). Scale bar, 200 μm. **b**, Representative images of SA-β-Gal staining and their quantitative analysis (*n* = 5). Scale bar, 200 μm. **c**, Representative images of γ-H2AX staining of cells and their quantitative analysis (*n* = 5). Scale bar, 100 μm. **d**–**f**, Representative images of ARS (**d**), ALP (**e**), and Oil Red O (**f**) staining of cells and their quantitative analysis (*n* = 5). Scale bar, 3 mm (**d** and **e**) or 100 μm (**f**). **g**, Morphology of EVs isolated from D-BMSCs (EVs$^{\text{D-BMSCs}}$), Scale bar, 100 nm. **h**, Diameter distribution of EVs$^{\text{D-BMSCs}}$ as revealed by NTA. **i**, The zeta potential of the EVs$^{\text{D-BMSCs}}$. The data points are represented by circles. Boxplots display median (center line), IQR (box limits), and 1.5 × IQR (whiskers). **j**, CD9, CD81, and TSG101 protein levels in EVs$^{\text{D-BMSCs}}$ by western blotting. **k**, Mean EVs concentration in different EVs groups (*n* = 5). **l**, Representative images of EdU staining of A-BMSCs treated with different EVs and their quantitative analysis (*n* = 5). Scale bar, 200 μm. **m**, Representative images of SA-β-Gal staining of A-BMSCs treated with different EVs and their quantitative analysis (*n* = 5). Scale bar, 200 μm. **n**, Representative images of γ-H2AX staining of A-BMSCs treated with different EVs and their quantitative analysis (*n* = 5). Scale bar, 100 μm. **o**–**q**, Representative images of ARS (**o**), ALP (**p**), and Oil Red O (**q**) staining of A-BMSCs treated with different EVs and their quantitative analysis (*n* = 5). Scale bar, 3 mm (**o** and **p**) or 100 μm (**q**). Statistical significance was calculated by one-way ANOVA with Bonferroni's multiple comparisons test (**a**–**f** and **k**–**q**). Data are presented as mean ± s.d. $^{****}P < 0.0001$.

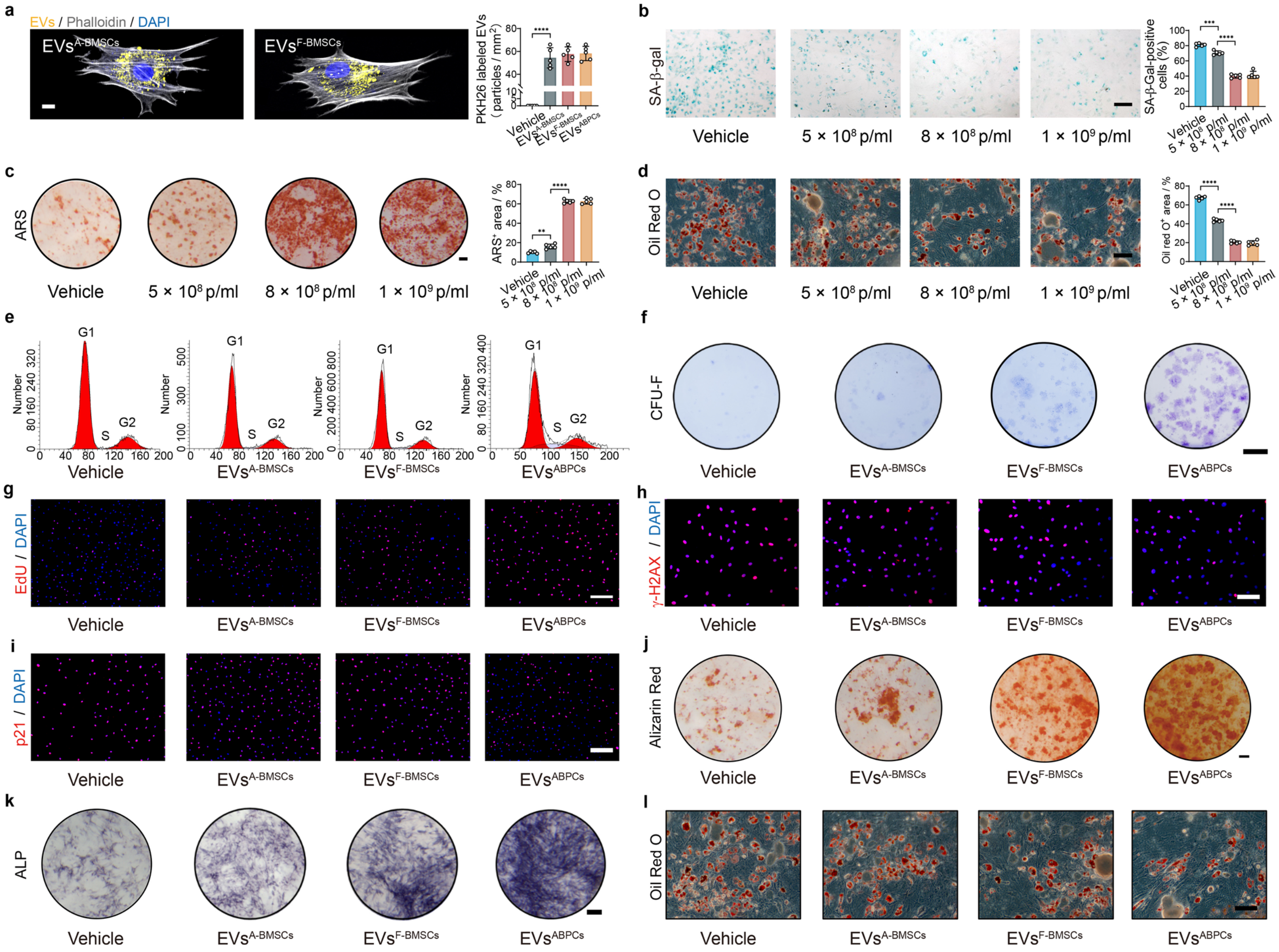

Extended Data Fig. 3 | Rejuvenation of A-BMSCs after EVs$^{\mathrm{ABPCs}}$ treatment. **a**, Internalization of PKH26-labeled EVs$^{\mathrm{A\text{-}BMSCs}}$ and EVs$^{\mathrm{F\text{-}BMSCs}}$ (yellow) within A-BMSCs stained with DAPI (blue) and phalloidin (white), and quantification of PKH26-labeled EVs in A-BMSCs (*n* = 5). Scale bar, 10 μm. **b**–**d**, Representative images of SA-β-Gal (**b**), ARS (**c**), and Oil Red O (**d**) staining in A-BMSCs following EVs$^{\mathrm{ABPCs}}$ treatment in a dose-dependent manner and their quantitative analysis (*n* = 5). Scale bar, 200 μm (**b**), 3 mm (**c**), or 100 μm (**d**). **e**, Flow cytometric analysis was performed to assess the cell-cycle phase in A-BMSCs treated with different EVs. **f**–**l**, Representative images of CFU-F (**f**), EdU (**g**), γ-H2AX (**h**), p21 (**i**), ARS (**j**), ALP (**k**), and Oil red O (**l**) staining in A-BMSCs following different EVs treatment. Scale bar, 5 mm (**f**), 200 μm (**g** and **i**), 100 μm (**h** and **l**) or 3 mm (**j** and **k**). Statistical significance was calculated by one-way ANOVA with Bonferroni's multiple comparisons test (**a**–**d**). Data are presented as mean ± s.d. $^{**}P < 0.01$, $^{***}P < 0.001$, and $^{****}P < 0.0001$.

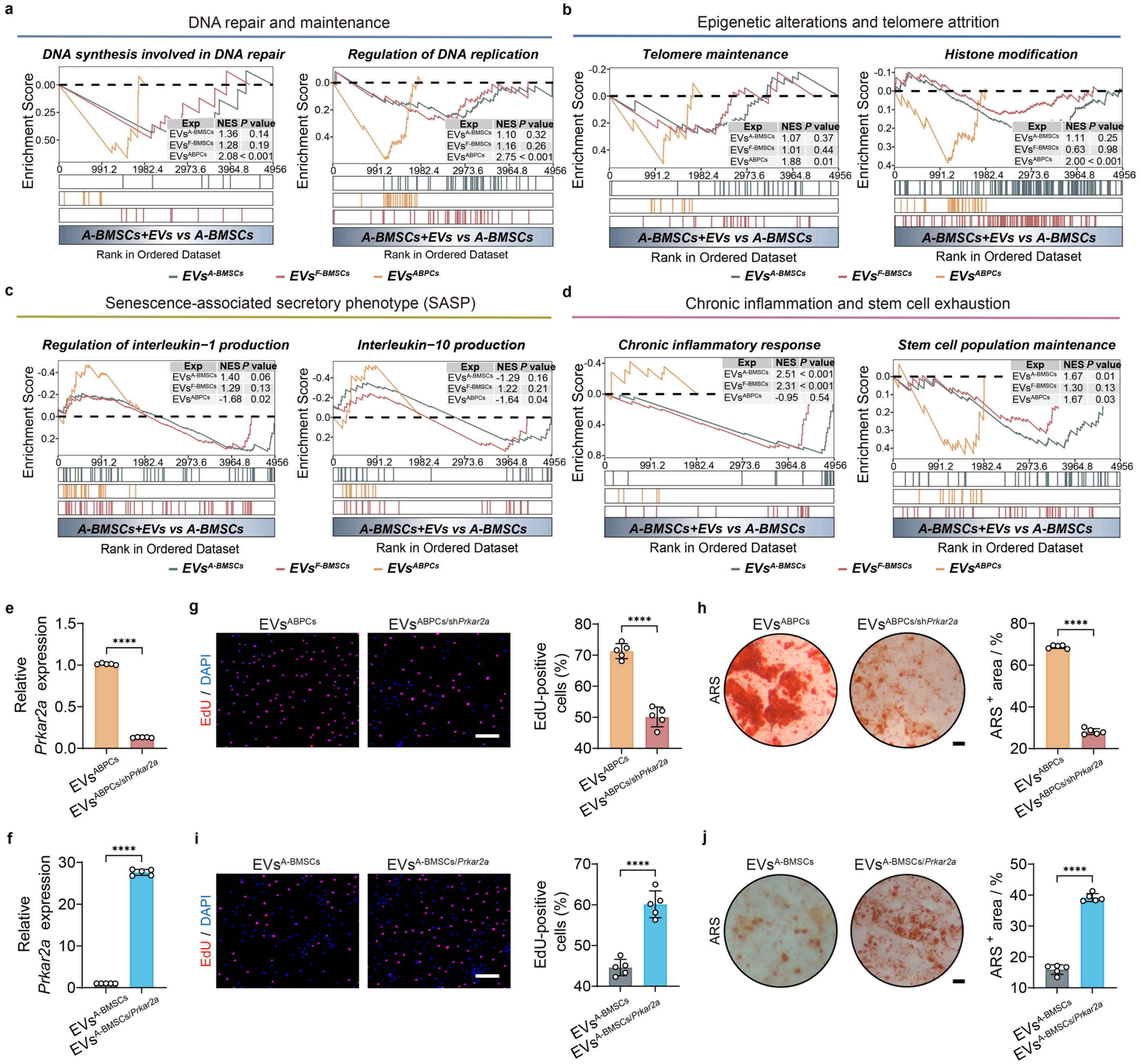

Extended Data Fig. 4 | EVs$^{\mathrm{ABPCs}}$ rejuvenate A-BMSCs in transcriptomic signature and phenotype. a–d, GSEA analysis revealed the regulation of DNA repair and maintenance (**a**), epigenetic alterations and telomere attrition (**b**), SASP (**c**), and chronic inflammation and stem cell exhaustion (**d**) in A-BMSCs following different EVs treatments. **e**, The relative expression levels of *Prkar2a* in in EVs$^{\mathrm{ABPCs}}$ treated and EVs$^{\mathrm{ABPCs/sh}Prkar2a}$ treated A-BMSCs by qPCR (*n* = 5). **f**, The relative expression levels of *Prkar2a* in in EVs$^{\mathrm{A\text{-}BMSCs}}$ treated and EVs$^{\mathrm{A\text{-}BMSCs/}Prkar2a}$ treated A-BMSCs by qPCR (*n* = 5). **g**,**h**, Representative images of EdU (**g**) and ARS (**h**) staining in A-BMSCs treated with EVs$^{\mathrm{ABPCs}}$ and EVs$^{\mathrm{ABPCs/sh}Prkar2a}$ and their quantitative analysis (*n* = 5). Scale bar, 200 μm (**g**) or 3 mm (**h**). **i**,**j**, Representative images of EdU (**i**) and ARS (**j**) staining in A-BMSCs treated with EVs$^{\mathrm{A\text{-}BMSCs}}$ and EVs$^{\mathrm{A\text{-}BMSCs/}Prkar2a}$ and their quantitative analysis (*n* = 5). Scale bar, 200 μm (**i**) or 3 mm (**j**). Statistical significance was calculated by two-tailed Student's *t*-test (**e**–**j**). Datr are presented as mean ± s.d. ****$P < 0.0001$.

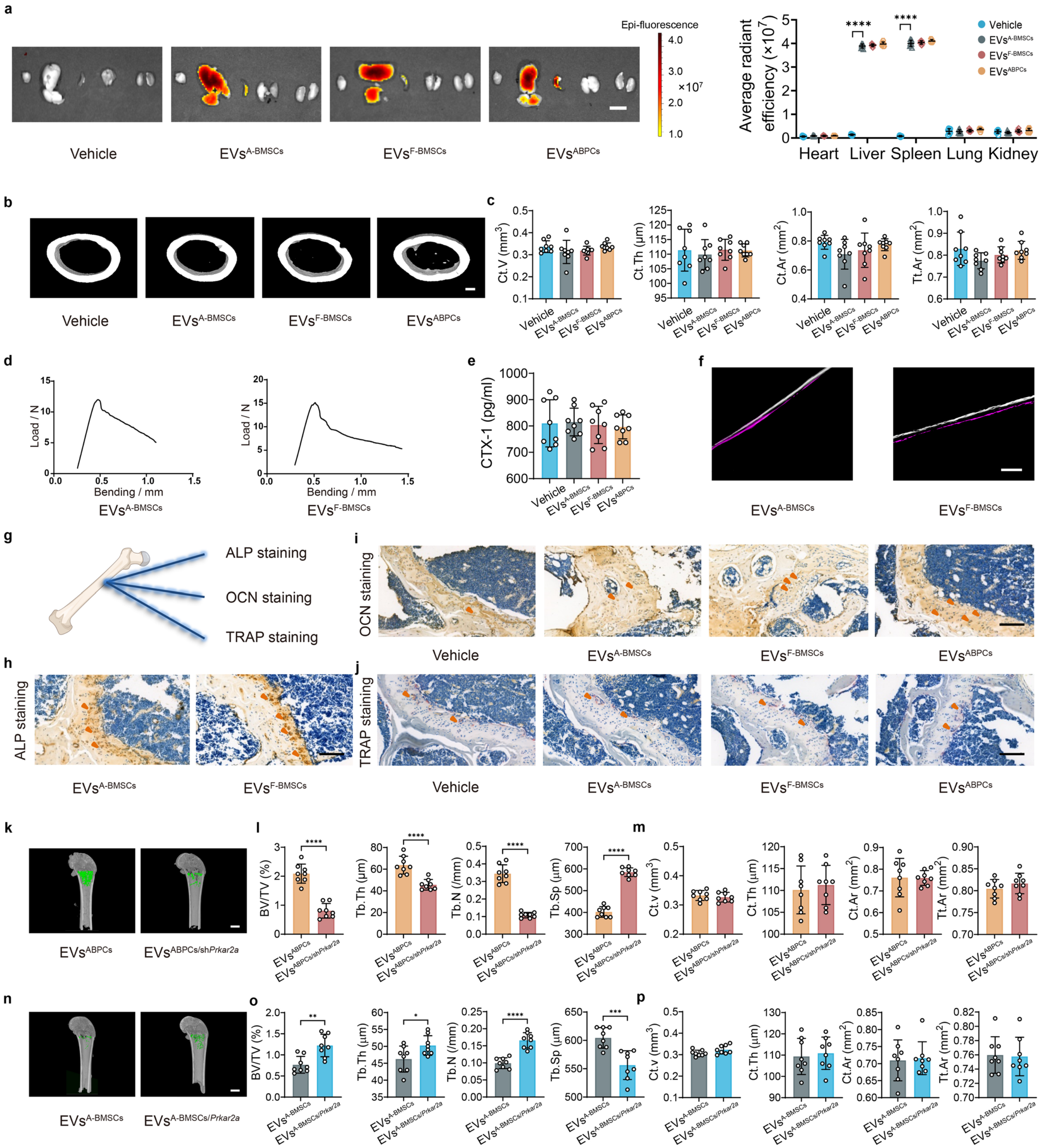

Extended Data Fig. 5 | EVs^{ABPCs} mitigate age-related bone loss in aged mice. **a**, *Ex vivo* fluorescence images and average radiant efficiency of organs at 48 h after tail vein injection of DiR-labeled EVs. From left to right: heart, liver, spleen, lung, kidney (*n* = 8). Scale bar, 1,000 μm. **b**, Representative micro-CT images of femoral cortical bone. Scale bar, 150 μm. **c**, Quantitative analysis of cortical bone parameters, including Ct.V, Ct.Th, Ct.Ar, and Tt.Ar from different groups (*n* = 8). **d**, Representative images of the mechanical strength of femurs from mice treated with EVs$^{A\text{-}BMSCs}$ or EVs$^{F\text{-}BMSCs}$. **e**, The concentration of serum CTX-1 (*n* = 8). **f**, Representative images of newly formed trabecular bone, labeled with calcein AM (magenta) and alizarin red (white) in mice treated with EVs$^{F\text{-}BMSCs}$ and EVs$^{A\text{-}BMSCs}$. Scale bar, 50 μm. **g**, A schematic diagram of immunohistochemical staining (ALP, OCN and TRAP staining) in femurs. **h**–**j**, Representative images of ALP (**h**), OCN (**i**), and TRAP (**j**) staining in femurs from mice treated with EVs, with the ALP-, OCN-, or TRAP-positive cells presented by orange arrow. Scale bar, 100 μm. **k**–**m**, Representative micro-CT reconstruction images (**k**) and quantitative analysis of the trabecular (**l**) and cortical bone (**m**) from mice treated with EVs^{ABPCs} or EVs$^{ABPCs/shPrkar2a}$ (*n* = 8). Scale bar, 1,500 μm. **n**–**p**, Representative micro-CT reconstruction images (**n**) and quantitative analysis of the trabecular (**o**) and cortical bone (**p**) in mice treated with EVs$^{A\text{-}BMSCs}$ or EVs$^{A\text{-}BMSCs/Prkar2a}$ (*n* = 8). Scale bar, 1,500 μm. Statistical significance was determined by one-way ANOVA with Bonferroni's multiple comparisons test (**a**, **c**, and **e**), two-tailed Student's *t*-test (**l**, **m**, **o**, and **p** in addition to the third plot), or nonparametric Mann–Whitney test (the third plot of **p**). Data are presented as mean ± s.d. $^{*}P < 0.05$, $^{**}P < 0.01$, $^{***}P < 0.001$, and $^{****}P < 0.0001$.

https://doi.org/10.1038/s43587-025-00918-x

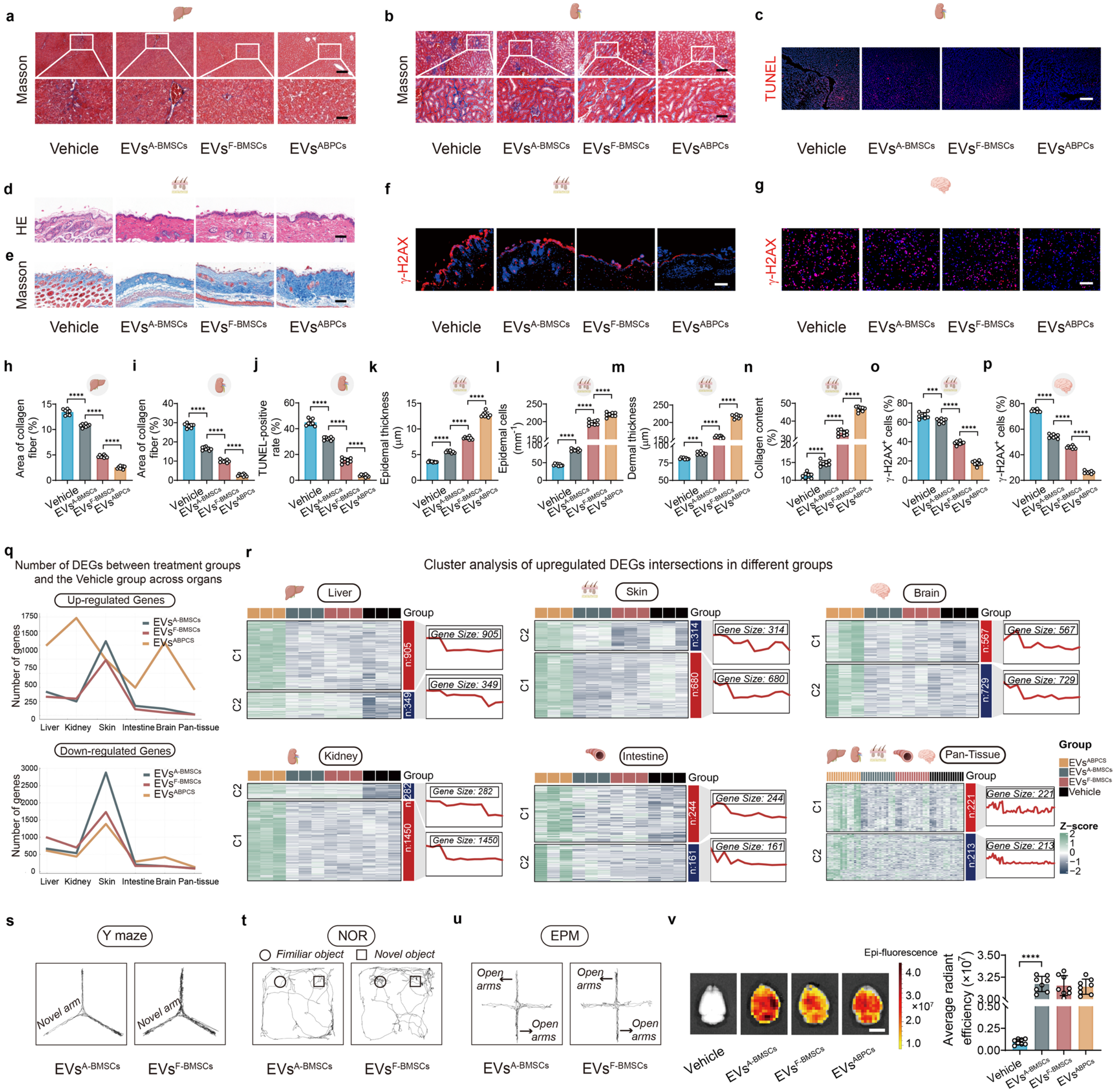

Extended Data Fig. 6 | The effects of EVs^{ABPCs} mitigate organ senescence in aged mice. a,**b**, Representative images of Masson's trichrome staining for liver (**a**) and kidney (**b**). Scale bar,100 μm (top of **a** and **b**) or 350 μm (bottom of **a** and **b**). **c**, Representative images of immunofluorescence staining of TUNEL in the kidney. Scale bar, 200 μm. **d**,**e**, Representative images of H&E (**d**) and Masson's trichrome (**e**) staining for skin. Scale bar, 50 μm (**d**) or 100 μm (**e**). **f**, Representative immunofluorescence images of γ-H2AX in skin. Scale bar, 500 μm. **g**, Representative immunofluorescence images of γ-H2AX staining in brain. Scale bar, 100 μm. **h**,**i**, The percentage of collagen fiber area in liver (**h**) and kidney (**i**) measured by the Masson's trichrome staining ($n = 8$). **j**, Quantitative analysis of expression level of TUNEL in kidney ($n = 8$). **k**–**n**, Quantitative analysis of epidermal thickness (**k**) and number of epidermal cells per millimeter thickness (**l**) measured by H&E staining, as well as dermal thickness (**m**) and collagen content (**n**) measured by the Masson's trichrome staining ($n = 8$). **o**, Quantitative analysis of expression level of γ-H2AX in skin ($n = 8$). **p**, Quantitative analysis of expression level of γ-H2AX in brain ($n = 8$). **q**, Clustering trend plots showed the numbers of DEGs across different organs. **r**, Cluster analysis showed the main upregulated DEGs in liver, kidney, skin, intestine, brain and pan-tissues treated with EVs^{ABPCs}. **s**–**u**, Representative tracking images of Y maze (**s**), NOR (**t**), and EPM (**u**) in EVs$^{A\text{-}BMSCs}$ and EVs$^{F\text{-}BMSCs}$ groups. **v**, *Ex vivo* fluorescence images of brains at 48 h after injection of DiR-labeled EVs by tail vein and their quantitative analysis ($n = 8$). Scale bar, 500 μm. Statistical significance was calculated by one-way ANOVA with Bonferroni's multiple comparisons test (**h**–**p** and **v**). Data were presented as mean ± s.d. $^{***}P < 0.001$, and $^{****}P < 0.0001$.

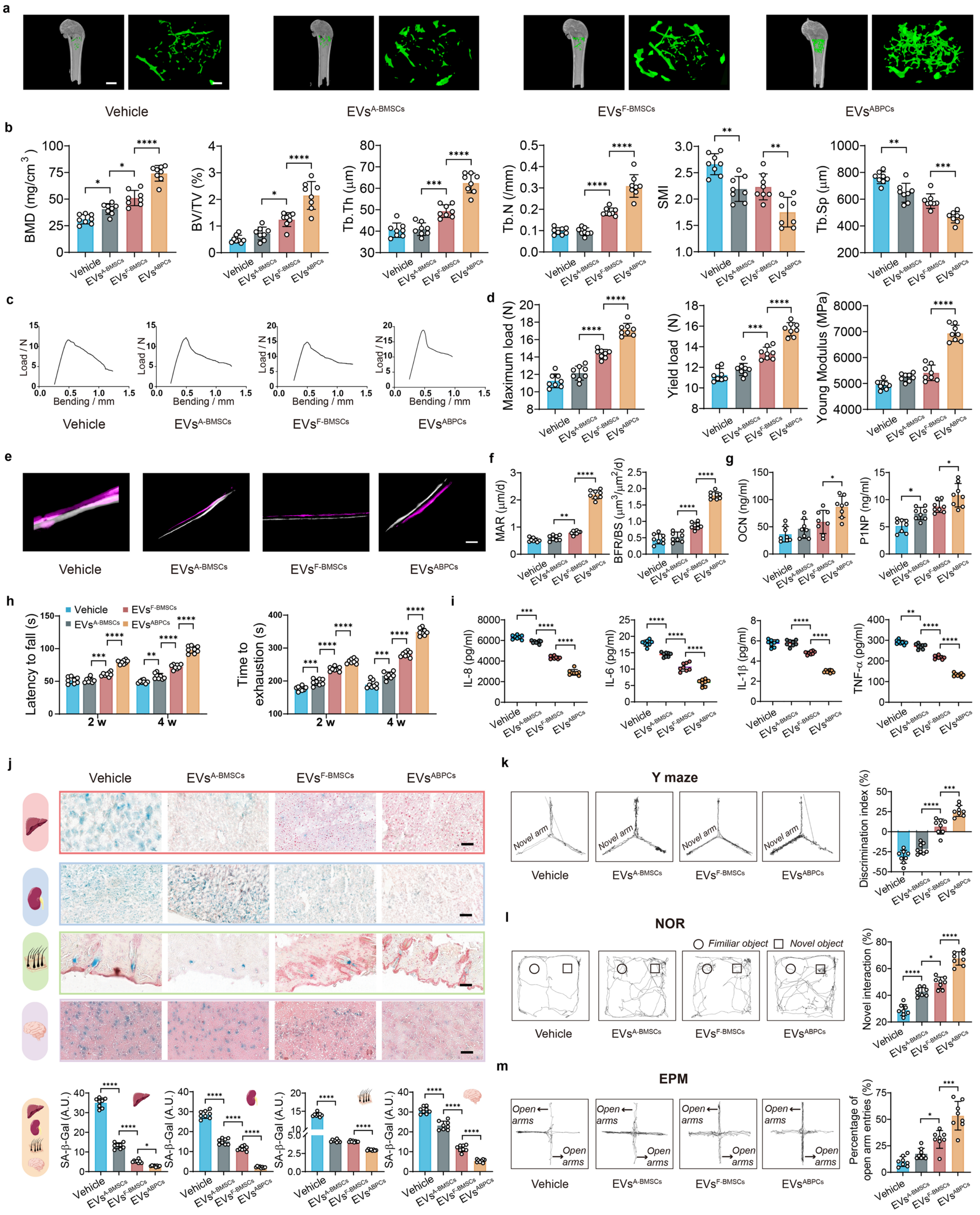

Extended Data Fig. 7 | See next page for caption.

Extended Data Fig. 7 | EVs$^{\mathrm{ABPCs}}$ rescue multiple age-associated phenotypes in aged female mice. a, Representative Micro-CT reconstruction images of femurs with different EVs treatment from female mice. Scale bar, 1,500 μm (left) or 300 μm (right). **b**, Quantitative analysis of trabecular bone from different groups, including BMD, BV/TV, Tb.Th, Tb.N, SMI, and Tb.Sp ($n = 8$). **c**,**d**, Representative images of the mechanical strength of femurs in female mice (**c**). Quantitative analysis of the maximum load, yield load, and Young's modulus ($n = 8$) (**d**). **e**,**f**, Representative images (**e**) and quantitative analysis (**f**) of MAR and BFR/BS in female mice from different groups ($n = 8$). Scale bar, 50 μm. **g**, The serum concentration of OCN and P1NP in female mice from different groups ($n = 8$). **h**, Quantification of the changes in motor coordination (left) and fatigue resistance (right) tests in female mice ($n = 8$). **i**, The serum concentration of inflammatory factors (IL-8, IL-6, IL-1β and TNF) levels with EVs treatment ($n = 8$). **j**, Representative SA-β-gal staining and quantification for SA-β-Gal activity in liver, kidney, skin, and brain (from top to bottom) of aged female mice with EVs treatment ($n = 8$). Scale bar, 50 μm (liver, skin, and brain) or 200 μm (kidney). **k**, Spatial working memory was assessed using the Y maze as the discrimination index for the novel arm ($n = 8$). **l**, Object recognition memory was assessed by NOR as the percentage of time exploring the novel object ($n = 8$). **m**, Anxiety-like behavior was assessed by EPM as the percentage of open arm ($n = 8$). Statistical significance was calculated by one-way ANOVA with Bonferroni's multiple comparisons test (**b**, **d**, and **f**–**m**). Data are presented as mean ± s.d. $^{*}P < 0.05$, $^{**}P < 0.01$, $^{***}P < 0.001$, and $^{****}P < 0.0001$.

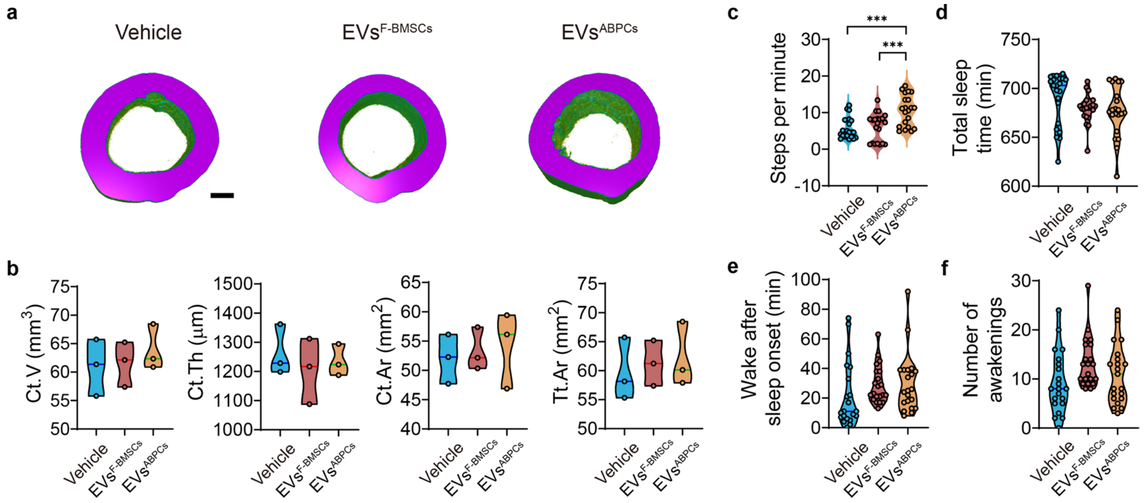

Extended Data Fig. 8 | EVs$^{\mathrm{ABPCs}}$ ameliorate bone loss and improved locomotor functions in aged rhesus macaques. a, Representative three-dimensional CT reconstructed images of cortical bone, with regions of interest colored in purple. Scale bar, 2,500 μm. **b**, Quantitative analysis of cortical bone in aged rhesus macaques following EVs treatments, including Ct.V, Ct.Th, Ct.Ar, and Tt.Ar ($n = 3$). **c**–**f**, Quantification of exercise model, including steps per minute (**c**), as well as sleep model, including total sleep time (**d**), wake after sleep onset (**e**), and number of awakenings (**f**) in aged rhesus macaques treated with EVs during the noninvasive monitor neck collar test. Data was collected daily over a consecutive 7-day recording period ($n = 3$). Statistical significance was calculated by one-way ANOVA with Bonferroni's multiple comparisons test (**b**, **c**, and **f**), or nonparametric Kruskal–Wallis test with Dunn's multiple comparisons test (**d** and **e**). Data were presented as mean ± s.d. ***$P < 0.001$.

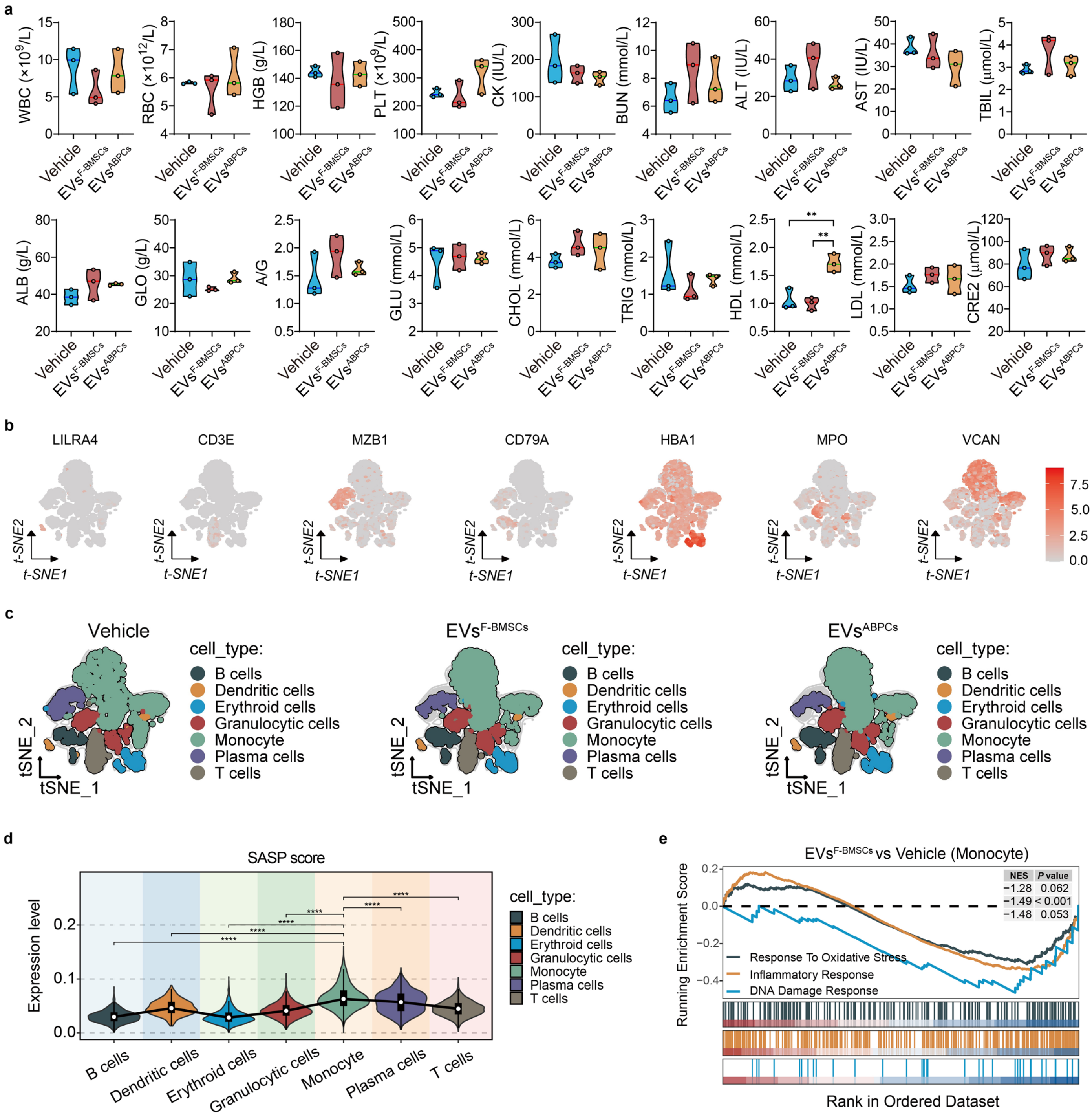

Extended Data Fig. 9 | Indicators of blood examination and bone marrow scRNA-seq in aged rhesus macaques. a, The counts of white blood cells (WBC), red blood cells (RBC), hemoglobin (HGB), and platelets (PLT) in the blood, along with serum levels of creatine kinase (CK), blood urea nitrogen (BUN), alanine aminotransferase (ALT), aspartate aminotransferase (AST), total bilirubin (TBIL), albumin (ALB), globulin (GLO), albumin-to-globulin ratio (A/G), glucose (GLU), total cholesterol (CHOL), triglycerides (TRIG), high-density lipoprotein cholesterol (HDL), low-density lipoprotein cholesterol (LDL), and creatinine (CRE2) were measured ($n = 3$). **b**, *t*-SNE plots were generated to depict the expression of specific genes representing seven cell populations: dendritic cells (*LILRA4*), T-cells (*CD3E*), plasma cells (*MZB1*), B-cells (*CD79A*), erythroid cells (*HBA1*), granulocytes (*MPO*), and monocytes (*VCAN*). **c**, A combined two-dimensional visualization of single-cell clusters in aged rhesus macaques with different treatments. **d**, A violin plot was utilized to display the scores of SASP gene expression across seven immune cell lineages ($n = 3$). Violin plots depict the data distribution (kernel density), density (violin width), IQR (embedded box), mean (white dot), and mean ± s.d. (whiskers). Lines connecting the medians across groups illustrate the overall trend of the data distribution. **e**, GSEA showed the regulated pathways in the monocyte subpopulation when comparing the EVs$^{\text{F-BMSCs}}$ group to the vehicle group. Statistical significance was calculated by one-way ANOVA with Bonferroni's multiple comparisons test (**a** and **d**). Data were presented as mean ± s.d. $^{**}P < 0.01$, and $^{****}P < 0.0001$.

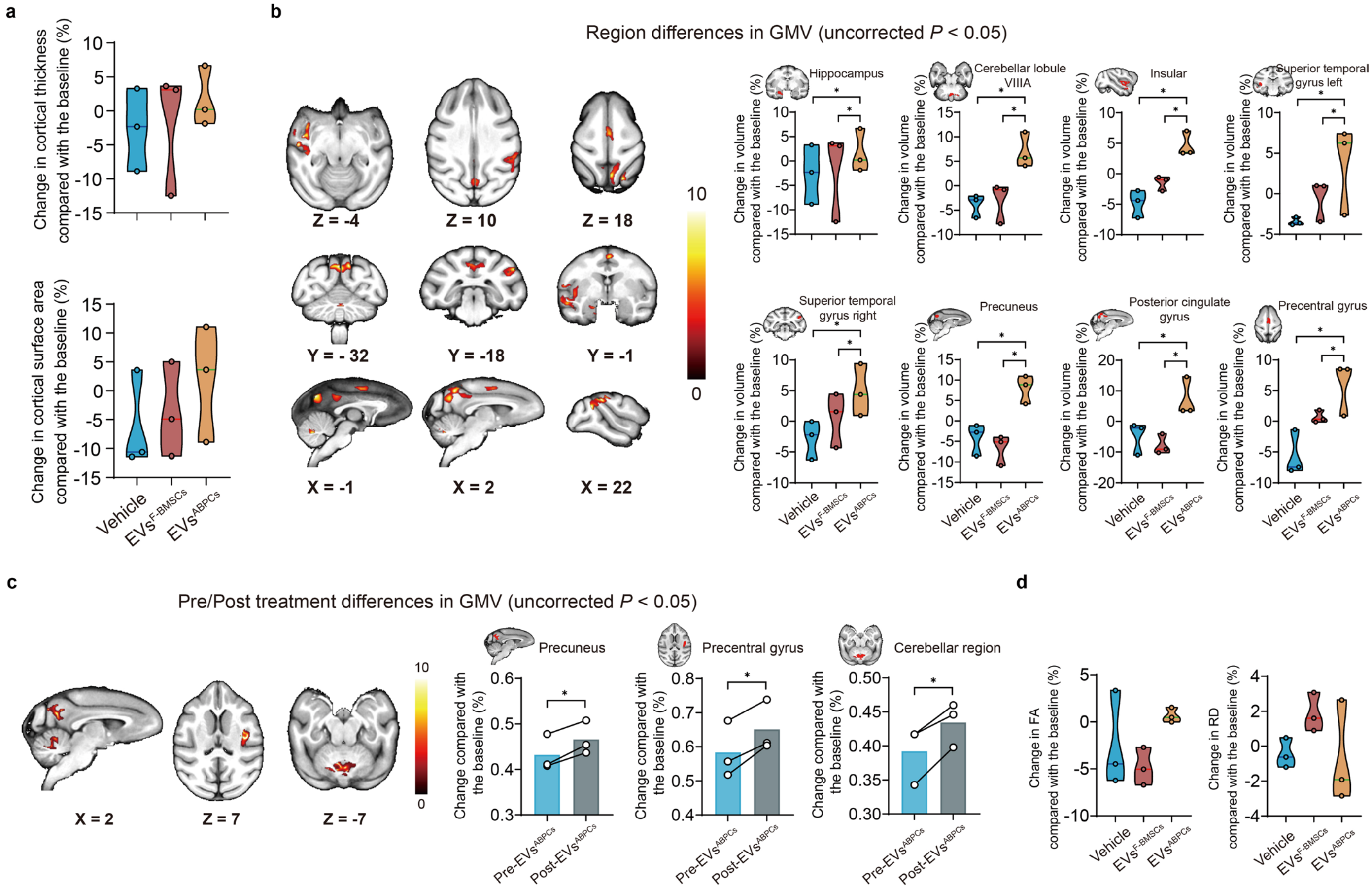

Extended Data Fig. 10 | Changes related to brain aging in EVs^{ABPCs}-treated aged rhesus macaques. a, A quantitative analysis was performed to evaluate changes in cortical thickness and surface area following EVs treatment ($n = 3$). **b**, VBM analysis showed region variations in GMV among groups, with red areas indicating significant differences in GMV. Quantitative analysis of the significantly different brain regions in GMV following different treatments ($n = 3$). **c**, The comparison of GMV between pre-treatment and post-treatment at an uncorrected *P*-value threshold was performed specifically for the EVs^{ABPCs} group. Quantification of GMV changes between pre-treatment and post-treatment in the EVs^{ABPCs} group was conducted without correction for multiple comparisons ($n = 3$). The lines connect the same individuals, showing the trend between pre- and post-treatment. **d**, A quantitative analysis of the changes of FA and RD following EVs treatment ($n = 3$). Statistical analyses were performed using the Kruskal–Wallis nonparametric test followed by post hoc pairwise comparisons followed by one-tailed Mann–Whitney U-tests with FWE correction (**a** and **d**), or not (**b**); one-tailed Wilcoxon matched-pairs signed rank test for within-group comparisons (**c**). Data were presented as mean ± s.d. Uncorrected $^{*}P < 0.05$.

nature portfolio

Corresponding author(s): Yonggang Yao; Wen Wang; Zhuojing Luo; Qiang Qiu; Jinghui Huang

Last updated by author(s): May 19, 2025

Reporting Summary

Nature Portfolio wishes to improve the reproducibility of the work that we publish. This form provides structure for consistency and transparency in reporting. For further information on Nature Portfolio policies, see our Editorial Policies and the Editorial Policy Checklist.

Statistics

For all statistical analyses, confirm that the following items are present in the figure legend, table legend, main text, or Methods section.

n/a	Confirmed	
☐	☒	The exact sample size (*n*) for each experimental group/condition, given as a discrete number and unit of measurement
☐	☒	A statement on whether measurements were taken from distinct samples or whether the same sample was measured repeatedly
☐	☒	The statistical test(s) used AND whether they are one- or two-sided *Only common tests should be described solely by name; describe more complex techniques in the Methods section.*
☒	☐	A description of all covariates tested
☐	☒	A description of any assumptions or corrections, such as tests of normality and adjustment for multiple comparisons
☐	☒	A full description of the statistical parameters including central tendency (e.g. means) or other basic estimates (e.g. regression coefficient) AND variation (e.g. standard deviation) or associated estimates of uncertainty (e.g. confidence intervals)
☐	☒	For null hypothesis testing, the test statistic (e.g. F, t, r) with confidence intervals, effect sizes, degrees of freedom and P value noted *Give P values as exact values whenever suitable.*
☒	☐	For Bayesian analysis, information on the choice of priors and Markov chain Monte Carlo settings
☒	☐	For hierarchical and complex designs, identification of the appropriate level for tests and full reporting of outcomes
☐	☒	Estimates of effect sizes (e.g. Cohen's *d*, Pearson's *r*), indicating how they were calculated

Our web collection on statistics for biologists contains articles on many of the points above.

Software and code

Policy information about availability of computer code

Data collection	The details were listed in the supplementary table 7. Specifically including: BD FACSCalibur™ (BD Biosciences); Zen blue (Zeiss, version 3.5); HT7800 series transmission electron microscopes (Hitachi); ZetaView analysis software (Particle Metrix, version 8.03.08.02); GE Amersham Imager 600 (GE HealthCare); illumina NovaSeq 6000 sequencing platform (Illumina); SkyScan 1276 (Bruker); BehaviorAtlas Capture (Monkey) (BayONE Scientific, version 1.01); ActiLife (ActiGraph LLC, version 6.13.4); GE Lightspeed VCT Scaner (GE HealthCare); Symbia Intevo 6 SPECT/CT (Siemens Healthineers); xSPECT Quant (Siemens Healthineers); 3T uMR NX system (United Imaging Healthcare, Shanghai, China).
Data analysis	The details were listed in the supplementary table 7. Specifically including: GraphPad Prism (version 9.0); ImageJ (Fiji) (version 2.14.0/1.54i); Image-Pro Plus (version 6); SPSS Statistics (version 27); PASS (version 23.0.2); NRecon (version 1.7.3.1); Dataviewer (version 0.4.8); CTAn (version 1.18); Ctvox (version 3.3.0 r1401); ModFit LT (version 3.0); 3D Slicer (version 5.6.2); BehaviorAtlas Analyzer (Monkey) (version 1.01); BehaviorAtlas Explorer (Monkey) (version 1.01); MATLAB (version 9.15.0.2047132); R software (version 4.2.0); Cell Ranger (version 7.0.1); Fastp (version 0.23.1); Limma (version 3.52.1); Seurat (version 4.3.0); scDblFinder (version 1.17.1); Harmony (version 0.1.1); clusterProfiler (version 4.9.3); AUCell (version 1.18.1); Metascape (version 3.5); Cytoscape (version 3.8.2); ggplot2 (version: 3.4.2); GseaVis (version 0.0.9); scatterplot3d (version 0.3.42); MaxQuant (version 1.6.14); SPM12 (version r7771); MRIcroGL (version 1.2.20211006); FSL (version 6.0.6.4); MRtrix3 (version 3.0.4); FreeSurfer (version 7.4.1); bedtools (version 2.31.0); samtools (version 1.19); DMwR2 (version 0.0.2); glmnet (version 4.1-8). The code used in this study is available at GitHub (https://github.com/finalbeibeiyu/Nature_aging).

For manuscripts utilizing custom algorithms or software that are central to the research but not yet described in published literature, software must be made available to editors and reviewers. We strongly encourage code deposition in a community repository (e.g. GitHub). See the Nature Portfolio guidelines for submitting code & software for further information.

Data

Policy information about availability of data

All manuscripts must include a data availability statement. This statement should provide the following information, where applicable:

- Accession codes, unique identifiers, or web links for publicly available datasets
- A description of any restrictions on data availability
- For clinical datasets or third party data, please ensure that the statement adheres to our policy

All omics data generated in this study have been deposited in the GEO database (transcriptome), and iProX database (proteome), which have been publicly released. The transcriptomic data of EVs, cells and mice (including serum and tissues) are accessible via GSE289038. The transcriptomic data of rhesus macaques are accessible via GSE273278. For scRNA-seq of rhesus macaques, the data are accessible via GSE288582. For proteomics of EVs, the data are accessible via PXD064039. Additionally, all data associated with this study are present in the paper or the Supplementary files.

Research involving human participants, their data, or biological material

Policy information about studies with human participants or human data. See also policy information about sex, gender (identity/presentation), and sexual orientation and race, ethnicity and racism.

Reporting on sex and gender	N/A
Reporting on race, ethnicity, or other socially relevant groupings	N/A
Population characteristics	N/A
Recruitment	N/A
Ethics oversight	N/A

Note that full information on the approval of the study protocol must also be provided in the manuscript.

Field-specific reporting

Please select the one below that is the best fit for your research. If you are not sure, read the appropriate sections before making your selection.

☒ Life sciences ☐ Behavioural & social sciences ☐ Ecological, evolutionary & environmental sciences

For a reference copy of the document with all sections, see nature.com/documents/nr-reporting-summary-flat.pdf

Life sciences study design

All studies must disclose on these points even when the disclosure is negative.

Sample size	For mouse: The required sample size to achieve statistically significant differences was calculated using standard power analysis (α = 0.05, power = 0.90) with the aid of PASS software (Version 23.0.2). The final sample size was determined to be 8 mice per group, accounting for assay variability and potential dropouts. For the rhesus macaques' experiments, we chose a sample size of 3 individuals per group. This sample size was determined based on a review of the existing literature, where similar studies have successfully employed small groups of macaques to evaluate treatment outcomes (Circulation 2020 142(6):556-574; Nature 2023 624(7992):611-620).
Data exclusions	No animals or data points were excluded and omitted from the analysis.
Replication	Main experimental findings (micrographs, blots, hematology, and etc.) were validated through three independently performed experiments. All replication presented the similar results.
Randomization	Cells and animals were allocated to each treatment group by using simple randomization. Different treatment groups were processed identically, and animals in different treatment groups were exposed to the same environment.
Blinding	All experiments were conducted with randomization and blinding performed by an independent researcher prior to EVs injection. During allocation, animals were randomly assigned to each group (mice in EVsABPCs, EVsF-BMSCs, EVsA-BMSCs and PBS-treated groups; rhesus macaques in EVsABPCs, EVsF-BMSCs and saline-treated groups), with group allocation being concealed from the therapists, collectors, and analysts. Throughout the experiment, the therapists remained blinded to the group allocations and handled all animals uniformly. They were also unaware of the specific treatments and provided consistent care across different groups. Following treatment, data were collected by individuals who blinded to both the treatment and group allocation. Similarly, data were analyzed by analysts who remained blinded to the treatment details. Groups were unblinded after the completion of the statistical analysis.

Reporting for specific materials, systems and methods

We require information from authors about some types of materials, experimental systems and methods used in many studies. Here, indicate whether each material, system or method listed is relevant to your study. If you are not sure if a list item applies to your research, read the appropriate section before selecting a response.

Materials & experimental systems

n/a	Involved in the study	
☐	☒	Antibodies
☒	☐	Eukaryotic cell lines
☒	☐	Palaeontology and archaeology
☐	☒	Animals and other organisms
☒	☐	Clinical data
☒	☐	Dual use research of concern
☒	☐	Plants

Methods

n/a	Involved in the study	
☒	☐	ChIP-seq
☐	☒	Flow cytometry
☐	☒	MRI-based neuroimaging

Antibodies

Antibodies used

Recombinant Anti-gamma H2A.X (phospho S139) antibody [EP854(2)Y] (ab81299) Abcam Cat# ab81299, RRID:AB_1640564, 1:250
Recombinant Anti-p21 antibody [EPR18021] (ab188224) Abcam Cat# ab188224, RRID:AB_2734729, 1:500
Recombinant Anti-CD9 antibody [EPR27551-92] (ab307085) Abcam Cat# ab307085, 1:1000
Recombinant Anti-CD81 antibody [EPR4244] (ab109201) Abcam Cat# ab109201, RRID:AB_10866464, 1:1000
Recombinant Anti-TSG101 antibody [EPR7130(B)] (ab125011) Abcam Cat# ab125011, RRID:AB_10974262, 1:1000
Recombinant Anti-Lamin B1 antibody [EPR22165-121] (ab229025) Abcam Cat# ab229025, RRID:AB_3083735, 1:1000
Anti-ALP antibody (ab224335) Abcam Cat# ab224335, 1:200
Anti-Osteocalcin antibody (ab93876) Abcam Cat# ab93876, RRID:AB_10675660, 1:200
Anti-TRAP/CD40L antibody (ab65854) Abcam Cat# ab65854, RRID:AB_2075950, 1:200
HRP conjugated Goat Anti-Rabbit IgG (H+L) Servicebio Cat# GB23303, RRID:AB_2811189, 1:10000
Cy3-Conjugated Goat Anti-Rabbit IgG (H+L) Servicebio Cat# GB21303, RRID:AB_2861435, 1:200

Validation

All the antibodies used in this study have been tested by the manufacturer and have been cited by other authors and the referencesare available on the manufacturer's websites.
Anti-gamma H2A.X antibody in immunofluorescence was confirmed by the manufacturer using knockout validation. The antibody has been cited in over 270 publications. See https://www.abcam.com/en-us/products/primary-antibodies/gamma-h2ax-phospho-s139-antibody-ep8542y-ab81299
Anti-p21 antibody in immunofluorescence was confirmed by the manufacturer using knockout validation. The antibody has been cited in over 210 publications. See https://www.abcam.com/en-us/products/primary-antibodies/p21-antibody-epr18021-ab188224
Anti-CD9 antibody in western blotting was confirmed by the manufacturer using knockout validation. The antibody has been cited in 4 publications. See https://www.abcam.com/en-us/products/primary-antibodies/cd9-antibody-epr27551-92-ab307085
Anti-CD81 antibody in western blotting was produced by the manufacturer using recombinant. The antibody has been cited in over 250 publications. See https://www.abcam.com/en-us/products/primary-antibodies/cd81-antibody-epr4244-ab109201
Anti-TSG101 antibody in western blotting was produced by the manufacturer using recombinant. The antibody has been cited in over 250 publications. See https://www.abcam.com/en-us/products/primary-antibodies/tsg101-antibody-epr7130b-ab125011
Anti-Lamin B1 antibody in immunofluorescence was confirmed by the manufacturer using Abcam's "Advanced Validation". The antibody has been cited in 12 publications. See https://www.abcam.com/en-us/products/primary-antibodies/lamin-b1-antibody-epr22165-121-ab229025
Anti-ALP antibody in immunohistochemistry was produced by the manufacturer. The antibody has been cited in 19 publications. See https://www.abcam.com/en-us/products/primary-antibodies/alp-antibody-ab224335
Anti-Osteocalcin antibody in immunohistochemistry was produced by the manufacturer. The antibody has been cited over 330 publications. See https://www.abcam.com/en-us/products/primary-antibodies/osteocalcin-antibody-ab93876
Anti-TRAP/CD40L antibody in immunohistochemistry was produced by the manufacturer. The antibody has been cited in 15 publications. See https://www.abcam.com/en-us/products/primary-antibodies/trap-cd40l-antibody-ab65854

Animals and other research organisms

Policy information about studies involving animals; ARRIVE guidelines recommended for reporting animal research, and Sex and Gender in Research

Laboratory animals

Eighteen-month-old C57 male and female mice with no diseases were provided unrestricted access to food and water within a regulated environment featuring a 12-hour light/dark cycle, maintained at a consistent temperature (23 ± 2 ℃) and humidity (50% ± 20%).
Nine healthy female rhesus macaque monkeys ranging in age from 16 to 18 years old were selected for this study. All monkeys were housed at the Kunming Institute of Zoology at the Chinese Academy of Sciences and were provided unrestricted access to standard monkey chow and fruit and water in sunny room maintained at a 12-h light/dark cycle.
Three healthy two-year-old male sika deer were used for this study. The deer were housed in enclosures under farming conditions, with ad libitum access to water and feed (consisting primarily of dry oak leaves, fresh grass, and supplemented cooked soybean

	cakes).
Wild animals	The study did not involved the wild animals.
Reporting on sex	We utilized both male and female mice, while only female rhesus macaques in the study. Additionally, we used male deer. Meanwhile, the use of males or females is clearly reported in the Methods.
Field-collected samples	No filed-collected samples were used in this study.
Ethics oversight	All animal procedures complied with Association for Assessment and Accreditation of Laboratory Animal Care International guidelines. Rodent studies were approved by the Animal Ethics Committee of Fourth Military Medical University (IACUC-20230075). Rhesus macaque experiments were conducted under approval from the Institutional Animal Care and Use Committee of Kunming Institute of Zoology, Chinese Academy of Sciences (IACUC-PE-2023-05-002). Sika deer procedures were approved by the Animal Ethics Committee of Changchun Sci-Tech University (CKARI202007).

Note that full information on the approval of the study protocol must also be provided in the manuscript.

Plants

Seed stocks	N/A
Novel plant genotypes	N/A
Authentication	N/A

Flow Cytometry

Plots

Confirm that:

☒ The axis labels state the marker and fluorochrome used (e.g. CD4-FITC).

☒ The axis scales are clearly visible. Include numbers along axes only for bottom left plot of group (a 'group' is an analysis of identical markers).

☐ All plots are contour plots with outliers or pseudocolor plots.

☒ A numerical value for number of cells or percentage (with statistics) is provided.

Methodology

Sample preparation	Cells (1 × 106) were washed and centrifuged at 112 × g for 5 min. The resulting pellets were resuspended in 1 mL of PBS and centrifuged again at 112 × g for 5 min to eliminate impurities. Following this, the cell pellet was incubated darkly with 500 µL PI/RNase Staining Buffer (BD Biosciences, 550825) for 30 min at 25 °C.
Instrument	BD FACSCalibur™ (BD Biosciences)
Software	ModFit LT (version 3.0)
Cell population abundance	No sorting procedure was included in cell cycle analysis. (Caffa, I. et al., Nature, 2020, PMID: 32669709; Bi Y. et al., Cell Metabolism, 2025, PMID: 39818209)
Gating strategy	No gating strategy was included in cell cycle analysis. (Caffa, I. et al., Nature, 2020, PMID: 32669709; Bi Y. et al., Cell Metabolism, 2025, PMID: 39818209)

☐ Tick this box to confirm that a figure exemplifying the gating strategy is provided in the Supplementary Information.

Magnetic resonance imaging

Experimental design

Design type	Structural MRI
Design specifications	No specific experimental setup was used

Behavioral performance measures	No behavioral measures was used

Acquisition

Imaging type(s)	Structural, mainly T1 weighted imaging
Field strength	3T
Sequence & imaging parameters	T1: TR/TE=11.3/4.8 ms; inversion time=880 ms; flip angle=8°; voxel size=0.5×0.5×0.5 mm3
Area of acquisition	Whole brain

Diffusion MRI ☒ Used ☐ Not used

Parameters	DTI: (TR/TE = 5300/62 ms; voxel size = 1×1×1 mm3; 116 directions: b = 500 s/mm2 (11 directions), b = 1000 s/mm2 (23 directions), b = 1500 s/mm2 (34 directions), b = 2000 s/mm2 (45 directions); three b = 0 s/mm2 images; number of slices = 90; GRAPPA factor = 2; multiband factor = 2

Preprocessing

Preprocessing software	Preprocessing for voxel-based morphology (VBM) was carried out in SPM12 (www.fil.ion.ucl.ac.uk/spm) running on Matlab R2020b (Mathworks Inv., Sherborn, MA, USA).
Normalization	The t1-weighted images were 1) reoriented to AC-PC line manually in SPM12; 2) segmented to gray matter (GM), white matter (WM) and cerebrospinal fluid (CSF) in native space by tissue probability maps (TPMs) of INIA19 template; 3) based on the diffeomorphic anatomical registration through exponentiated lie algebra (DARTEL) algorithm, the segmented images were used to create the sample GM and WM templates; 4) according to created templates as mediator, the individual GM and WM images were spatially normalized to the INIA19 macaque brain template space (0.5mm isotropic); 5) the voxel values were modulated by Jacobian determinants of the deformation field and finally the GM and WM density images in INIA19 space were calculated. In this study, total intracranial volume (TIV) is calculated as sum of GM and WM density multiplied by voxel size, which is 0.5×0.5×0.5 mm^3 (divided by 1000 to convert units to cm^3.).
Normalization template	We used the INIA19 template and atlas of macaque, which contains tissue probability maps of GM, WM and CSF (Rohlfing et al. 2012).
Noise and artifact removal	During acquisition, real-time motion monitoring was employed to detect head movement. If triggering, the scan pauses immediately followed by animal condition assessment to determine continuation. Images were manually reviewed for artifacts, with re-scan decisions based on animal's status. 1. For the structural MRI data: (1) Visual inspection revealed no notable artifacts; (2) Structural images were acquired on two occasions, and during preprocessing, these acquisitions were initially registered and subsequently averaged to improve the signal-to-noise ratio and mitigate noise. 2. Diffusional data were evaluated for b0 temporal SNR, non-b0 image contrast-to-noise ratio, and motion metrics. Susceptibility distortion, motion artifacts and eddy current correction in the diffusion image were conducted by FMRIB Software Library (version 6.0.6.4).
Volume censoring	During preprocessing, we checked the effects of segmentation and normalization visually. Finally , there was no case need to be excluded.

Statistical modeling & inference

Model type and settings	Mainly mass univariate analysis
Effect(s) tested	We used Kruskal-wallis test for non-parametric comparison among groups to estimate structural brain changes.

Specify type of analysis: ☐ Whole brain ☐ ROI-based ☒ Both

Anatomical location(s)	Total intracranial volume (TIV), gray matter volume (GMV), white matter volume (WMV) were calculated and compared at the whole brain level. The percentage volume change for gray matter and white volume were calculated and compared in a voxel-wise manner using mass univariate analysis (uncorrected).
Statistic type for inference (See Eklund et al. 2016)	For any pair-wise comparison, we used permutation tests and reported FWE corrected p values.
Correction	Permutation tests were performed and the resultant p values were corrected for FWE for multiple comparison correction. (description in materials and methods)

Models & analysis

n/a	Involved in the study
☒	☐ Functional and/or effective connectivity
☒	☐ Graph analysis
☒	☐ Multivariate modeling or predictive analysis